

Synthesis and intercalation of epitaxial graphene on iridium

Petrović, Marin

Doctoral thesis / Disertacija

2014

Degree Grantor / Ustanova koja je dodijelila akademski / stručni stupanj: **University of Zagreb, Faculty of Science / Sveučilište u Zagrebu, Prirodoslovno-matematički fakultet**

Permanent link / Trajna poveznica: <https://urn.nsk.hr/urn:nbn:hr:217:680505>

Rights / Prava: [In copyright](#) / [Zaštićeno autorskim pravom.](#)

Download date / Datum preuzimanja: **2024-04-24**



Repository / Repozitorij:

[Repository of the Faculty of Science - University of Zagreb](#)





UNIVERSITY OF ZAGREB
FACULTY OF SCIENCE
DEPARTMENT OF PHYSICS

Marin Petrović

**SYNTHESIS AND INTERCALATION
OF EPITAXIAL GRAPHENE
ON IRIDIUM**

DOCTORAL THESIS

Zagreb, 2014.



UNIVERSITY OF ZAGREB
FACULTY OF SCIENCE
DEPARTMENT OF PHYSICS

Marin Petrović

**SYNTHESIS AND INTERCALATION
OF EPITAXIAL GRAPHENE
ON IRIDIUM**

DOCTORAL THESIS

Supervisor: dr. sc. Marko Kralj

Zagreb, 2014.



SVEUČILIŠTE U ZAGREBU
PRIRODOSLOVNO-MATEMATIČKI FAKULTET
FIZIČKI ODSJEK

Marin Petrović

**SINTEZA I INTERKALACIJA
EPITAKSIJALNOG GRAFENA
NA IRIDIJU**

DOKTORSKI RAD

Mentor: dr. sc. Marko Kralj

Zagreb, 2014.

This thesis was made under the mentorship of dr. sc. Marko Kralj as a part of the doctoral study at the Department of Physics, Faculty of Science, University of Zagreb. Presented experimental work was carried out at the Institute of Physics in Zagreb and several collaborating universities (University of Cologne, Columbia University) and research facilities (Brookhaven National Laboratory, Elettra synchrotron).

Ovaj rad je izrađen pod mentorstvom dr. sc. Marka Kralja u sklopu doktorskog studija na Fizičkom odsjeku Prirodoslovno-matematičkog fakulteta Sveučilišta u Zagrebu. Prezentirani eksperimentalni rad je proveden na Institutu za fiziku u Zagrebu i nekoliko surađujućih sveučilišta (Sveučilište u Kölnu, Sveučilište Columbia) i istraživačkih ustanova (Nacionalni laboratorij Brookhaven, sinkrotron Elettra).

Acknowledgments

I would like to thank my mentor dr. sc. Marko Kralj for guidance and unlimited support over the years. His systematic approach and dedication to science were essential for my research. I also express my gratitude to dr. sc. Petar Pervan for providing me with the opportunity to conduct my PhD studies at the Institute of Physics. Many thanks to dr. sc. Ivo Pletikosić for his numerous advices and assistance in the lab. Furthermore, I am thankful to all other people from the Institute of Physics who in one way or another contributed to my scientific work.

I wish to thank prof. dr. sc. Thomas Michely, dr. sc. Carsten Busse and all other collaborators from the University of Cologne for sharing their knowledge with me, especially on the STM technique, and for being such good hosts during my visits to Cologne. I also thank dr. sc. Tonica Valla and dr. sc. Jerzy T. Sadowski from Brookhaven National Laboratory for their support during ARPES and LEEM measurements. I acknowledge all members of the group of prof. dr. sc. Richard M. Osgood from the Columbia University for our successful cooperation on 2PPE studies. I am thankful to prof. dr. sc. Thomas Fauster for the lending of the Ir(100) crystal.

Finally, I would like to thank my parents, Marija and Vlado, my sister Anita and my wife Petra for encouragement and support throughout the years.

BASIC DOCUMENTATION CARD

University of Zagreb
Faculty of Science
Department of Physics

Doctoral thesis

SYNTHESIS AND INTERCALATION OF EPITAXIAL GRAPHENE ON IRIDIUM

MARIN PETROVIĆ

Epitaxial graphene on iridium (111) surface is considered to be one of the best systems for studying intrinsic properties of graphene due to the weak interaction with the substrate which is predominantly of the van der Waals character. In epitaxial systems, graphene's properties can be modified or some new ones can be induced by the processes of intercalation of various atoms or molecules in between the graphene and the substrate. Therefore, a detailed understanding of the formation of such hybrid systems, from graphene synthesis to its intercalation, is crucial for their complete understanding.

In this thesis, results relevant for the growth and intercalation of epitaxial graphene synthesized on Ir(111) are presented. By utilizing well-established procedures for graphene synthesis, samples with various graphene coverages are prepared in order to characterize the growth of graphene in detail. Different species (specifically, Cs, Li, Eu and O) are also deposited on such samples which results in the formation of new, hybrid (and most often intercalated) systems whose properties depend on the exact preparation parameters. In order to characterize the morphology, low energy electron microscopy (LEEM) and scanning tunneling microscopy (STM) are used while the electronic structure is investigated by means of angle-resolved photoemission spectroscopy (ARPES) and two-photon photoemission spectroscopy (2PPE). The growth of graphene is characterized on a microscopic level, focusing on small graphene islands and their interaction with iridium. For a complete graphene monolayer, a network of graphene wrinkles is studied. It is found that such network exhibits ordering on the micrometer scales dictated by the substrate. Occupied and unoccupied electronic structure in the vicinity of the Brillouin zone center is investigated via spectroscopic techniques establishing basic relations between the states located below and above the Fermi level. From the aspect of intercalation, Cs deposition on well defined graphene layer is studied and emerging spectroscopic and morphological features are characterized. By this, a novel mechanism of intercalation and the corresponding dynamics behind it are revealed. A competition between Coulomb and van der Waals interactions turns out to be crucial in such epitaxial systems. In addition, intercalation of Li, Eu and O are characterized with special emphasis on the electronic structure at the K point of the Brillouin zone which gives new insight on the influence of various intercalated layers on the surface states of iridium.

(143 pages, 62 figures, 5 tables, 187 references)

Keywords: epitaxial graphene, iridium, intercalation, temperature programmed growth (TPG), wrinkles, graphene islands, surface states, image-potential states

Language of the original: English

Supervisor: dr. sc. Marko Kralj, higher research associate,
Institute of Physics, Zagreb

Reviewers: 1. prof. dr. sc. Amir Hamzić,
Faculty of Science, University of Zagreb
2. dr. sc. Marko Kralj, higher research associate,
Institute of Physics, Zagreb
3. prof. dr. sc. Thomas Michely,
Institute of Physics II, University of Cologne
4. assoc. prof. dr. sc. Goranka Bilalbegović,
Faculty of Science, University of Zagreb
5. prof. dr. sc. Hrvoje Buljan,
Faculty of Science, University of Zagreb

Thesis accepted: September 9, 2014

TEMELJNA DOKUMENTACIJSKA KARTICA

Sveučilište u Zagrebu
Prirodoslovno-matematički fakultet
Fizički odsjek

Doktorski rad

SINTEZA I INTERKALACIJA EPITAKSIJALNOG GRAFENA NA IRIDIJU

MARIN PETROVIĆ

Epitaksijalni grafen na iridiju (111) se smatra jednim od najboljih sistema za proučavanje intrinzičnih svojstava grafena zbog slabog međudjelovanja s podlogom koje je dominantno van der Waals tipa. U epitaksijalnim sistemima, svojstva grafena se mogu mijenjati ili se čak mogu inducirati neka nova u procesima interkalacije različitih atoma ili molekula između grafena i podloge. Stoga je detaljno razumijevanje nastanka takvih hibridnih sistema, od sinteze grafena do njegove interkalacije, ključno za njihovo potpuno razumijevanje.

U ovom radu su prezentirani rezultati relevantni za rast i interkalaciju epitaksijalnog grafena sintetiziranog na Ir(111). Korištenjem dobro utvrđenih postupaka za sintezu, pripremljeni su uzorci s različitim pokrivenostima iridijeve površine grafenom kako bi se detaljno okarakterizirao njegov rast. Na takve uzorke nanoseni su drugi kemijski elementi (specifično, Cs, Li Eu i O) što je rezultiralo stvaranjem novih, hibridnih (i najčešće interkaliranih) sistema čija svojstva ovise o konkretnim parametrima pripreme. Za karakterizaciju morfologije se koriste nisko-energetska elektronska mikroskopija (LEEM) i pretražna tunelirajuća mikroskopija (STM) dok se elektronska struktura istražuje kutno-razlučivom fotoemisijskom spektroskopijom (ARPES) i dvo-fotonsko fotoemisijskom spektroskopijom (2PPE). Rast grafena je karakteriziran na mikroskopskom nivou sa posebnim fokusom na malene grafenske otoke i njihovo međudjelovanje s iridijem. Za cjeloviti grafenski sloj, istražena su svojstva mreže grafenskih nabora te je nađeno da takva mreža pokazuje uređenost na mikrometarskim skalama koja je određena s podlogom. Pomoću spektroskopskih tehnika je istražena popunjena i nepopunjena elektronska struktura u blizini centra Brillouinove zone čime su uspostavljene osnovne veze između stanja koja se nalaze ispod i iznad Fermijevog nivoa. S aspekta interkalacije, obavljena je spektroskopska i morfološka karakterizacija depozicije cezija na dobro definiran grafenski sloj. Pri tome je otkriven novi mehanizam interkalacije kao i odgovarajuća dinamika koja je vezana uz taj proces. Pokazuje se da je natjecanje između van der Waals i Coulomb međudjelovanja od ključne važnosti u epitaksijalnim sistemima. Dodatno, okarakterizirana je interkalacija litija, europija i kisika sa posebnim naglaskom na elektronsku strukturu u blizini K točke Brillouinove zone čime je dobiven novi uvid u utjecaj različitih interkaliranih slojeva na površinska stanja iridija.

(143 stranice, 62 slike, 5 tablica, 187 literaturnih navoda)

Ključne riječi: epitaksijalni grafen, iridij, interkalacija, temperaturno programirani rast (TPG), grafenski nabori, grafenski otoci, površinska stanja, stanja zrcalnog potencijala

Jezik izvornika: Engleski

Mentor: dr. sc. Marko Kralj, v. zn. suradnik,
Institut za fiziku, Zagreb

Povjerenstvo: 1. prof. dr. sc. Amir Hamzić,
Prirodoslovno-matematički fakultet, Sveučilište u Zagrebu
2. dr. sc. Marko Kralj, v. zn. suradnik,
Institut za fiziku, Zagreb
3. prof. dr. sc. Thomas Michely,
Institut za fiziku II, Sveučilište u Kölnu
4. izv. prof. dr. sc. Goranka Bilalbegović,
Prirodoslovno-matematički fakultet, Sveučilište u Zagrebu
5. prof. dr. sc. Hrvoje Buljan,
Prirodoslovno-matematički fakultet, Sveučilište u Zagrebu

Rad prihvaćen: 9. rujna 2014.

Contents

Prolouge	xiii
1 Introduction	1
1.1 Ideal freestanding graphene	2
1.1.1 Crystal structure	2
1.1.2 Valence and conduction band dispersion	3
1.1.3 Image-potential states	5
1.2 Exceptional physical properties	7
1.3 Graphene on Ir(111)	9
1.3.1 Structural features	9
1.3.2 Binding strength and interaction with iridium	11
1.4 Stress relaxation in epitaxial graphene	13
1.5 Graphene islands	15
1.6 Intercalation related effects	16
1.7 Objectives	18
2 Sample preparation and experimental methods	19
2.1 Sample preparation and graphene growth procedures	20
2.2 Angle-resolved photoemission spectroscopy	21
2.3 Two-photon photoemission spectroscopy	24
2.4 Scanning tunneling microscopy and spectroscopy	25
2.5 Low energy electron microscopy	27
2.6 Low energy electron diffraction	29
3 Microscopic characterization of graphene growth	31
3.1 Morphological analysis	32
3.1.1 STM results	32
3.1.2 LEEM results	33
3.1.3 Synthesis on Ir(100)	35
3.2 Evolution of the electronic structure	37
3.3 Carbon loss in TPG growth	41
3.4 Average work function	42
3.5 Graphene wrinkles	45
3.5.1 Wrinkles network	45
3.5.2 Localized stress relaxation and wrinkle pinning	48
3.5.3 Voronoi approximation	51
3.5.4 Internal structure	53

4	Electronic structure at the Brillouin zone center	55
4.1	Rashba-split surface states of iridium	55
4.2	Image-potential states of graphene on Ir(111)	58
5	The mechanism and effects of caesium intercalation	63
5.1	Morphology and phase separation	64
5.1.1	LEED results	64
5.1.2	STM results	65
5.1.3	LEEM results	67
5.2	Electronic structure	69
5.3	Theoretical calculations	71
5.4	Driving forces for intercalation	72
5.5	Intercalation dynamics	73
5.5.1	Graphene on Ir(111)	73
5.5.2	Graphene on Ir(100)	75
5.6	De-intercalation	76
5.7	Adatom interaction in the α -phase	78
5.8	Quasiparticle scattering	80
5.9	Properties of ionic adsorption	84
5.9.1	Relating work function and Dirac point position	85
5.9.2	Three-step adsorption model	87
6	Intercalation with other species	91
6.1	Lithium intercalation	91
6.2	Europium intercalation	94
6.3	Oxygen intercalation	96
6.3.1	Electronic structure	97
6.3.2	Confined Dirac electrons and graphene decoupling	99
7	Conclusion	101
	Appendix A	105
	Appendix B	109
	Appendix C	111
	Sažetak na hrvatskom jeziku	113
	Bibliography	140

Most of the results presented in this thesis have been published in peer-reviewed papers. Those papers are listed here in accordance with their relevance to specific chapters.

Chapter 3

- * Kralj, M., Pletikosić, I., Petrović, M., Pervan, P., Milun, M., N'Diaye, A. T., Busse, C., Michely, T., Fuji, J. and Vobornik, I. Graphene on Ir(111) characterized by angle-resolved photoemission. *Physical Review B* **84**, 075427 (2011).
- * Niesner, D., Fauster, Th., Dadap, J. I., Zaki, N., Knox, K. R., Yeh, P.-C., Bhandari, R., Osgood, R. M., Petrović, M. and Kralj, M. Trapping surface electrons on graphene layers and islands. *Physical Review B* **84**, 081402(R) (2012).

Chapter 4

- * Niesner, D., Fauster, Th., Dadap, J. I., Zaki, N., Knox, K. R., Yeh, P.-C., Bhandari, R., Osgood, R. M., Petrović, M. and Kralj, M. Trapping surface electrons on graphene layers and islands. *Physical Review B* **84**, 081402(R) (2012).

Chapter 5

- * Petrović, M., Šrut Rakić, I., Runte, S., Busse, C., Sadowski, J. T., Lazić, P., Pletikosić, I., Pan, Z.-H., Milun, M., Pervan, P., Atodiresei, N., Brako, R., Šokčević, R., Valla, T., Michely, T. and Kralj, M. The mechanism of caesium intercalation of graphene. *Nature communications* **4**, 2772 (2013).
- * Schumacher, S., Wehling, T. O., Lazić, P., Runte, S., Förster, D. F., Busse, C., Petrović, M., Kralj, M., Blügel, S., Atodiresei, N., Caciuc, V. and Michely, T. The backside of graphene: Manipulating adsorption by intercalation. *Nano letters* **13**, 5013–9 (2013).

Chapter 6

- * Jolie, W., Craes, F., Petrović, M., Atodiresei, N., Caciuc, V., Blügel, S., Kralj, M., Michely, T. and Busse, C. Confinement of Dirac electrons in graphene quantum dots. *Physical Review B* **89**, 155435 (2014).

List of commonly used acronyms

1NN - first nearest neighbor

2PPE - two-photon photoemission

ARPES - angle-resolved photoemission spectroscopy

BZ - Brillouin zone

CVD - chemical vapor deposition

E_F - Fermi level

E_V - vacuum level

FT - Fourier transform

FT-STM - Fourier transform scanning tunneling microscopy

FWHM - full width at half maximum

Gr - graphene

IPS - image-potential state

LEED - low energy electron diffraction

LEEM - low energy electron diffraction

(L)DOS - (local) density of states

ML - monolayer

STM - scanning tunneling microscopy

STS - scanning tunneling spectroscopy

TB - tight-binding

TPG - temperature programmed growth

UHV - ultra-high vacuum

Prologue

Simple structure and chemical composition of graphene could naively fool us to believe that its properties are equally simple and straightforward to understand. But anyone studying this remarkable material will surely agree that its characteristics are far from trivial and that the science which is found in graphene is fascinating. Indeed, the significance of graphene research was acknowledged in 2010 when Andre Geim and Konstantin Novoselov were awarded the Nobel Prize in physics “*for groundbreaking experiments regarding the two-dimensional material graphene*”. Furthermore, graphene used in those groundbreaking experiments was obtained from a piece of graphite and a scotch-tape (by a procedure also called mechanical exfoliation) [1], which cannot really be considered as the most sophisticated method of modern sample fabrication. Soon after the publication of these first results in 2004, graphene research went through the roof and a new, two-dimensional (2D) route of research in physics (and other fields as well) has been opened. To be fair, scientists, especially surface physicists and chemists, conducted research on thin graphitic films back in the 60’s (see e.g. Refs. [2–4]). However, the full potential of those films was not recognized and they were often considered to be an undesired byproduct of sample preparation, partially due to the lack of sophisticated surface science experimental methods available today.

Ideally, graphene is a 2D material which is often thought of as an infinite, flat sheet of hexagonally-arranged carbon atoms (see Fig. 1). In reality, things are more complicated because graphene is most often synthesized on a substrate and is then referred to as epitaxial graphene. This means that there is an interaction acting between the graphene and its substrate which modifies graphene’s intrinsic properties. The extent of these modifications will depend on the strength of the interaction i.e. binding to the substrate. One of the most commonly used substrates are SiC [5–7] and various metals [8–15]. Due to the extent of literature which can be found on graphene on these substrates, we will

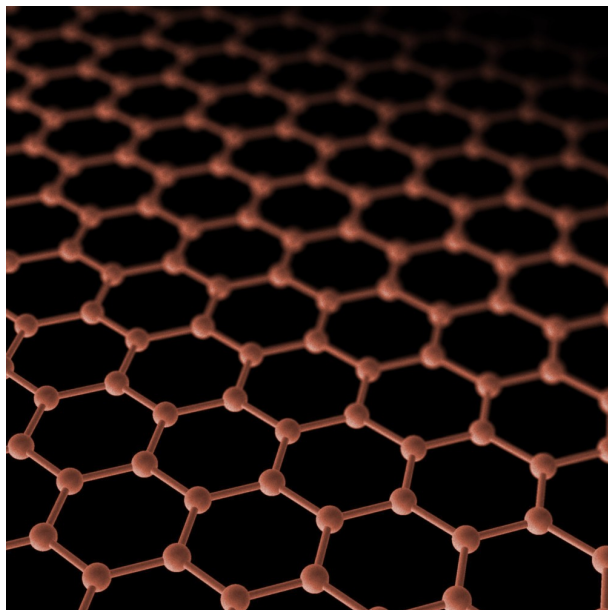


Figure 1: A model of an ideal graphene layer.

refrain from a detailed description of those systems in the main text and the reader is pointed to given references (and references therein). Graphene on metals can be roughly divided into two classes: (i) strongly bound, chemisorbed graphene where the binding significantly changes graphene properties and (ii) weakly bound, physisorbed graphene which is more similar to free-standing graphene. If one wants to explore fundamental graphene properties, an optimal substrate has to be chosen in order to obtain high-quality graphene crystals and at the same time preserve its intrinsic properties. As will be demonstrated, the (111) face of iridium is an ideal candidate for this task.

The growth of graphene on a substrate often implies initial nucleation of many small islands which form bigger crystals as the synthesis procedure progresses. Hence, the properties of small graphene islands, which may differ from those of an extended layer, are also important to understand, all the more since various quantum effects become more pronounced as the dimensions of studied system get smaller. Therefore, epitaxial graphene has to be studied at various stages of growth and cannot be always simplified by an infinite sheet of carbon hexagons.

Once the properties of graphene on a particular substrate are well documented, the next fundamental question arises: What would be a good way to modify, or possibly even precisely control those properties? One of the most commonly used procedures is certainly graphene intercalation. By insertion of various atoms and molecules between the graphene and the substrate, many novel properties can be induced. Even graphite in-

tercalation has been investigated in detail and recognized as interesting [16], yielding e.g. superconductivity in several graphite intercalated compounds. Besides many new properties which can be realized by intercalation of epitaxial graphene, thorough understanding of driving forces enabling it is also required. Such knowledge is crucial for gaining control over the intercalation process and tailoring of intercalated systems properties.

Graphene can also be studied in a much wider context as a basic building block of some other carbon-based materials such as buckyballs, nanotubes and graphite [17, 18]. Thus, studying graphene also contributes to understanding of these materials. Moreover, since the pioneering work on graphene by Geim and Novoselov, many other layered materials became interesting to scientists. Among them are e.g. hexagonal boron nitride (hBN), transition metal dichalcogenides, silicene and others [19, 20] because of their 2D nature. Also, topological insulators [21] and 3D topological Dirac semimetals [22, 23] have been discovered which exhibit an electronic dispersion inherent to graphene. It is therefore safe to say that the discovery of graphene, due to its groundbreaking novel properties, initiated a brand new field of research studying a wide range of novel materials [24].

The structure of this thesis is the following: in Chapter 1 we give an introduction to epitaxial graphene with special focus to the fundamental properties of graphene on Ir(111). Then, sample preparation and experimental methods used for sample characterization are described in Chapter 2. Turning to the results, graphene synthesis is presented in Chapter 3 which is followed by a description of the electronic structure at the Brillouin zone center in Chapter 4. Cs intercalation results represent a large part of this thesis and they are given in Chapter 5. In the final chapter, Chapter 6, we present additional results of graphene intercalation by several other chemical species: Li, Eu and O. Conclusion, Appendices and Bibliography are given at the end of the thesis.

CHAPTER 1

Introduction

Graphene on Ir(111) [Gr/Ir(111)] is one of the most extensively studied epitaxial graphene systems. A substantial number of papers can be found on various aspects of a Gr/Ir(111) system including synthesis recipes, structural characterization, intercalation compound properties etc. In the following, we introduce the reader with all important and the most recent information on the Gr/Ir(111) system which will be relevant for results interpretation and discussions that follow in the subsequent chapters of this thesis.

First, crystal and electronic structure of ideal, freestanding graphene is presented. A relatively simple tight-binding approximation can be used to describe the valence and conduction band of graphene. After that, some of the most interesting properties of graphene arising from its specific structure are briefly introduced. Furtheron, we turn to the morphology and electronic structure of graphene on Ir(111). In particular, graphene's high structural quality and the preservation of characteristic linear band dispersion are depicted. Turning to more mesoscopic structural features, we also introduce graphene wrinkles which are common to almost all epitaxial graphene systems. In addition, graphene islands preceding the formation of an extended graphene crystal are described. Finally, properties of graphene can be modified chemically by the insertion of various atoms or molecules in between the graphene and its substrate. This process, known as intercalation, yields many novel graphene hybrid systems and we will reflect on them at the end of this chapter.

1.1 Ideal freestanding graphene

1.1.1 Crystal structure

Graphene consists of carbon atoms arranged in a 2D hexagonal lattice. There are two atoms in the basis of a unit cell resulting in a honeycomb structure consisting of perfect hexagons. Equivalently, graphene can be regarded as a crystal consisting of two hexagonal lattices shifted with respect to each other. A model of graphene structure is shown in Fig. 1.1(a) where the two-atom basis is marked by red and blue circles. It turns out that this kind of structure is the key for many of graphene's fascinating properties.

The origin of graphene honeycomb structure is found in three sp^2 hybrid orbitals which form by linearly combining $2s$, $2p_x$ and $2p_y$ carbon orbitals. These hybrid orbitals all lie in the same plane mutually forming an angle of 120° which is a characteristic angle of the honeycomb structure [cf. Fig. 1.1(a)]. sp^2 orbitals of the neighboring atoms form σ -bonds which in turn constitute σ bands in the extended 2D crystal. σ -bonds are responsible for the exceptional mechanical integrity and elasticity of graphene and they define the C-C atomic distance which is equal to 1.42 \AA . The remaining $2p_z$ carbon orbitals do not participate in the hybridization and are left standing perpendicular to the sp^2 -hybrid plane. Overlap of the $2p_z$ orbitals forms π -bonds and consequentially π bands which are half-filled and they define most of graphene's electronic and optical properties.

The reciprocal lattice of graphene is shown in Fig. 1.1(b). The 2D structure in real space maps into a corresponding 2D structure in the reciprocal space. The first Brillouin zone (BZ) of graphene is shaded in gray in Fig. 1.1(b) where we also marked high symmetry points of the BZ: Γ , M, K and K'. There are two nonequivalent neighboring points in the corners of the BZ, K and K', since one cannot use unit vectors \mathbf{b}_1 and \mathbf{b}_2 to translate from the K point to the K' point. As there are two atoms in the basis of a graphene unit cell, the electron wave functions can be described by two components. Mathematically, these two components can be thought of as two possible spin orientations, allowing us to introduce the pseudospin degree of freedom [25–27]. Having pseudospin, it is also possible to define helicity as the projection of the momentum along the pseudospin direction. Electrons at K and K' points have opposite helicities which, once more, indicates

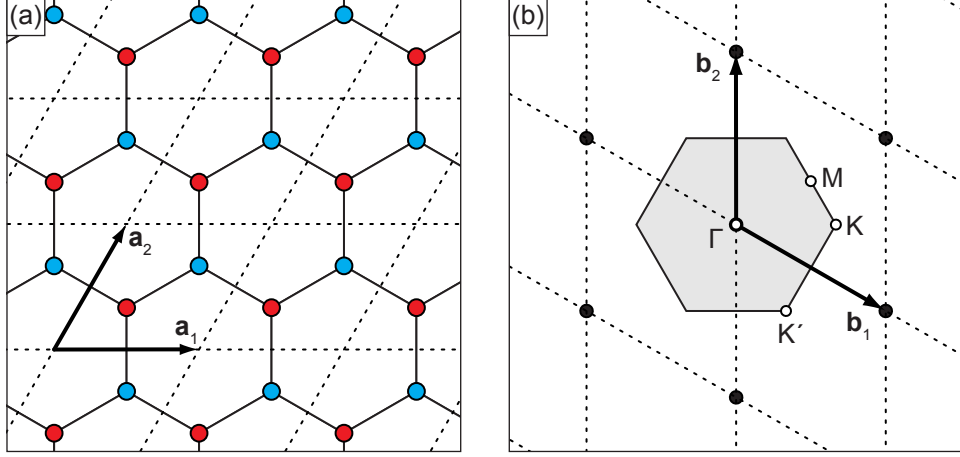


Figure 1.1: (a) A model of graphene lattice. Blue and red circles are carbon atoms corresponding to the two atoms in the basis of each unit cell (marked by dashed lines). \mathbf{a}_1 and \mathbf{a}_2 are primitive vectors of the lattice. (b) A reciprocal lattice of graphene. The gray-shaded hexagon corresponds to the first Brillouin zone of graphene. High symmetry points Γ , M , K and K' are marked by white dots. \mathbf{b}_1 and \mathbf{b}_2 are primitive vectors of the reciprocal lattice.

the nonequivalence of K and K' points.

1.1.2 Valence and conduction band dispersion

Graphene π bands are formed by tunneling of the electrons between the neighboring $2p_z$ orbitals which can be accurately described within the tight-binding (TB) approximation. In this way, the dispersion relation of the valence band and the conduction band (usually labeled as π and π^* bands, respectively) can be obtained with simple calculations. The lack of TB approximation is the neglect of many-body effects (e.g. electron-phonon coupling, plasmarons etc.) which are required if a more detailed description of the band structure is necessary. In Appendix A we derive π and π^* band dispersion relations and here we just write down the final result. The dispersion relation of π and π^* bands in the first nearest-neighbor (1NN) TB approximation has the form

$$E(\mathbf{k}) = \frac{\epsilon \pm \gamma_0 w(\mathbf{k})}{1 \pm s_0 w(\mathbf{k})} \quad (1.1)$$

where $w(\mathbf{k}) = \sqrt{1 + 4 \cos\left(\frac{a\sqrt{3}}{2}k_y\right) \cos\left(\frac{a}{2}k_x\right) + 4 \cos^2\left(\frac{a}{2}k_x\right)}$. k_x and k_y are the components of the electron wavevector \mathbf{k} and a is graphene lattice constant. ϵ is the orbital energy of the $2p_z$ level while γ_0 and s_0 are electron hopping (tunneling) energy and overlap between neighboring $2p_z$ -orbitals. s_0 is often negligibly small and set to zero. In Fig.

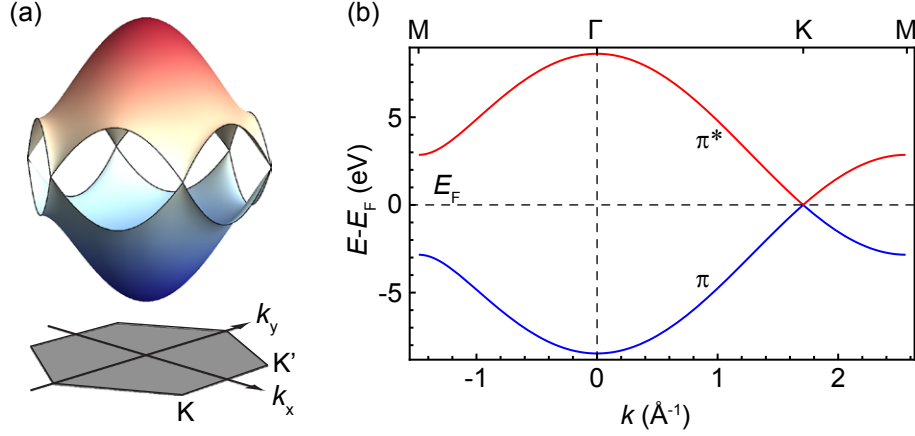


Figure 1.2: Graphene π band structure calculated in the 1NN TB approximation ($a = 2.45 \text{ \AA}$, $\varepsilon = 0 \text{ eV}$, $\gamma_0 = 2.848 \text{ eV}$, $s_0 = 0.0029$). **(a)** A 3D plot of the π (blue shade) and π^* (red shade) bands in the first BZ (gray hexagon). The bands meet at K and K' points where also the Dirac cones are found. **(b)** A plot of the π and π^* bands in the high symmetry Γ KM and Γ M directions. The linearity of the dispersion is apparent in the vicinity of the K point.

1.2(a) we show the plot of the Eq. 1.1 in the first BZ. It is visible that π and π^* bands touch each other only at six K and K' points of the BZ making graphene a semi-metal or equivalently a zero gap semiconductor. Moreover, the dispersion in the vicinity of these points is linear, as can be more clearly seen in the Fig. 1.2(b). Because of this linear energy-momentum dependence (as in the case of photons), electrons near the K and K' points can be described by the Dirac equation for massless particles and the corresponding electronic states constitute so-called Dirac cones in the k -space. Accordingly, points where the π and π^* bands meet are referred to as Dirac points. For the ideal freestanding graphene the Fermi level (E_F) is situated at the energy of the Dirac points.

Eq. 1.1 can be used to calculate the density of states (DOS) of graphene which exhibit several interesting features. One of them is a linear dependence of DOS with energy in the vicinity of the Dirac point (see Appendix A). Furthermore, van Hove singularities are found in DOS which are related to the existence of local extrema in the dispersion at the M points of the BZ [cf. Fig. 1.2(b)]. These two features become relevant for doped graphene, when the chemical potential is significantly changed and the Fermi surface is correspondingly modified. When the charge is transfer to (from) graphene, E_F shifts above (below) the six Dirac points. Therefore, the Fermi surface transforms from six discrete points to six circular, and later on triangularly warped pockets. This is illustrated in Fig. 1.3(a) and (b) where equienergetic contours of graphene TB dispersion are shown. The

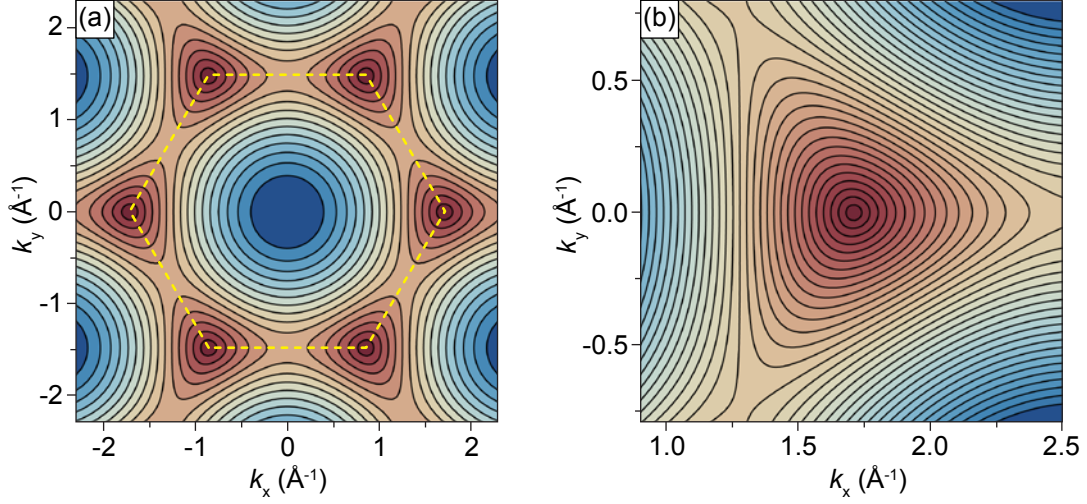


Figure 1.3: Equienergetic contours of graphene TB dispersion **(a)** in the first BZ marked by a yellow dotted line and **(b)** in the vicinity of the K point. Consecutive contour separation is 0.53 eV in (a) and 0.18 eV in (b). The contours centered at the K point evolve from circular to triangular shapes as the energetic separation from the Dirac point increases. An area enclosed by those contours is directly proportional to the charge transferred to graphene (see Eq. 1.2).

black closed curves (filled by red shades) can be identified with the Fermi surface of doped graphene (neglecting the renormalization due to the many-body effects). The integration of DOS from the Dirac point up to E_F yields a simple formula which can be used for the calculation of charge transfer n to (or from) initially neutral graphene (see Appendix A for details):

$$n = \frac{A_{FC}}{\pi^2} \quad (1.2)$$

where A_{FC} is the area of the Fermi contour at a given doping level [e.g. an area enclosed by one of the black contours centered at the K point in Fig. 1.3(b)] which can be measured experimentally.

1.1.3 Image-potential states

Graphene is an ultimate one-atom thick material. Having no bulk, its two mirror-symmetric surfaces and the related surface-phenomena define graphene's properties to a great extent. An important feature of metallic surfaces is the effective potential at the metal-vacuum interface. One significant component of that potential arises from the spillout of the electrons from the metal into the vacuum which defines the work function

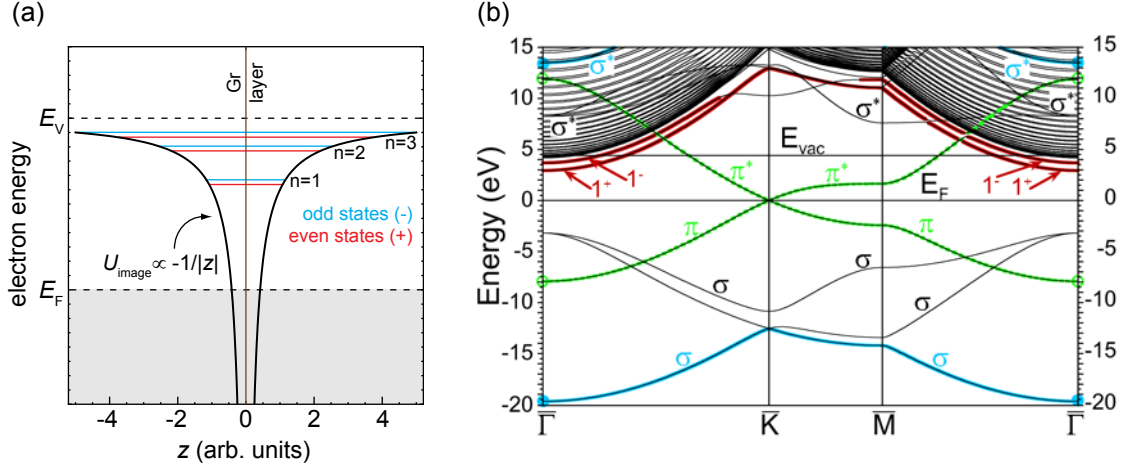


Figure 1.4: (a) An illustration of the image potential U_{image} and the first three image-potential states ($n = 1, 2, 3$) of graphene. Each state is split into an even (+) and odd (-) state due to the finite small thickness of the graphene layer. (b) Theoretical calculation of the band structure of freestanding graphene. π (green) and σ (blue) bands are highlighted as well as the first ($n = 1$) IPS (red). Splitting to an even (1^+) and odd (1^-) state is evident. Panel (b) is adopted from Ref. [31].

of the metal. Another component is image potential which originates from the attraction between the electron trying to leave the surface and its positive image charge. Image potential has a Coulomb-like form, $U_{\text{image}} \propto -1/z$, where z is the distance between the electron and the image plane. If a surface projected bulk band gap exists on the metal side, a series of electronic states, called image-potential states (IPSs) can be formed between the band gap and the image potential [28–30]. These states are located between the Fermi and the vacuum level and are unoccupied when the system is in equilibrium; If one wants to populate them, electron excitation from the occupied part of the band structure is necessary. The dispersion of the IPSs is discrete in the direction perpendicular to the surface and resembles to a Rydberg series of energy levels while it has free-electron form in the direction parallel to the surface.

Graphene has two equivalent semi-metal surfaces so IPSs can form on both of them [see Fig. 1.4(a)]. Moreover, since those two surfaces are just one atomic layer apart, electrons occupying IPSs on opposite surfaces belong to the same system. This results in the formation of a double series of IPSs of even (+) and odd (-) symmetry with respect to the reflection in the graphene plane [31]. Energies of those states are not degenerate so that each energy level n ($n = 1, 2, 3, \dots$) consists of two sublevels as schematically illustrated in Fig. 1.4(a). In Fig. 1.4(b) we show LDA calculations of the band structure of freestanding graphene which includes the first even (1^+) and odd (1^-) IPS [31]. It

is visible that the IPSs are located at the Γ point, are pinned to the vacuum level and exhibit parabolic dispersion in the direction parallel to graphene surface.

IPSs are important from the aspect of overall electronic structure, dielectric properties, hot-electron dynamics and current conduction [32] and photoluminescence effects [33]. In addition, IPS wavefunctions extend relatively far from the graphene plane, making them sensitive to the nature of graphene-substrate binding. Moreover, large spatial extension causes hybridization of the IPSs from the neighboring graphene sheets in graphite which gives rise to the interlayer states [31]. The interlayer states, in turn, can hybridize with the s states of metals in graphite intercalated compounds which is believed to play a crucial role in their superconductive properties [34].

1.2 Exceptional physical properties

Because of its specific crystal and electronic structure described in the previous section, graphene exhibits many superior physical properties. Here, we shall address the most interesting among them in a brief and concise manner.

✱ **Ambipolar electric field effect.** If one manufactures a device composed of graphene placed on a dielectric, e.g. SiO, which enables fabrication of a field-effect transistor and the application of back gate voltage V_g , it is possible to measure graphene's transport properties such as e.g. resistivity ρ [1]. Graphene is gapless semiconductor and its valence and conduction bands are symmetric with respect to the Fermi level. This kind of electronic structure then gives rise to the ambipolar electric field effect which is reflected in the symmetric shape of the $\rho - V_g$ curve with respect to zero gate voltage and doping. In other words, charge carriers can be continuously tuned between electrons and holes and current conduction is independent of the type of carriers. Also, charge carrier concentrations as high as 10^{13} cm^{-2} can be achieved by gating [1, 17].

✱ **Mobility and ballistic transport.** Measured graphene devices possess very high charge mobilities μ , ranging from $\sim 10\,000 \text{ cm}^2 \text{ V}^{-1} \text{ s}^{-1}$ for first measured samples [1] to $\sim 200\,000 \text{ cm}^2 \text{ V}^{-1} \text{ s}^{-1}$ for the samples cooled to 5 K [35]. For comparison, typical room temperature mobility values for Si and Ge are lower, $\sim 1\,500 \text{ cm}^2 \text{ V}^{-1} \text{ s}^{-1}$ and

$\sim 4\,500\text{ cm}^2\text{ V}^{-1}\text{ s}^{-1}$, respectively. In any case, μ remains very high even at high carrier concentrations and results in ballistic transport on almost micrometer scale.

✱ **Landau levels.** Placing a 2D system in a perpendicular magnetic field results in discretization of its energy spectrum to energy levels, called Landau levels, which exhibit linear separation in energy, $E_N \propto (N + 1/2)$ (N being the index of a level). For graphene containing Dirac fermions, the situation is somewhat unusual. The level separation is not linear any more and one level exists at zero energy: $E_N \propto \sqrt{N}$ [17, 26]. The zero-energy level ($N = 0$) is shared by electron and holes, which is not the case for other levels. This kind of Landau discretization is a consequence of massless character of electrons in graphene [26].

✱ **Anomalous quantum Hall effect.** Measurement of Hall conductivity σ_{xy} as a function of electron and hole concentration n in a constant magnetic field provides an interesting result: conductivity exhibits plateaux at $\sigma_{xy} = (4e^2/h)(N + 1/2)$ (N being the index of a plateau) which are shifted by $2e^2/h$ from the usually expected sequence [36]. This observation can be related to the existence of zero-energy Landau level and the fact that it is occupied by both electrons and holes. Because of this shift, graphene exhibits half-integer (or anomalous) quantum Hall effect.

✱ **Linear optical adsorption.** Because of its specific electronic structure, graphene has almost constant adsorption of electromagnetic radiation in a broad wavelength interval ranging from 300 (visible) to 2 500 (near infrared) nm [33]. One graphene layer adsorbs $\approx 2.3\%$ (which is $\approx \pi\alpha$, α being fine structure constant) of incident radiation, meaning that it is in principle transparent, but also optically visible.

✱ **Mechanical strength.** Up to now we've reflected only on graphene properties emerging from the specific structure of the π bands. However, its mechanical properties are determined by the strength of the σ -bonds. A convenient way of testing the mechanical properties of graphene is by performing indentation experiments on suspended graphene with an AFM tip [37]. It turns out that graphene is one of the strongest material known to us: its tensile strength is 130 GPa (while structural steel A36 has the value of 0.4 GPa) and it exhibits Young modulus of 1.0 TPa. We emphasize that these values are determined for one-atom thin graphene, making them even more astonishing.

New physics yields new applications—which is also valid in the case of graphene. Scientists and engineers are trying to exploit these exceptional properties of graphene to create new devices which could be used to improve our lives in near future. This is clearly supported by the list of keywords describing some of the potential applications: batteries, supercapacitors, solar cells, fuel cells, chemical sensors, DNA sequencing, flexible electronics, spintronics, transistors, touch screens, photodetectors, coatings, loudspeakers, electromagnetic shielding, thermal interfaces, lubrication, water deionization. And the list goes on. By adding the prefix *micro* or *nano* in front of those keywords, which is certainly legitimate in many cases, the perspective becomes even better. All this indicates that graphene research, besides fundamental physical aspects, is also of great importance from the applications point of view.

A prerequisite for future applications is large-scale high-quality graphene production which can be easily transferred to various substrates after the synthesis. In addition, graphene growth without the necessity of ultra-high vacuum (UHV) conditions is preferable in order to minimize the production costs. Significant advances have been made in this direction for graphene growth on polycrystalline metal films and foils; Among them, the most promising is the synthesis of graphene on Cu [15, 38] and Ni [39]. These metals can be easily etched away which greatly facilitates graphene transfer to other substrates in combination with polymer stamping. Primary goals in graphene growth on foils are the reduction of nucleation sites and number of relative orientations as well as better control over a number of synthesized graphene layers. This can be achieved by precise control of the growth parameters such as temperature and exposure rate or pressure of carbonaceous precursor. Another important aspect relevant for graphene application is large-scale growth on non-metallic substrates such as SiC [5] or Ge [40] which was shown to be possible at (or close to) atmospheric pressures.

1.3 Graphene on Ir(111)

1.3.1 Structural features

Iridium is a noble transition metal that crystallizes in face-centered cubic (FCC) lattice. Hence, its (111) surface has a hexagonal lattice with cell parameter of 2.715 Å [41]. (111) surface of Ir can be used to synthesize high-quality graphene samples with almost perfect

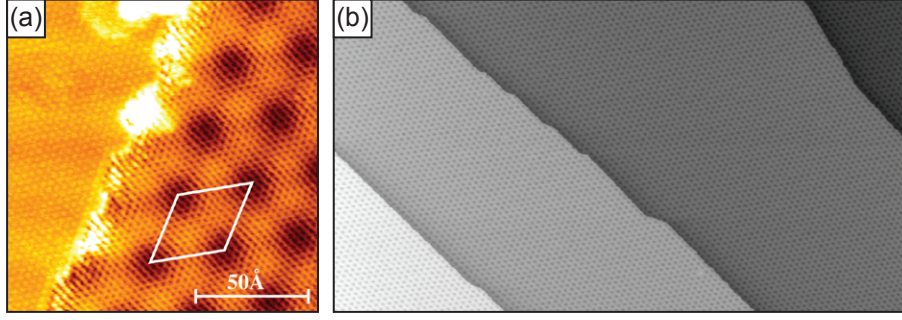


Figure 1.5: (a) An STM topograph of iridium (111) surface partially covered by graphene on the right side. Carbon rings as well as moiré structure (unit cell marked by white rhombus) can be resolved. Adopted from Ref. [41]. (b) $(125 \times 250) \text{ nm}^2$ STM topograph of graphene on Ir(111) extending over several iridium terraces i.e. crossing several iridium steps. Adopted from Ref. [10].

alignment of $\langle 10\bar{1} \rangle$ direction of iridium and $\langle 11\bar{2}0 \rangle$ direction of graphene (i.e. alignment of carbon zig-zag and Ir dense packed rows) by means of catalytic decomposition of gaseous carbohydrates in UHV [10, 41] (see Section 2.1 for details on the preparation procedure). STM topograph of a boundary between graphene and bare iridium is shown in atomic resolution in Fig. 1.5(a). Carbon rings (on the right side) as well as iridium atoms (on the left side) can be resolved. From such images one can easily determine the value of graphene lattice constant which is 2.45 Å [41]. What is also evident on graphene-covered side is an additional hexagonal periodicity, containing approximately ten carbon rings i.e. ten graphene unit cells. This is co-called moiré structure originating generally from a small mismatch between two well-defined overlapping periodicities. For Gr/Ir(111), the two periodicities differ by $1 - 2.45 \text{ Å} / 2.715 \text{ Å} \approx 10\%$. From STM, moiré periodicity is determined to be 25.3 Å [41] and thus forms an incommensurate (9.32×9.32) structure with respect to the iridium lattice. Moiré unit cell is marked in Fig. 1.5(a) by white rhombus. Moiré structure is also present on a full-layer graphene which is depicted in Fig. 1.5(b) where graphene extends over many iridium terraces and exhibits exceptional structural quality [10]. Such data also indicates that graphene can grow over step-edges of iridium without interruption in a carpet-like fashion and what is more, growth is possible in both step-up and step-down directions. This kind of growth mode is creditable for high quality of graphene on Ir(111) and is not universal to other epitaxial systems, e.g. graphene on Ru(0001) [42].

By controlling the growth temperature, it is also possible to prepare epitaxial Gr/Ir(111) in various orientations with respect to the substrate i.e. not to have perfect alignment

of $\langle 10\bar{1} \rangle$ and $\langle 11\bar{2}0 \rangle$ directions of iridium and graphene, respectively [43, 44]. In such cases, graphene orientation is labeled as $R\alpha$, where α is the angle between aforementioned directions of graphene and iridium. For STM image analysis, it is important to know the relation between α and the size of the moiré unit cell. In general, moiré lattice wavevector can be written as a difference between the graphene and iridium lattice wavevectors: $\mathbf{k}_{\text{moiré}} = \mathbf{k}_{\text{Gr}} - \mathbf{k}_{\text{Ir}}$. For an arbitrary angle α between \mathbf{k}_{Gr} and \mathbf{k}_{Ir} and by using the law of cosines, moiré wavevector module can be written as

$$k_{\text{moiré}}^2 = k_{\text{Gr}}^2 + k_{\text{Ir}}^2 - 2k_{\text{Gr}}k_{\text{Ir}} \cos \alpha \quad (1.3)$$

which then translates into the expression for the real-space lattice constants

$$a_{\text{moiré}} = \frac{a_{\text{Gr}}a_{\text{Ir}}}{\sqrt{a_{\text{Gr}}^2 + a_{\text{Ir}}^2 - 2a_{\text{Gr}}a_{\text{Ir}} \cos \alpha}}. \quad (1.4)$$

It is evident that moiré unit cell will have its maximum size if the two lattices are aligned (for R0 graphene i.e. $\alpha = 0^\circ$). In Appendix B we have modeled the Gr/Ir(111) moiré superstructures and the corresponding Fourier transforms for angles $\alpha = 0^\circ$ and 30° . The moiré acts as an magnifying tool as can be deduced from Eqs. 1.3 and 1.4: small changes in e.g. graphene lattice constant or its relative orientation with respect to iridium are ~ 10 times magnified and reflected in the size and orientation of the moiré structure [41, 45].

1.3.2 Binding strength and interaction with iridium

Characteristic electronic structure of graphene is preserved in the Gr/Ir(111) system which is also reflected in almost intrinsic Dirac cone bands [46–48]. This is illustrated in Fig. 1.6(b) where we show the electronic structure of Gr/Ir(111) in the vicinity of K point and close to the E_{F} . Immediately, one can notice two linear branches of the Dirac cone meeting at 0.1 eV above the E_{F} [46] making graphene on Ir(111) slightly p -doped. In addition, mini-gaps (cf. white arrows) and replicas of the Dirac cone (cf. marker R) can be noticed which exist due to the periodic potential introduced into the system by moiré superstructure (see also Refs. [47, 48]).

An important feature of Gr/Ir(111) is the absence of iridium electronic bands in the vicinity of the K point of graphene below the Fermi level [see Fig. 1.6(a)] [46, 49]. As

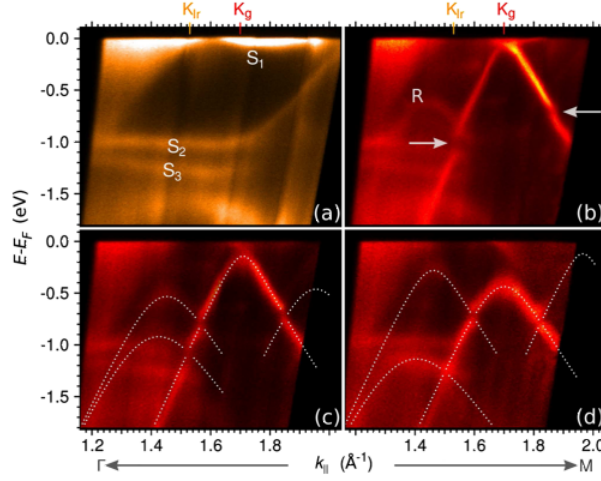


Figure 1.6: Photoemission spectra recorded in the vicinity of the K point of graphene (a) before and (b-d) after graphene formation on Ir(111). In (b), a well-defined Dirac cone is visible with the Dirac point located at 0.1 eV above E_F . Due to the moiré superstructure, mini-gaps (white arrows) and replica bands (marked by R) form. Azimuthal offsets $\Delta\phi$ with respect to ΓK direction: 0.5° in (a) and (b), 1.4° in (c) and 3.0° in (d). Adopted from Ref. [46].

a consequence, majority of the Dirac cone does not interact with the iridium states and remains intact. However, a study by Starodub et al. suggests that the iridium surface state located at the Fermi level [cf. state S_1 in Fig. 1.6(a)] hybridizes with the Dirac cone [50]. This hybridization scenario also supported by vdW-DFT (van der Waals-density functional theory) calculations of Busse et al. [51] who showed that the binding of graphene to iridium is predominantly physisorption with the addition of chemical, covalent-like bonding in the hcp and fcc regions of the moiré cell. In those regions, $C(2p_z)$ and $Ir(5d_{3z^2-r^2})$ orbitals hybridize and result in charge accumulation between C and Ir atoms. Most of the accumulated charge originates from C atoms, causing p -doping of graphene. Overall, the binding energy of graphene to iridium is 50 meV per C atom which is higher than 31 meV per C atom found for graphite [52] but can be still categorized as weak binding. The average Gr-Ir distance is 3.38 Å [51], is very close to the distance between adjacent layers in graphite (3.36 Å) and is an additional indicator of a weak binding to the substrate.

We point the reader to Refs. [14] and [13] and references therein for additional information on binding strength, morphology and electronic structure of epitaxial graphene on other metal surfaces.

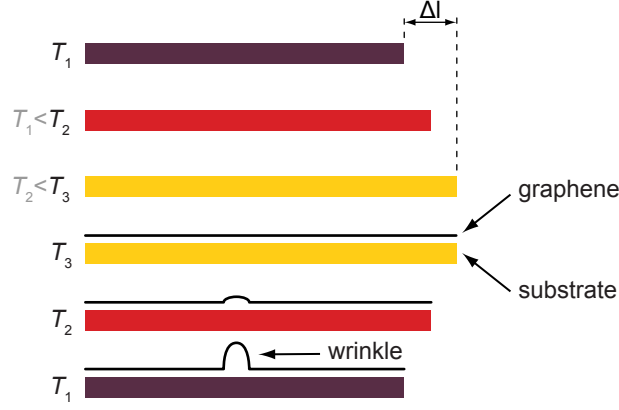


Figure 1.7: Illustration of a wrinkle formation process. The substrate temperature is increased from room temperature (T_1) to high temperatures (T_3 , typically in the 1070–1570 K range) which are suitable for graphene synthesis. During this process, the substrate expands by Δl . After the graphene is formed at T_3 , the sample is cooled down to T_1 which is accompanied by its contraction by Δl . Graphene, now bounded epitaxially to the substrate surface, contracts much less in the cooling process because the thermal expansion coefficient of graphene is much smaller than that of the substrate. The accumulated stress within the graphene sheet is at a certain point (T_2) released in the form of wrinkles.

1.4 Stress relaxation in epitaxial graphene

Growth of epitaxial graphene takes place at high substrate temperatures. During cooldown, the substrate contracts in accordance with its thermal expansion (contraction) coefficient. Since graphene's thermal expansion coefficient is negligible, during cooldown a compressive stress builds up inside the graphene layer which is relaxed at a certain point through the formation of so-called wrinkles (sometimes also referred to as ridges or folds). This is schematically illustrated for one-dimensional case in Fig. 1.7. Wrinkles are delaminated parts of graphene which extend in the direction perpendicular to graphene plane [cf. Fig. 1.8(c) and (d)] but can be thought of as basically 1D objects on the scale of micrometers [cf. Fig. 1.8(b)]. Many epitaxial graphene systems exhibit wrinkles [9, 53–57] and Gr/Ir(111) is no exception [44, 45, 58]. In transferred graphene systems, additional wrinkles can be induced solely due to the mechanical manipulation of graphene [59]. It is documented that wrinkles relate to several important properties of graphene, including transport [60–62] as well as the chemical reactivity e.g. resistivity against oxygen etching [63]. Therefore, control over graphene wrinkles is desirable for future nanofabrication and electronic device implementation of graphene. Some concrete efforts have already been made in that direction, e.g. manipulation of wrinkle orientation and length for graphene

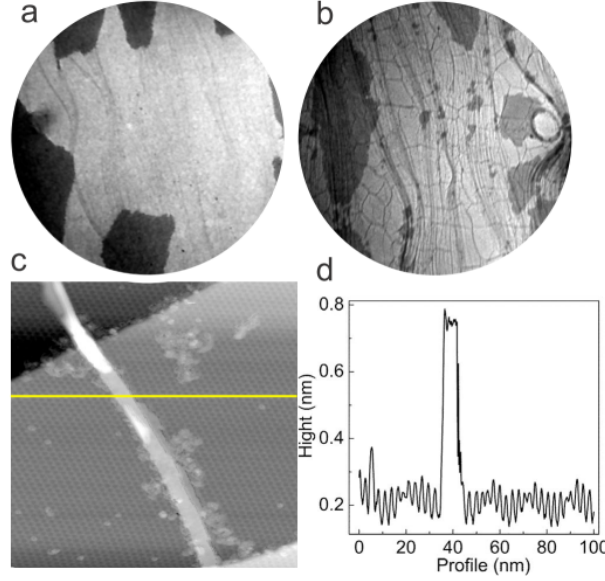


Figure 1.8: (a), (b) LEEM images of Gr/Ir(111) recorded at 1200 K and 300 K, respectively. In (b) wrinkles are visible as an interconnected network of 1D features. FOV = 20 μm . (c) STM topograph (100 nm \times 100 nm) of graphene area containing a wrinkle. (d) A profile along the yellow line from (c). Adopted from Ref. [44].

on 6H-SiC(0001) by STM tip [56] or modification of areal wrinkle density by selecting the substrate roughness for transferred graphene [64].

An experimental characterization of wrinkles on Gr/Ir(111) via LEEM and a simplified 1D theoretical model of wrinkle formation has been reported in the work of N'Diaye et al. [58]. It should be emphasized that the authors there study only wrinkles on graphene islands or graphene layers containing several rotational domains. Similar type of samples were also investigated in Ref. [44]. A detailed study on the relation between lattice parameters of graphene and iridium in a broad temperature interval [45] revealed a hysteretic behavior of wrinkle appearance/disappearance and proved that wrinkling is indeed a result of stress relaxation in graphene. Finally, it is clearly shown that wrinkles on the average relax $\sim 2/3$ of the compressive strain imposed by iridium, while $\sim 1/3$ still remains in the graphene layer.

From the characterization reported so far, typical height and width of the wrinkles are found to vary from below one nanometer up to ~ 10 nanometers, depending on the substrate and the preparation procedure. But their internal structure is very scarcely investigated. This can partly be ascribed to the fact that wrinkles, being relatively high objects with respect to their surroundings, can be difficult to image with scanning probe techniques. Reported wrinkle profiles are most often considered to be similar to semi-

circular forms [44, 57, 58]. At first, the semi-circular profile seems to be energetically stable shape for wrinkles, but one has to bear in mind the importance of additional interactions, such as van der Waals interaction, which can lead to the formation of more complex folded structures as reported in Refs. [60, 65].

Fig. 1.8(b) already indicates that wrinkles form a complex network consisting of straight, interconnecting segments. A comprehensive description of such network is still not given neither it is known if some sort of ordering can be found in it. For example, a statistical analysis of wrinkles network would be a source of relevant information since it could provide us with parameters useful for categorization of such complex structures.

1.5 Graphene islands

Besides a full coverage, epitaxial graphene can be synthesized at partial coverage, when it consists of graphene islands sometimes also referred to as graphene flakes. One particularly suitable approach in achieving this is by performing the temperature programmed growth (TPG), where first a carbonaceous precursor is adsorbed at room temperature on crystal surface which is followed by annealing to high temperatures (see Section 2.1 for preparation details). Typical dimensions of graphene islands depend on the annealing temperature and the number of TPG cycles used for synthesis. If these dimensions are as small as few nanometers, the islands are then called graphene quantum dots because at such small dimensions the effects of quantum confinement become pronounced. A detailed STM study on the morphology of graphene islands is given in Ref. [66]. TPG temperature the authors report on as being sufficient for graphene formation are in the interval between 870 and 970 K. This is in agreement with the study of Lizzit and Baraldi [67] where the authors ramp the temperature of ethylene-saturated iridium (111) surface and detect a clear graphene XPS signal after the sample reached ~ 900 K. Also, STM analysis revealed that only for TPGs conducted at 970 K or more, iridium $\langle 10\bar{1} \rangle$ and graphene $\langle 11\bar{2}0 \rangle$ directions are aligned and a characteristic moiré pattern is then resolved. Due to graphene island ripening, higher annealing temperature yields larger islands and lower island density (i.e. the number of islands per unit area). But regardless of the annealing temperature, a single TPG cycle results in graphene coverage of about 22% [66] which should be taken as an estimation because of the limited sample area available in STM

imaging. For obtaining more accurate results, area-averaging techniques (such as ARPES, see Section 3.2) should be employed. We note that graphene islands can also be formed by another growth process (chemical vapor deposition, see Section 2.1 for more information) but in this thesis we will limit ourselves to TPG-grown islands due to better control of graphene coverage and average island size.

Published STM data indicate that majority of graphene islands nucleate at iridium step edges. Furthermore, it was observed that these island grind into step edges and that significantly change the topography of Ir surface. Such behavior is an indication for relatively strong interaction of C edge atoms and Ir atoms. Indeed, a combined XPS and DFT study showed that graphene islands most strongly interact with iridium at the edges where an interaction of C $2p$ and top-layer Ir d band takes place [68]. It follows from this that the average interaction per C atom between graphene islands and iridium will be the strongest when graphene edge density is the highest. An increased binding of graphene edges to iridium is also experimentally evidenced in e.g. O intercalation experiments [69].

Graphene quantum dots can serve to explore and demonstrate some of the basic principles of quantum mechanics such as energy discretization and wavefunction visualization. In several studies the confinement of electrons on graphene quantum dots was investigated by STM, STS and also theoretical modeling [70–73]. The key observation made in all those studies were standing electron waves inside the quantum dots which are a realistic example of quantum particle-in-a-box model. By means of spatial visualization of electronic states via STS, discretized dispersions were obtained which are attributed to either linear Dirac cone [70–72] or the surface state of iridium [73]. An additional discrepancy in those studies is found for the value of Fermi velocity and positions of the Dirac point. Hence, true nature of the observed confined states is still not resolved and their additional investigation is necessary.

1.6 Intercalation related effects

One of the most frequent routes used for the modification of epitaxial graphene's properties is intercalation and as such is interesting from several different aspects. One of them is decoupling of graphene from the substrate by reducing the bonding interaction [11, 74, 75], but also an increase of the interaction can be induced [76]. An effect characteristic for

nearly all intercalated systems is chemical doping of graphene [77] which stems from the charge transfer to (from) graphene yielding n -type (p -type) electron doping. Due to the low density of states of graphene at the Fermi level, even small charge transfer results in notable shift of the Dirac point. The exact shift of the Dirac point depends on the amount and type of the intercalated species and it has been shown that the electronic states can be filled up to the van Hove singularities found at the M points of graphene band structure [78].

Intercalation effects are also of great importance for practical uses of graphene. A band gap opening has been reported for several intercalated systems [79–81] which is interesting from electronics point of view. Moreover, fabrication of novel graphene-based batteries and supercapacitors [82] is closely related to intercalation-induced effects. It was demonstrated that by precise control of the intercalation interface, laterally well-defined mesoscopic regions of n - and p -doped graphene—that is, $p-n$ graphene junctions—can be formed [83]. For spintronic applications, on one hand, intercalation of ferromagnetic 3d metals such as Co [84] or Ni [76, 85] has been explored; however, it results in a strong chemical interaction between the metal d -orbitals and π -bands of graphene. On the other hand, a more promising approach to design magnetic properties of graphene by using its almost unperturbed π -bands is the intercalation of a wider class of systems of the same nature—such as alkali metals, alkaline earth metals or lanthanides (for example, Nd or Eu that contain $4f$ and $6s$ electrons) [86].

In the case of Gr/Ir(111) it was shown that, despite macroscopic uniformity, different atoms and molecules can be successfully intercalated between graphene and iridium [69, 76, 84, 86–94]. The fact that graphene can be intercalated calls for an explanation on how the intercalation can occur through an apparently perfect graphene membrane. As an example, experiments and theoretical calculations showed that graphene represents an impermeable membrane to He atoms [95, 96]. This suggest that some sort of defects or cracks are necessary for the intercalation of graphene, as already proposed earlier [97]. These defects might be present on graphene prior to intercalation or they could be temporarily induced by the presence of deposited chemical species (particularly metals) which is then followed by self-healing of C-C bonds in graphene layer [85, 98, 99]. It seems that the exact pathway for the intercalation (preexisting defects or transient defects) is chosen based on the interaction strength of the intercalant atoms with carbon atoms [99].

For the intercalation of Gr islands with non-metallic elements such as O, studies point to the island edges as entry points for the intercalated atoms [63, 69].

Publications referenced in the preceding paragraph enlighten the process of intercalation only to a certain extent. Some important details, however, are still unknown. For example, it is not clear what is the driving force for the intercalation. Theoretical calculations show that for the penetration through graphene defects of various sizes a notable amount of energy has to be invested (up to 10 eV) [96, 100]. In addition, each C atom is on the average bound to Ir with 50 meV of binding i.e. delamination energy [51] which has to be compensated in order to push something in between Gr and Ir. So, in order to perform intercalation, all these energy costs need to be covered. Also, if intercalation takes place through various defects, it would be good to know what is their origin in order to potentially control their surface density and hence manipulate the intercalation process. In addition, more knowledge on the desorption of intercalated atoms (i.e. de-intercalation) would be desirable in order to fully understand all relevant aspects of intercalation of epitaxial graphene systems.

1.7 Objectives

At the end of the Introduction, we summarize the main goals which are to be fulfilled throughout this thesis. From the aspect of growth, we will monitor the evolution of occupied and unoccupied electronic structure (above and below the Fermi level) whilst increasing the coverage of iridium surface with graphene until one complete graphene layer is formed. This process is expected to result in the formation of characteristic graphene bands as well as partial modification of the iridium electronic states. Additional attention will be given to image-potential states located below the vacuum level. We will also characterize various structural features which are observed during the formation of a complete graphene layer with special emphasis on graphene wrinkles. The other task of this thesis is to clarify the mechanism and dynamics of intercalation of epitaxial graphene. Moreover, we want to investigate the intercalation effects of various species on the electronic structure and morphology of both graphene and iridium and how do these effects influence the interaction of graphene with its surroundings.

CHAPTER 2

Sample preparation and experimental methods

Detailed understanding of the sample preparation process and the working principle of techniques used for its characterization is utterly important in experimental work. We begin this chapter by describing synthesis procedures of graphene on iridium (111) surface. In all of our samples graphene was the main component and a primary point of interest and its properties were additionally modified in several ways as described below. The experimental methods used in this thesis can be divided into two groups: spectroscopies and microscopies. For the determination of the band structure we used angle-resolved photoemission spectroscopy (ARPES), two-photon photoemission spectroscopy (2PPE) and to a smaller extent scanning tunneling spectroscopy (STS). Sample structure and morphology was investigated by means of scanning tunneling microscopy (STM) and low energy electron microscopy (LEEM). Low energy electron diffraction (LEED) was used as an auxiliary technique in all experimental setups.

Sample preparation and all experiments (unless otherwise noted) were performed in UHV conditions with a typical base pressure in the range between 10^{-11} and 10^{-10} mbar. The sample was heated by radiative and e-beam heating; Cooling below room temperatures was achieved either by closed-cycle helium refrigerator or a cryostat. The sample temperature was determined by means of thermocouple [C type (W-5% Re vs. W-26% Re) or K type (chromel vs. alumel)] which were in physical contact with the iridium crystal or via calibrated optical pyrometer.

2.1 Sample preparation and graphene growth procedures

A prerequisite for epitaxial graphene synthesis is the preparation of clean, well-defined substrate surface. In our case, (111) surface of iridium single-crystal was most often used; Several experiments were conducted with Ir(100). Crystals were obtained from Mateck GmbH, Germany. They are manufactured in a hat-shaped form with a typical diameter of 6 mm. Their orientation accuracy is better than 0.1° and purity is 99.99%. Regardless of the particular crystal in use, first noble-gas ion sputtering (most often Ar^+ ions) takes place with the ion energies in the range between 1 and 2 keV either at room temperature or at elevated temperatures (~ 870 K). Then several cycles of oxygen glowing and annealing are applied. During oxygen glowing, usually at 1120 K, vast majority of remaining dirt on the sample surface is oxidized and removed. Annealing (in the range between 1370 and 1570 K) ensures structural quality of the substrate and absence of any adsorbates. It should be emphasized that such cleaning procedure yields sample surface containing large terraces of specified crystal orientation separated by (most often) mono-atomic steps.

There are two main procedures we used for graphene preparation - temperature programmed growth (TPG) and chemical vapor deposition (CVD). Both of them rely on the fact that surfaces of many transition metals are catalitically active and can decompose hydrocarbons—at elevated temperatures—to their constituting atoms. As carbon precursor, we used either ethene (ethylene) or methane. TPG consists of adsorption of precursor on the substrate crystal at room temperature until saturation is achieved. Typical applied dose was 5×10^{-8} mbar of hydrocarbon during 50 s. Then, a short annealing follows (1070-1470 K range, 30 s) and results in the formation of graphene islands whose average size depends on the annealing temperature [66]. Single TPG cycle yields graphene coverage of about 0.2 ML and by repeating the cycle several times, graphene coverage increases and eventually almost full coverage (one monolayer, 1 ML) can be achieved. CVD procedure implies exposure of hot crystal substrate (~ 1120 K) to the carbon precursor for an extended period of time and results in 1 ML graphene samples if the exposure time is long enough (e.g. for a dose of 1×10^{-7} mbar of hydrocarbon during 15 min). In addition, various combinations of TPG and CVD procedures can be used to synthesize graphene samples of various coverage. To obtain high quality uniform 1 ML samples, we

employed TPG + CVD procedure which consists of just one TPG and one CVD cycle till full coverage [66]. For sub-monolayer graphene coverages, we repeated TPG procedure a certain number of times. It is important to note that the solubility of carbon in iridium is negligible [101] ($n(\text{C})/n(\text{Ir}) \approx 10^{-3}$ at 1300 K) which inhibits the growth of multilayer graphene. Namely, once the whole metal surface is covered with graphene, growth from the gaseous carbon precursor is no longer effective.

1 ML or sub-monolayer graphene samples were additionally modified by deposition of various chemical elements. Alkali metals (Cs, Li) were deposited from commercially available dispensers (SAES getters) with the sample held at room temperature. Typical flux values of alkali sources were $5 \times 10^{15} \text{ m}^{-2} \text{ s}^{-1}$ which were achieved by passing up to $\sim 9 \text{ A}$ of current (depending on the dispenser mounting) through the dispensers. For Eu deposition we used water cooled Knudsen cell heated at a temperature of 720 K (typical flux of the order of $1 \times 10^{16} \text{ m}^{-2} \text{ s}^{-1}$) with the sample held at 720 K. In O deposition experiments, molecular oxygen was introduced into the UHV chamber through a leak valve at a sample temperature of 520 K.

2.2 Angle-resolved photoemission spectroscopy

The ideal method for mapping the occupied electronic bandstructure of various surfaces is ARPES. The method is based on the photoemission process in which an incident photon of energy $\hbar\omega$ causes an electron to be ejected from the sample [see Fig. 2.1(a)]. After ejection, electron kinetic energy (E_{kin}) is determined by the analyzer. From the conservation of energy one can determine the binding energy (E_{B}) of an electron referenced to the Fermi level from the equation

$$E_{\text{B}} = \hbar\omega - E_{\text{kin}} - \Phi \quad (2.1)$$

where Φ is the work function of the sample [cf. Fig. 2.2(a)]. Obviously, the relation $\hbar\omega > \Phi$ must hold in order to achieve photoemission. Electron analyzers are electrostatic analyzers consisting of two concentric hemispheres which act as electrodes and to which a potential difference is applied [schematic is given in Fig. 2.1(a)]. In this way, electrons with different kinetic energies have different trajectories between the hemispheres and fall onto different positions on the detector. Moreover, a set of angles θ (polar angle),

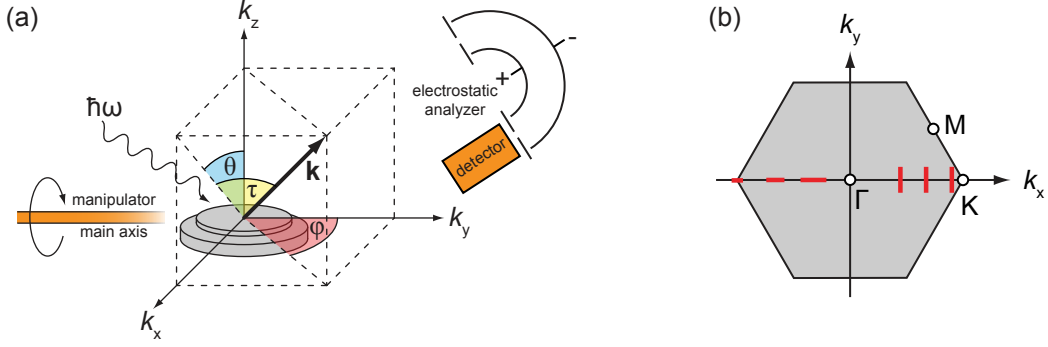


Figure 2.1: (a) A schematic of a photoemission experiment. Photons of well defined energy $\hbar\omega$ are directed onto the sample (gray, hat-shaped). The ejected photoelectrons, sampled by an electrostatic analyzer, can be characterized by the angles θ , φ and τ which are used in the calculation of k_x and k_y components of the electron wavevector \mathbf{k} . Orange rod in the $-k_y$ direction indicates the main axis of the sample manipulator. (b) Red lines indicate parts of the BZ which are probed in a single spectrum of the angle-resolved analyzer for six arbitrary polar angles θ . Vertical lines correspond to the pΓK geometry while horizontal lines correspond to the ΓK geometry in the experiment.

φ (azimuth) and τ (tilt) characterizing the direction of the electron wavevector \mathbf{k} [cf. Fig. 2.1(a)] can be determined from the relative position of the sample surface and the analyzer. Because the detector is two-dimensional, simultaneous detection of electrons entering the analyzer from a range of emission angles is possible.

In practice, two experimental geometries are most commonly used in ARPES setups:

- * ΓK (parallel to ΓK, \parallel ΓK): the analyzer entrance slit is oriented perpendicular to the main manipulator axis i.e. angle τ of the analyzed electrons is zero. For the case shown in Fig. 2.1(a) the components of the wavevector \mathbf{k} parallel to the sample surface are $k_x = |\mathbf{k}| \sin \theta$ and $k_y = 0$.
- * pΓK (perpendicular to ΓK, \perp ΓK): the analyzer entrance slit is oriented parallel to the main manipulator axis. Again referencing to Fig. 2.1(a), the components of the wavevector \mathbf{k} parallel to the sample surface are $k_x = |\mathbf{k}| \cos \tau \sin \theta$ and $k_y = |\mathbf{k}| \sin \tau$.

The components of the electron wavevector \mathbf{k} parallel to the sample surface are conserved in the process of photoemission [102]. Knowing the relation $|\mathbf{k}| = \frac{1}{\hbar} \sqrt{2m_e E_{\text{kin}}}$ and by measuring the kinetic energy and trajectory angles of the photoemitted electrons, we can obtain the 2D dispersion relation $E_B(k_x, k_y)$. Parts of the BZ which are reachable in one photoemission spectrum in both geometries are indicated in Fig. 2.1(b). We note that in our experiments conducted in the ΓK geometry, due to the mechanical restrictions of our sample holder, a very fine adjustment of the azimuthal angle is often difficult

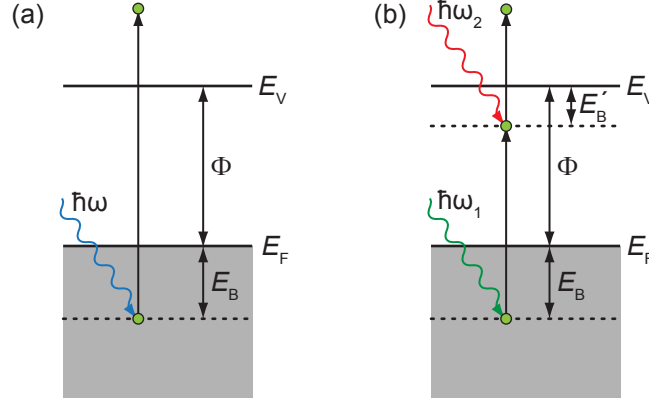


Figure 2.2: (a) A simple energy diagram of the photoemission process. Energy of the incoming photon is transferred to the electron which is ejected from the sample into the vacuum. (b) An energy diagram of the two-photon photoemission process. A pump photon excites the electron to an unoccupied band below the vacuum level. An additional probe photon provides the electron with enough energy to escape from the sample.

which typically leads to a small misalignment (up to $\sim 1^\circ$) of the desired and actual scan directions in the BZ. In other words, the precision of reaching e.g. certain high symmetry point of the BZ is limited by this potential misalignment.

The intensity in ARPES spectra is proportional to the single-particle spectral function which in the case of a system of interacting particles has the form

$$A(\mathbf{k}, E) = \frac{1}{\pi} \frac{\Im[\Sigma(\mathbf{k}, E)]}{\{E - E_{\mathbf{k}}^0 - \Re[\Sigma(\mathbf{k}, E)]\}^2 + \{\Im[\Sigma(\mathbf{k}, E)]\}^2} \quad (2.2)$$

where $\Sigma(\mathbf{k}, E)$ is the quasiparticle self-energy and $E_{\mathbf{k}}^0$ is the electronic dispersion relation in a system of non-interacting particles. Since the self-energy function reflects the interactions in a many-body system, ARPES spectra can be directly used to characterize those interactions (see e.g. [103]). Each multidimensional ARPES spectrum (energy, wavevector and photoemission intensity) can be reduced to 2D representation if (i) the photoemission intensity is plotted as a function of energy for a particular wavevector (energy distribution curve or EDC) or if (ii) the photoemission intensity is plotted as a function of wavevector for a particular energy (momentum distribution curve or MDC). Those two types of curves are used for fitting the band profiles to a particular peak curves, usually Lorentzian curves, providing information on e.g. full width at half maximum (FWHM) of the band and its exact position in the (\mathbf{k}, E) space.

Our ARPES experiments were conducted in several laboratories: (i) ARPES-dedicated setup in the Laboratory for Surface Science and Supported Nanostructures at Institute

of Physics, Zagreb, Croatia (figure caption abbreviation: Zg-ARPES). Both Γ K and p Γ K geometries were utilized in this setup. Helium discharge lamp ($\hbar\omega = 21.2$ eV) was used for excitation. Analyzer type: Scienta SES100 (25 meV energy and 0.2° angular resolution). (ii) APE beamline of the Elettra synchrotron near Trieste, Italy (figure caption abbreviation: Elt-ARPES). Data was collected in the Γ K geometry. Analyzer type: Scienta SES2002 (10-20 meV energy and 0.2° angular resolution). (iii) U13UB beamline of the NSLS synchrotron at Brookhaven National Laboratory, Upton, USA (figure caption abbreviation: BNL-ARPES). There, the p Γ K geometry was used in data acquisition. Analyzer type: Scienta SES2002 (10 meV energy and 0.14° angular resolution). In addition, light polarization was well defined at synchrotron facilities which was not the case for noble gas discharge lamp.

Further reading on ARPES:

- * *Photoelectron Spectroscopy: Principles and Applications* by S. Hüfner [102]
- * *Very High Resolution Photoelectron Spectroscopy* by S. Hüfner (ed.) [104]
- * *Advanced photoelectric effect experiment beamline at Elettra: A surface science laboratory coupled with Synchrotron Radiation* by G. Panaccione et al. [105]

2.3 Two-photon photoemission spectroscopy

Characterization of the unoccupied electronic structure is not possible with ARPES because photon excitation ejects the electrons directly into the vacuum. For unoccupied states we employ 2PPE which uses two photons in order to gather the information about the electronic states above the E_F . Fig. 2.2(b) displays the energy diagram of the process: photon $\hbar\omega_1$ (pump pulse) excites an electron from below the E_F to some intermediate, unoccupied state between the E_F and vacuum level (E_V). Then the second photon $\hbar\omega_2$ (probe pulse) is used to eject the electron above the E_V and enables its detection. Photons $\hbar\omega_1$ and $\hbar\omega_2$ can come to the sample at the same time or with a time lag Δt with respect to each other. In the latter case, 2PPE becomes time-resolved and can be used to investigate electron dynamics at surfaces. If $\hbar\omega_1 = \hbar\omega_2$ then 2PPE is monochromatic while it is bichromatic if $\hbar\omega_1 \neq \hbar\omega_2$.

The principle of detection of photoelectrons is the same as in the case of ARPES described in the Section 2.2. By measuring the kinetic energy and the ejection angle of

the electrons, electronic dispersion $E'_B(k_x, k_y)$ of the unoccupied band can be obtained. In each EDC slice of 2PPE spectrum two characteristic cutoffs can be found: (i) low-energy cutoff at $E_{\text{kin}} = 0$ which is formed by one-photon photoemission of the electrons excited thermally above the Fermi level and (ii) high-energy cutoff (which actually coincides with the vacuum level) formed by 2PPE of the electrons from the Fermi level [cf. Fig. 2.2(b) for the case $\hbar\omega_1 = \hbar\omega_2 = \hbar\omega \approx \Phi$]. Taking this into account, the work function of the sample can be simply expressed as

$$\Phi = 2\hbar\omega - \Delta E \quad (2.3)$$

where ΔE is the separation of high- and low-energy cutoffs.

We performed monochromatic 2PPE experiments at Columbia University, New York, USA. Ti:sapphire laser at 250 kHz repetition rate drove an optical parametric amplifier whose output pulses were frequency doubled to generate tunable UV p -polarized pulses in the energy interval $3.8 < \hbar\omega < 4.9$ eV. Bandwidth of the pulses was ~ 20 meV, duration 90 fs and energy ~ 1 nJ. A spherical-sector energy analyzer with 50 meV energy resolution was used for data acquisition. The detector was one dimensional and angular resolution of the experiment was achieved by rotating the sample in steps of 1° . The sample was biased at -4 V to reduce the effects of stray fields.

Further reading on 2PPE:

- * *Two-photon photoemission spectroscopy of image states* by T. Fauster and W. Steinmann [30]
- * *Two-Photon Photoelectron Spectroscopy* by T. Fauster [106]
- * *Theory of two-photon photoemission spectroscopy of surfaces* by H. Ueba and B. Gumhalter [107]

2.4 Scanning tunneling microscopy and spectroscopy

Based on the quantum-mechanical phenomenon of tunneling through a potential barrier, STM and STS enable resolving morphological and spectroscopic features of the sample surface with lateral resolution at the atomic level. The working principle of the corresponding instrument is sketched in Fig. 2.3. An atomically-sharp metal tip is brought in the close vicinity of the sample surface which must also be electrically conducting (metal

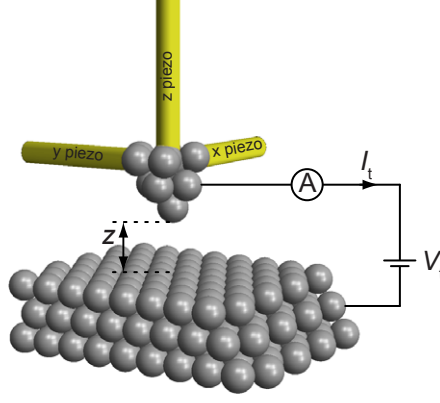


Figure 2.3: Working schematic of an STM. The tip is brought close to the sample which enables the tunneling of electrons between them and hence the tunneling current I_t when the voltage V_t is applied. The lateral and vertical movement of the tip is controlled by the piezo elements.

or semiconductor) so that a significant overlap of the corresponding wavefunctions exists. The voltage V_t is applied between the tip and the sample which causes tunneling of the electrons between them i.e. the flow of the current I_t . By applying several approximations [108], it can be shown that the tunneling current has the form

$$I_t = \frac{4\pi e}{\hbar} \int_0^{eV_t} \rho_T(E_F^T - eV_t + \epsilon) \rho_S(E_F^S + \epsilon) \exp(-2kz) d\epsilon. \quad (2.4)$$

ρ_T and ρ_S are local densities of states (LDOS) of the tip and the sample, z is tip-sample distance and the coefficient k is given by

$$k \cong \sqrt{\frac{m_e (\Phi_T + \Phi_S + eV_t)}{\hbar}} \quad (2.5)$$

where Φ_T and Φ_S are the work function of the tip and the sample. Scanning the tip laterally (x and y directions) and vertically (z direction) by means of piezoelements, the tunneling current is recorded as a function of the tip position. We see that the information contained in the STM image depends on ρ_S and a large LDOS corresponds to a large number of electronic states available for tunneling which contribute to I_t . That is why the height information in STM images has to be interpreted with care. Generally, STM can work in one of the two modes: constant current ($I_t = \text{const.}$) or constant height mode (the tip does not move vertically). Depending on the type of the sample and the desired scanning speed, one of these two modes is employed during STM measurements.

We see from Eq. 2.4 that the tunneling current drops exponentially with the increasing

tip-sample distance, $I_t \propto \exp(-2kz)$. If one assumes that the state of the tip remains unchanged during data acquisition, the work function difference on different positions of the sample can be obtained from Eq. 2.4 and 2.5 by measuring the corresponding $I_t(z)$ curves (see e.g. Ref. [109] for details). Often only LDOS (and not the topography of the sample) is of interest since it is closely related to the electronic band structure of the sample. In order to obtain this kind of information, STS is performed. In particular, we used so-called dI_t/dV_t spectroscopy which results in dI_t/dV_t curves (describing LDOS at certain point) or dI_t/dV_t maps (describing DOS at a certain energy over a predefined area of the sample). The sought dI_t/dV_t signal, which is proportional to the density of states of the sample, is obtained by applying sinusoidal tunneling voltage V_t and using a lock-in amplifier for signal extraction.

STM measurements were performed in: (i) low-temperature STM setup (CreaTec LT-STM) in Cologne, Germany. We also used this setup for dI_t/dV_t spectroscopy and $I_t(z)$ measurements. All data were recorded at temperatures $T_S < 10$ K. (ii) variable-temperature STM (SPECS Aarhus STM) in the Laboratory for Surface Science and Supported Nanostructures at Institute of Physics, Zagreb, Croatia. In this setup the data was recorded at room temperature. In both cases, STM data analysis was done in WSxM software [110].

Further reading on STM and STS:

- * *Introduction to scanning tunneling microscopy* by C. Julian Chen [111]
- * *Scanning Tunneling Microscopy* by A. Della Pia & G. Costantini [108]
- * *Scanning tunnelling microscopy studies of metal surfaces* by F. Besenbacher [112]

2.5 Low energy electron microscopy

Unlike in most other electron microscopes, LEEM uses low energy electrons for sample probing in order to enhance surface sensitivity. Electrons are emitted from the electron gun, are accelerated (typically to the energy of 20 keV) and focused on the sample by the objective [see blue dashed line in Fig. 2.4]. Before reaching the sample, the electrons are decelerated by the electric field which is set up between the objective and the sample to just a few eV which makes them surface-sensitive. After reflection from the sample

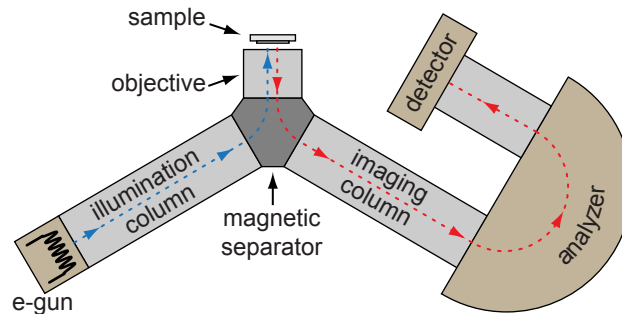


Figure 2.4: A schematic of a LEEM instrument equipped with an energy analyzer. Blue and red lines indicate trajectories of the incoming and outgoing electron beams, respectively.

surface electrons are once more accelerated to high energies (by the same electric field which previously decelerated them), they travel back through the objective lens and are deflected towards the analyzer and afterward to the detector [see red dashed line in Fig. 2.4]. If the sample has a crystal structure, electron reflection from the surface is in principle diffraction resulting in the formation of a diffraction image of the sample in the back focal plane of the objective which can also be recorded as such. One of the key parts of the microscope is the beam separator which is used for separation of the incoming and the reflected electron beams and enables realization of the reflective geometry of the microscope.

Besides LEEM, such instrument is also capable of other kinds of measurements. From a series of images recorded at different electron energies, so-called *IV*-LEEM series, reflectivity vs. energy curves can be extracted which have a spectroscopic character. By virtue of several illumination apertures in the illumination column (providing 80, 20, 8 and 2 μm electron beam sizes on the sample), micro-LEED (μ -LEED) characterization of micrometer-sized sample areas is available. Several other techniques can be employed in LEEM-dedicated setup [(X)PEEM, μ -ARPES, XPS, SPLEEM, MEM; For more information see the end of this section] making such instrument a versatile tool for sample characterization.

An important feature of LEEM is in the ability to perform *in situ* real-time measurements during processes which are relevant for sample preparation (e.g. deposition, heating, exposure to gases etc.). In this why the dynamics on the surfaces can also be investigated with this instrument. The contrast in LEEM images comes about from different diffraction conditions on the sample i.e. different crystal structure, interference between reflected electron waves or simply from incoherent scattering by well-defined,

sharp structures on the sample surface [113]. As in other electron microscopes, images can be recorded in the bright field [when (0,0) diffraction maximum is used for imaging] or dark field mode (when higher order diffraction maxima is used for imaging) by adjusting the contrast aperture size and position in the imaging column.

The instrument we used in this work is a commercial Elmitec LEEM III system equipped with an energy analyzer, installed at U5UA beamline at NSLS synchrotron at Brookhaven National Laboratory, Upton, USA. Spatial resolution of the microscope was ~ 10 nm. All LEEM data shown in this thesis is recorded in the bright field mode unless otherwise stated in the figure caption.

Further reading on LEEM:

- * *Low energy electron microscopy* by E. Bauer [114]
- * *Trends in low energy electron microscopy* by M. S. Altman [113]
- * *Low energy electron microscopy and photoemission electron microscopy investigation of graphene* by K. L. Man and M. S. Altman [115]

2.6 Low energy electron diffraction

Most UHV chambers have LEED available on them since it provides basic information about the surface structure of the sample. The technique utilizes the fact that electrons scatter elastically from the sample and form a diffraction pattern if the sample has well-defined crystal structure. Since electrons of low energy are used, the method is surface sensitive and enables e.g. monitoring of superstructure formation and rough estimation of the quantity of deposited material on the sample. Also, the quality and contamination of sample surface can be determined, which is often useful during sample preparation. We refrain from a detailed description of the LEED apparatus, for more information we point the reader to the references given below.

Further reading on LEED:

- * *Modern techniques of surface science* by D. P. Woodruff and T. A. Delchar [116]
- * *Low-energy Electron Diffraction (LEED)* by G. Held [117]

CHAPTER 3

Microscopic characterization of graphene growth

Despite substantial amount of information which can be found on synthesis of graphene on Ir(111) (see Chapter 1 and references therein), a systematic analysis of graphene at various intermediate stages of growth is still missing. Also, details on the work function modification of Gr/Ir(111) system upon graphene growth are also not complete. For full monolayer graphene, a thorough analysis of wrinkles network as well as their internal structure is needed for a complete description of its properties, especially in terms of potential future applications.

In this chapter results concerning structural and electronic-band evolution during an increase of graphene coverage θ_{Gr} in the $0 \text{ ML} < \theta_{\text{Gr}} < 1 \text{ ML}$ range are presented. Variable coverage is achieved by repeating TPG growth cycle a given number of times (θ_{Gr} increases after each cycle). Spatial growth was monitored by STM (nanometer scales) and LEEM (micrometer scales). We show LEEM results of graphene growth on Ir(100) as an example of growth on non-hexagonal substrate. Changes in the electronic structure of both Gr and Ir are characterized by ARPES with focus directed to the K point of graphene. Sample work function, which can be studied locally on the nanometer scale or as averaged on larger scales is also investigated as a function of variable θ_{Gr} . We gathered substantial amount of LEEM data on the interconnecting network of graphene wrinkles which resulted in clarification of network's main features. Real-time microscopy enabled observation of wrinkling dynamics and local stress relaxation in a complete graphene layer. In addition, STM images of individual wrinkles provide a detailed insight into the internal structure

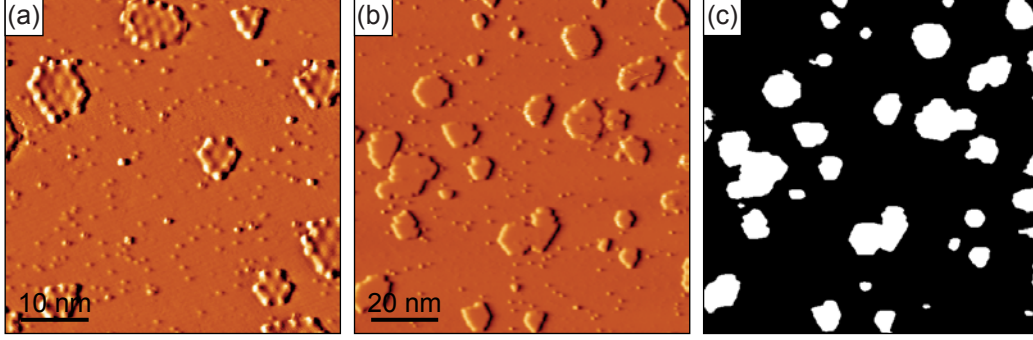


Figure 3.1: (a), (b) STM images of graphene flakes on Ir(111) after one TPG cycle at 1120 K. First derivative of the data is shown so that the structures appear to be illuminated from the left. In (a) $U_t = 160$ mV, $I_t = 0.18$ nA, in (b) $U_t = 1.8$ V, $I_t = 1.6$ nA. (c) Thresholded image of the non-differentiated figure from (b) where white areas represent graphene flakes.

of wrinkles which turned out to be more complex than previously thought.

3.1 Morphological analysis

3.1.1 STM results

In Section 2.1 we described the TPG procedure which yields graphene islands of various sizes; Here we focus on their morphology starting with STM characterization. In Fig. 3.1 we show two characteristic areas on the sample surface after one TPG cycle performed at 1120 K. In panel (a) several flakes are visible and on most of them a characteristic moiré pattern can be resolved. Small specks that are randomly distributed across the surface are most likely segregated dirt particles leftover after sample cool-down. In panel (b) we show different, two times larger area on the same sample. By using the threshold technique [see panel (c)], we calculated that $\sim 16\%$ of the iridium surface is covered by graphene. An average flake size is ~ 10 nm, as expected from previous studies [66].

It is known from previous STM experiments [66] that after each TPG cycle a fraction f of bare iridium surface is covered with graphene. The graphene coverage after N cycles can then be written as $\theta_{\text{Gr}}(N) = \theta_{\text{Gr}}(N-1) + f[1 - \theta_{\text{Gr}}(N-1)]$. The solution to this linear recurrence of the first order is $\theta_{\text{Gr}}(N) = 1 - (1-f)^N$ with the starting condition $\theta_{\text{Gr}}(0) = 0$ [47]. Further simplification of the solution can be made by using substitution $f = 1 - e^{-\lambda}$ which yields

$$\theta_{\text{Gr}}(N) = 1 - e^{-\lambda N}. \quad (3.1)$$

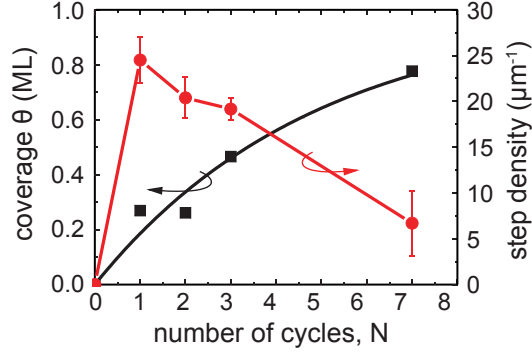


Figure 3.2: Graphene coverage extracted from a set of $(1 \times 1) \mu\text{m}^2$ STM images (cf. Fig. 1 in Ref. [47]) and the corresponding exponential fit (black squares and black line). From the same STM data, graphene step-edge density (red circles) is also obtained. Red line is a guide to the eye. Adopted from Ref. [47].

We see that the graphene coverage exponentially approaches unity as the number of TPG cycles N increases with the growth rate quantified by λ . The values of λ and f can be obtained by extracting graphene coverage from the STM images for several different graphene coverages and by using Eq. 3.1 for fitting the data. This kind of analysis was performed in Ref. [47] after $N = 1, 2, 3$ and 7 TPG cycles conducted at 1470 K. The resulting data (black squares) together with the corresponding exponential fit are shown in Fig. 3.2. Fitting yields the value $\lambda_{\text{STM}} = 0.21 \pm 0.02$. From this it follows that after each TPG cycle a fraction of $f_{\text{STM}} = 1 - e^{-\lambda_{\text{STM}}} = 19\%$ of bare iridium is covered with graphene. We note that the exact determination of the growth parameters by STM is somewhat difficult because of spatial limitation to the maximum accessible area on the sample. Nevertheless, the fraction f calculated in this way is in good agreement with previously found value obtained from $1 \times \text{TPG}$ STM images [66] and moreover, it is certainly more reliable.

3.1.2 LEEM results

In order to characterize the TPG growth of graphene on micrometer scales which is more appropriate for higher graphene coverages, we recorded LEEM images after several consecutive TPG cycles. The resulting sequence is shown in Fig. 3.3. The first frame shows clean iridium surface. Steps are visible as wavy lines which extend across the crystal surface. LEEM imaging of graphene flakes after a single TPG cycle is not possible because their typical size coincides with ~ 10 nm resolution of the LEEM instrument (cf. Fig. 3.1). But after second TPG, well-defined graphene areas on iridium can be imaged by LEEM

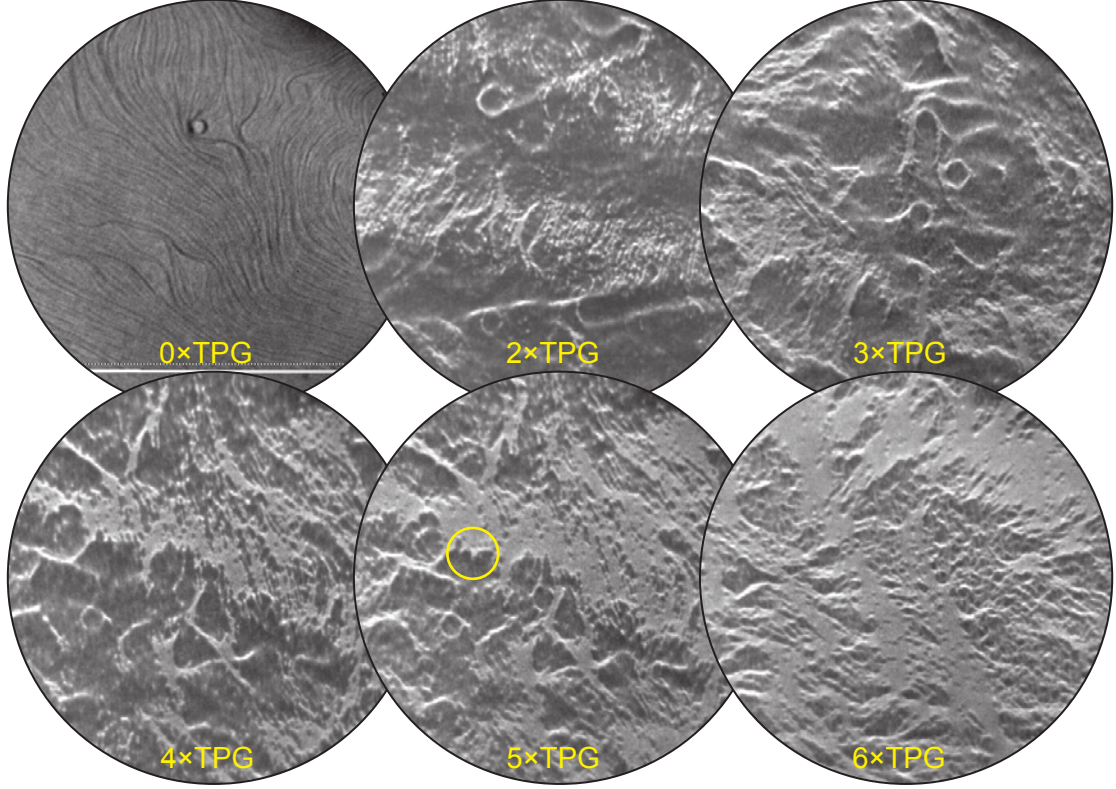


Figure 3.3: A set of six LEEM images showing the sample surface after a noted number of TPG cycles. Dark contrast corresponds to clean iridium whilst bright contrast corresponds to graphene. FOV = $9.3 \mu\text{m}$, $E = 4 \text{ eV}$, $T_S = 300 \text{ K}$.

(see bright contrast in the second frame of Fig. 3.3). Due to thermal drifting after each TPG step, frames in Fig. 3.3 shown different areas on the sample which prevents direct comparison of LEEM images. Nevertheless, looking at various graphene coverages shown in different frames (0-6 TPGs), the expansion of graphene area is obvious. On the average, graphene islands grown on iridium show random spatial distribution but locally there are inhomogeneities which can be spotted in LEEM. An example of this is highlighted by a yellow circle in 5xTPG frame where large graphene area is found next to clean iridium area. The possible reasons for such local inhomogeneity are imperfections of the iridium surface (meaning steps, step bunches and defects) which dictate local preference in graphene nucleation and the coalescence of small graphene islands at high synthesis temperatures (1470 K in this case) [66].

Next we analyze graphene area to determine the graphene coverage in each frame of Fig. 3.3 using the threshold technique. The resulting data points are shown in Fig. 3.4. Fitting the data to exponential growth (Eq. 3.1), we obtain the exponent of $\lambda_{\text{LEEM}} = (0.162 \pm 0.004)$. In addition, the STM growth curve is also plotted in Fig. 3.4. As can be

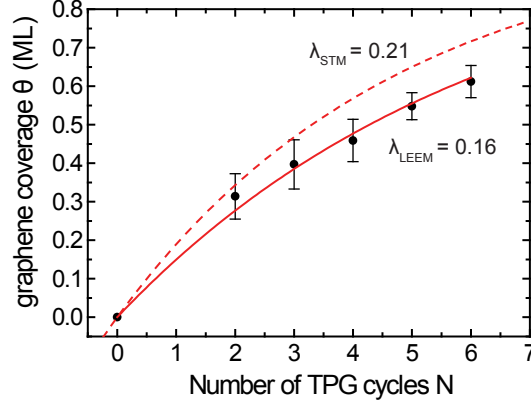


Figure 3.4: Graphene coverage as a function of number of TPG cycles extracted from the LEEM data shown in Fig. 3.3. Error bars originate from the uncertainty of threshold values used in each LEEM frame. Full line is a fit to the LEEM data, dashed line is a fit to the STM data as calculated in Ref. [47].

seen, growth rate determined by LEEM is lower. One of the major factors influencing this discrepancy is probably LEEM resolution which limits inclusion of small/narrow graphene areas to the total coverage. Also, graphene edges, being relatively sharp features, strongly scatter incoming electrons in LEEM which might lead to an underestimation of the total graphene area in our analysis. Because of this, λ_{LEEM} should be regarded as approximate.

3.1.3 Synthesis on Ir(100)

In addition to well known growth on (111) face of iridium, graphene can be grown on other crystal faces, including vicinal surfaces [118–120]. In scope of this work, we discuss some of the basic properties of graphene grown on Ir(100) and also present usefulness of LEEM dark field imaging in the characterization of graphene synthesis. The (100) surface of iridium exhibits several reconstructions [121, 122]. We shall focus on one of them—a (5×1) reconstruction resulting in a quasihexagonal packing of the top layer, so the exact notation for the substrate in this case is Ir(100)- (5×1) -hex. In addition, the crystal was deliberately produced with a very small miscut angle. In this way, large (100) - (5×1) -hex terraces are preserved (several hundreds of nanometers wide) and (5×1) reconstruction of the iridium surface is restricted to only one direction. This is confirmed by LEED pattern shown in Fig. 3.5(a).

We synthesized graphene on Ir(100) by CVD at 1120 K and recorded the corresponding LEED pattern over an area of $10 \mu\text{m}$ shown in Fig. 3.5(b). The well known (5×1) reconstruction of the underlying iridium [122] is removed by the formation of graphene

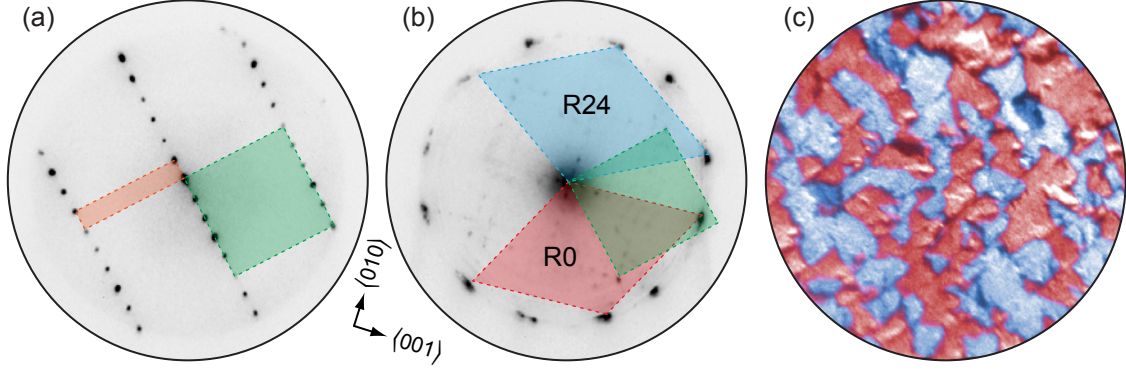


Figure 3.5: (a) LEED pattern of a Ir(100)-(5×1)-hex surface. Unit cells of Ir(100) (green) and (5×1) reconstruction (orange) are noted. $E = 40$ eV. (b) LEED pattern of Gr/Ir(100). Unit cells of Ir(100) (green) and two graphene rotations (red and blue) are marked. $E = 35$ eV. (c) Overlap of the two dark field LEEM images of Gr/Ir(100) formed by the first order diffraction maxima of the two graphene orientations visible in (b). Color coding (red and blue shades) is used for direct visualization of the two orientations. FOV = $9.3 \mu\text{m}$, $E = 32$ eV, $T_s = 388$ K.

as can be deduced by comparing diffraction spots in Fig. 3.5(a) and (b). In panel (b), sequences of new, faint diffraction spots are visible which are aligned to directions of the two diagonals of Ir(100) unit cell. These spots are identified with 2.1 nm periodic ripples of graphene [123]. The removal of (5×1) reconstruction is expected since (i) (100) surface of iridium is easily reconstructed by adsorption (e.g. hydrogen adsorption at low temperatures [121]) and (ii) during growth, graphene acts aggressively upon non-flat iridium areas (e.g. grinds into iridium step edges [66]).

From LEED pattern shown in Fig. 3.5(b) we see that graphene exhibits two principal orientations. One of them (red) is aligned within a few degrees to Ir $\langle 001 \rangle$ as was also found in Refs. [123, 124] and we will refer to it as R0. We observe another orientation (blue) which is rotated with respect to R0 by $\sim 24^\circ$ (R24) and which was not reported on before. However, two dominant graphene orientations were also found by Locatelli et al. [124] which are rotated by 30° with respect to each other. A discrepancy of 6° between those and our results could be attributed to a specific, vicinal Ir(100) we used in our experiments.

In order to visualize the spatial arrangement of the two domains identified in LEED, dark field LEEM imaging was performed. First order maxima of the two Gr orientations was utilized for LEEM image formation and the resulting composition image is shown in Fig. 3.5(c). Two graphene domains are clearly distinguished, each of them occupying roughly 50% of the recorded sample area. Typical sizes of individual grains are $\sim 1 \mu\text{m}$ or

less, which is in rough agreement with previous findings [124]. DFT calculations point to the fact that Gr on Ir(100) (R0 domains at least) is more strongly bound to the substrate as compared to e.g. Gr/Ir(111) [123]. This is evident from the non-vanishing density of states at the position of the Dirac point which is an indication of strong hybridization (and therefore chemisorption) between the Dirac cone and the iridium states. For comparison, weakly bound graphene on Pt(111) [125, 126] also exhibits two dominant graphene orientations. We therefore deduce that two-domain graphene growth is found in both strongly and weakly interacting graphene systems.

3.2 Evolution of the electronic structure

The electronic structure of a full layer ($\theta_{\text{Gr}} = 1$) of Gr/Ir(111) has been investigated by many groups by means of ARPES (see 1.3 and references therein). Also, the electronic properties of graphene flakes have been studied by scanning probe techniques [70–72]. However, the question remained open on how does the electronic structure of graphene and the underlying iridium change (especially in the vicinity of the K point) as the graphene coverage changes from 0 to 1 ML. In the following we describe this evolution based on our ARPES results recorded during a series of seventeen sequential TPG growth cycles performed at 1470 K. Fig. 3.6(a) shows several ARPES spectra recorded at the K point after a noted number of TPGs. The formation and a continuous increase of the Dirac cone intensity is evident, with the Dirac point situated at 1.7 \AA^{-1} . Yellow line in the $8 \times \text{TPG}$ panel marks k value of 1.784 \AA^{-1} where EDCs were extracted from all seventeen spectra. Those seventeen curves were merged into a single plot in Fig. 3.6(b) and show the evolution of two clearly resolved peaks: one close to the Fermi level belonging to the iridium surface state [49] and another at the lower energy belonging to the right branch of the Dirac cone. Obviously, with increasing number of TPG cycles, the peak intensity of iridium is reduced while the graphene peak intensity is increased. We also note the background intensity at energies below -0.4 eV which gets additionally reduced after each TPG cycle.

Making the analysis of peak intensities more quantitative, the EDC curves were fitted by two Lorentzian peaks of fixed position and width: for iridium at -0.07 eV with a FWHM of 0.13 eV and for graphene at -0.30 eV with a FWHM of 0.20 eV . Fig. 3.6(c)

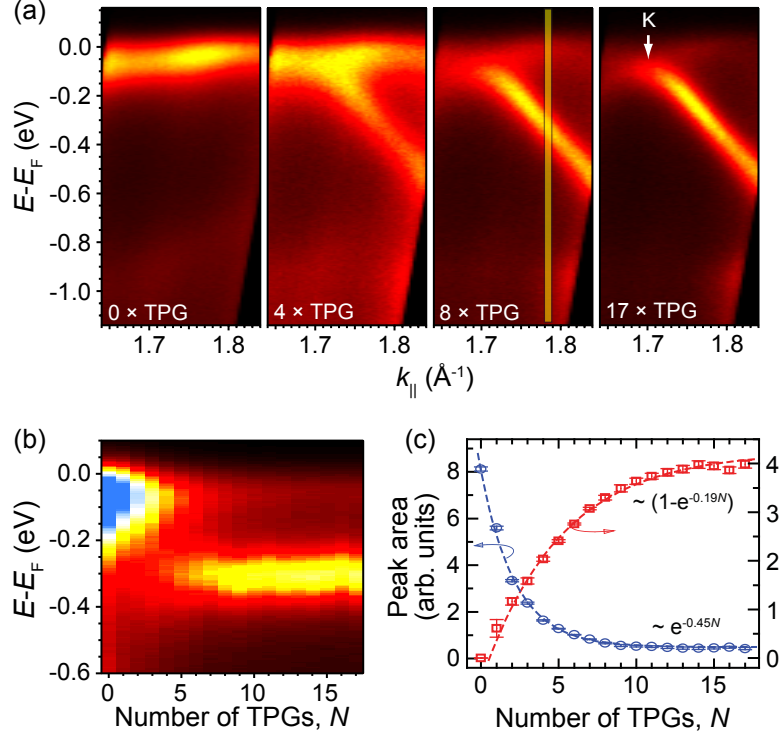


Figure 3.6: (a) ARPES spectra showing the Dirac cone intensity obtained after the indicated number of TPG cycles. Spectra are focused to the region of the K point of graphene’s BZ. Zg-ARPES, $\parallel \Gamma K$, $\hbar\omega = 21.2$ eV, mixed polarization, $T_S = 60$ K. (b) EDC cuts obtained from a series of seventeen spectra, some of them shown in (a), merged into a two-dimensional map. Cuts were taken at $k_{||} = 1.784 \text{ \AA}^{-1}$ [cf. yellow line in $8 \times \text{TPG}$ spectrum from (a)]. (c) Photoemission peak areas extracted from spectra in (b). Lines indicate fits of peak areas by noted exponential functions.

shows the areas of the fitted Lorentzian peaks (with linear background subtracted) plotted as a function of the number of TPG cycles. Both the iridium and graphene peak intensities exhibit clear saturation with the increasing number of TPG steps. We assume that the peak area associated with the cut through the Dirac cone, I_{Gr} , is proportional to the graphene coverage and following Eq. 3.1, the Dirac cone peak area is given by $I_{\text{Gr}}(N) \sim (1 - e^{-\lambda N})$. For fitting the graphene peak area, the zeroth cycle point was omitted and the value of $\lambda_{\text{Gr}} = \lambda_{\text{ARPES}} = 0.196 \pm 0.007$ is found. The corresponding fraction f equals 18%. Following the same logic as for the increase of graphene peak, for the iridium surface state peak we expect a decrease, $I_{\text{Ir}}(N) \sim e^{-\lambda N} + I_{\text{off}}$, where the offset intensity I_{off} is introduced as the intensity of the surface state must not decay to zero even for a fully covered surface. We find a value of $\lambda_{\text{Ir}} = 0.45 \pm 0.01$ with the iridium peak area offset being about 5% of its initial area at $N = 0$ i.e. iridium peak is suppressed to 5% of its initial intensity. We note that the same λ values are obtained if we do not freeze the position

of the iridium peak. In that case, the maximum of the iridium peak shifts monotonously with growing number of cycles towards the Fermi energy and the overall shift is around 0.025-0.030 eV. An explanation of this effect can be found in gradual p -doping of iridium surface state upon graphene formation. This idea is additionally strengthened by ARPES study which has demonstrated that another surface state of iridium located at the Γ point exhibits an upward shift of about 150 meV due to the presence of the graphene layer [127]. Likewise, a shift of the iridium surface state to higher binding energies due to the n -doping is found in several intercalated systems (see Sections 6.1 and 6.2). Much larger surface state shifts have been found for strongly chemisorbed graphene on Ru(0001) [128] where the smaller graphene-substrate separation and the different symmetry character of the state may be responsible for a more pronounced effect.

We see that the values λ_{STM} and λ_{ARPES} are very similar which confirms our assumption that the Dirac cone peak intensity is directly proportional to the graphene covered area. ARPES value should be taken as more accurate because it was obtained from a larger number of TPG cycles and the information is derived by integrating over a much larger area of the sample (determined by the UV lamp spot diameter on the sample, $\sim (2\text{mm}/2)^2 \pi \approx 3\text{ mm}^2$) which significantly improves statistics of the measurements. The visibility of iridium surface state even after the completion of graphene monolayer can be explained by weak, mostly physisorption-type interaction between graphene and iridium [51, 129]. This is also reflected on the visibility of iridium surface states at the Γ point of BZ which persist under the graphene layer (see Section 4.1). If we assume that the interaction of graphene and the Ir surface state is very weak then we expect that the graphene islands just attenuate the intensity of photoelectrons emitted from the Ir surface state proportionally to graphene coverage. In a simple three-step model of the photoemission process [102], this would be reflected in the fact that the photoelectron from the iridium surface state has to overcome a larger path and more attenuation before it is emitted from the surface.

The inelastic mean free path of the electrons with a kinetic energy of about 15 eV is of the order of 1 nm [102, 130]. When they pass through an additional graphene layer of ~ 0.34 nm in thickness, their intensity is expected to be reduced to about 70% whereas we observed reduction down to only 5%. Therefore, we must assume that a more complex mechanisms are at work. One of them could be the hybridization of iridium surface state

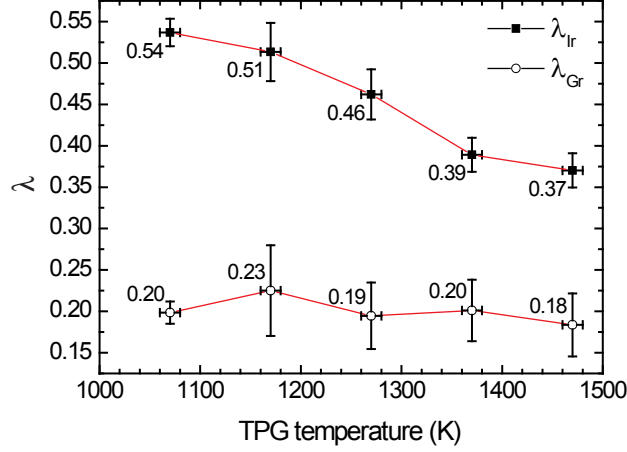


Figure 3.7: The exponents λ_{Ir} and λ_{Gr} as a function of the TPG annealing temperature. λ_{Gr} (white circles) remains in principle constant while λ_{Ir} (black squares) exhibits a decrease as the temperature increases. This can be explained by higher scattering rate of the surface state of iridium at lower annealing temperatures (see text).

and Dirac cone as proposed by Starodub et al. [50] which may affect the surface state ARPES intensity in the vicinity of the K point. Second, we consider the possibility of an upward shift of the surface state upon graphene adsorption which is supported by the observation of a small monotonous shift of several tens of meV towards the Fermi level, if the fit position of the iridium peak is not kept frozen for a growing number of TPG cycles. In that case it is clear that the ARPES intensity we monitor would apparently drop due to the Fermi level cutoff.

For all the mechanisms discussed above (attenuation, electronic interaction and upward shift), the intensity of the iridium peak could decay in accordance with the increase of graphene coverage as determined by STM and λ_{Ir} should have a value of around 0.2 instead of 0.45. In order to gain even more insight into the origin of the discrepancy between λ_{Ir} and λ_{Gr} , we have performed several consecutive TPG growth series (each consisting of 17 TPG cycles) at various annealing temperatures: 1070, 1170, 1270, 1370 and 1470 K. Each series was analyzed in the same way as described in the preceding paragraphs—by monitoring the ARPES intensity of the Dirac cone and the surface state of Ir—which resulted in growth rates λ_{Gr} and λ_{Ir} for various TPG temperatures. The corresponding data is shown in Fig. 3.7. We see that λ_{Gr} remains essentially constant, meaning that graphene growth rate is independent of the TPG annealing temperature. In other words, total graphene coverage of iridium surface (which is directly proportional to Dirac cone photoemission intensity) after a given number of TPG cycles is independent

of the temperature. In contrast to graphene growth rate, a monotonic decrease of λ_{Ir} is found as the TPG temperature is increased (cf. Fig. 3.7). We attribute this behavior to scattering of the Ir surface state at graphene edges. Such scattering was visualized in STS experiments [70]. This scattering occurs because the edges of graphene flakes are locally more strongly bond to Ir surface [68]. Scattering is therefore related to the relevant structural quantity, the graphene step-edge density, which we obtained via STM [47] as displayed in Fig. 3.2. At lower growth temperatures, step-edge density increases and hence causes higher scattering rate of the Ir surface state and suppression of its ARPES intensity. Taking into account a decrease in the intensity of the surface state proportional to the graphene covered areas with an additional decrease proportional to the measured graphene step-edge density can qualitatively lead to an overall diminution with a significantly increased λ_{Ir} as compared to λ_{Gr} and also explains the observed decrease of λ_{Ir} at lower TPG annealing temperatures.

Finally, please note there is an inconsistency in λ_{Ir} value obtained at 1470 K derived from the data shown in Fig. 3.6 (0.45) and the value noted in Fig. 3.7 (0.37). We can understand this difference as being a result of (i) slightly different sample preparation procedures, including variations in the cleaning procedures of Ir(111) which resulted in more smoother or rougher surface affecting surface state wavefunctions or (ii) error in the temperature measurement. Nevertheless, a decrease of λ_{Ir} as a function of temperature is qualitatively a realistic effect.

3.3 Carbon loss in TPG growth

We know that in one TPG cycle iridium surface is saturated with ethylene at room temperature and then annealed in order to dehydrogenate those same ethylene molecules and form graphene. If ethylene coverage upon its adsorption could be estimated and if one assumes that all C atoms left after dehydrogenation participate in graphene formation, calculation of the parameter f (and consequently λ) is trivial. We address two references where ethylene saturation coverage on Ir(111) has been determined by LEED [131] and XPS [132]. Via LEED, authors in Ref. [131] report on the formation of a poorly ordered $(\sqrt{3} \times \sqrt{3})\text{R}30^\circ$ structure. One ethylene molecule is shared among three iridium atoms and would give, after the formation of graphene, a coverage of 27.2%. In Ref. [132], the

saturation coverage of 1.1 ± 0.1 C atoms per one Ir atom is found by XPS which can be translated into a graphene coverage of 44%. These values, together with the values we obtained from STM, LEEM and ARPES in the preceding sections, are given in Table 3.1.

Obviously, the assumption that each C atom adsorbed on the iridium surface (as a part of the ethylene molecule) participates in the formation of graphene layer is wrong. The two f values obtained from Refs. [131] and [132] are both higher than our experimental f values and, even though significantly different, qualitatively point to the fact that a portion of pre-adsorbed ethylene molecules does not participate in the graphene formation. Indeed, according to thermal programmed desorption (TPD) and temperature programmed XPS (TP-XPS) results, certain amount of carbon is lost through desorption of ethylene, C_2H_4 , and its various fragments, C_xH_y during annealing [67, 131] (taking into account the negligible solubility of carbon in iridium [101]). From the values displayed in Table 3.1, we roughly estimate that 35 – 60% of C atoms are lost in this process. C 1s XPS data shown in Ref. [67] suggests this value to be 65%, although the authors there partially ascribe this to various effects related to data acquisition at high temperatures.

3.4 Average work function

Photoemission spectroscopies can be used to determine the average work function of the sample (see e.g. Ref. [30]). In the following, we shall focus on the monochromatic 2PPE measurements. For work function calculation, we use Eq. 2.3. Evidently, precise evaluation of the cutoff energies is mandatory in order to determine ΔE , the separation between the high- and low-energy cutoffs in 2PPE spectra.

The 7×TPG graphene sample was prepared which corresponds to a graphene coverage

Table 3.1: Graphene growth parameters obtained from the experiments described in the preceding sections (LEEM, STM, ARPES) and estimated values based on the data from the literature (LEED, XPS). λ is the parameter from graphene growth equation $\theta_{Gr}(N) = 1 - e^{-\lambda N}$, f is the fraction of bare iridium surface covered with graphene after each TPG step.

method	λ	f (%)
LEEM	0.162 ± 0.004	15.0
STM	0.21 ± 0.02	18.9
ARPES	0.196 ± 0.007	17.8
LEED [131]	—	27.2
XPS [132]	—	44.0

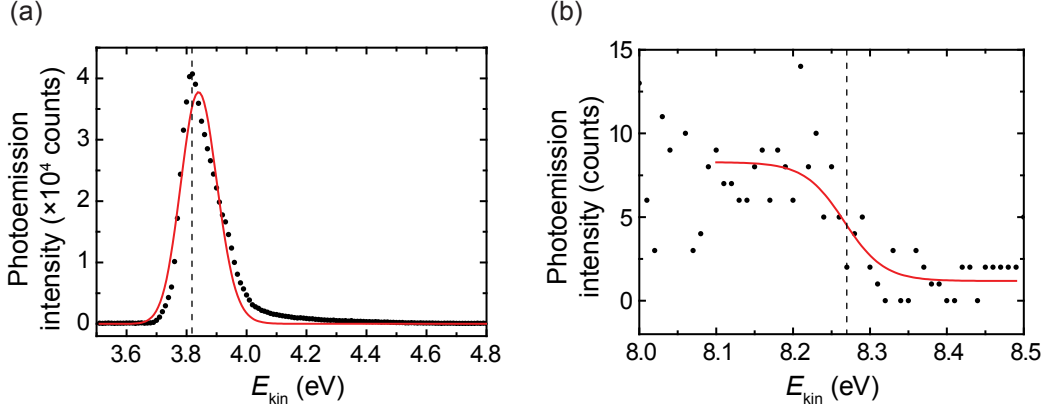


Figure 3.8: The 2PPE EDC spectra of a 0.75 ML Gr/Ir(111) sample. **(a)** Normal emission low-energy cutoff peak (black dots) originating from one-photon photoemission of the electrons excited thermally above the Fermi level. Red curve is a fit by Eq. 3.2. Dashed line indicates the position of E_L at 3.818 eV. **(b)** Off-normal emission high-energy cutoff (black dots) originating from two-photon photoemission of the electrons from the Fermi level. Red curve is a fit by Eq. 3.3. Dashed line marks the vacuum level at 8.27 eV. The sample was biased at -4 V. $\hbar\omega = 4.68$ eV, $T_S = 300$ K.

of 0.75 ML (see Section 3.2). Fig. 3.8(a) displays a typical low-energy cutoff obtained in our 2PPE experiments. The measurements were performed with a bias of -4 V applied to the sample in order to avoid the effects of stray fields. The negative sample bias results in the shift of the peak to higher kinetic energies, away from $E_{\text{kin}} = 0$ eV. As can be seen from the data (black dots), the peak is asymmetric and a proper fitting function has to be used in order to exactly determine the position of the low-energy cutoff. A good description of the data can be achieved by using a convolution of the tail of the Fermi-Dirac distribution multiplied by a step function (representing intrinsic line-shape) and a Gaussian function (representing instrumental function) [133]. The resulting convolution i.e. photoemission intensity has the form

$$I = \frac{A}{2} \exp \left[\frac{\beta}{2} (2E_L - 2E + \delta E^2 \beta) \right] \left[1 - \operatorname{erf} \left(\frac{E_L - E + \delta E^2 \beta}{\sqrt{2} \delta E} \right) \right] \quad (3.2)$$

where A is the height of the step function (and is proportional to the peak height), E_L is the position of the low-energy cutoff, δE is the width of the Gaussian function (and equals to electron analyzer resolution) and $\beta = 1/kT$. The resulting fit to the data is shown by red curve in Fig. 3.8(a). E_L is determined to be (3.818 ± 0.001) eV. Also, fitting procedure yields an energy resolution of the analyzer which is found to be $\delta E = (56 \pm 1)$ meV. In this fit, β was not a free parameter as the sample temperature was 300 K.

We now turn to high-energy cutoff of the 2PPE spectra. The corresponding data

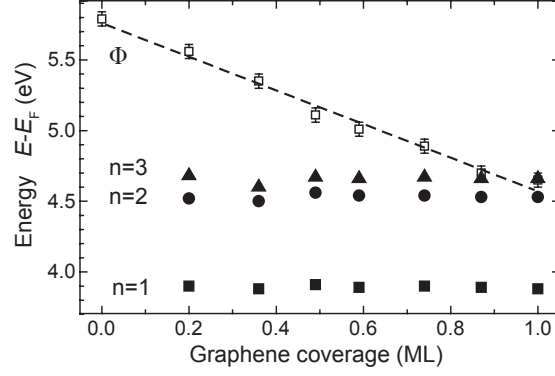


Figure 3.9: Measured work function (open symbols) of Gr/Ir(111) as a function of graphene coverage. A linear decrease is fitted by a dashed line. Solid symbols represent binding energies of image-potential states of the system (see Section 4.2 for more information). Adopted from Ref. [134].

points are shown in Fig. 3.8(b). It should be noted that EDC recorded as far as possible from normal emission should be taken for the determination of the high-energy cutoff because of possible interference of the electronic states with the cutoff (as e.g. image-potential states are found close to the vacuum level, see Section 4.2 for details). For fitting purposes, a convolution of the Fermi-Dirac distribution and a Gaussian function should be taken to determine the position of the cutoff i.e. vacuum level E_V . But the convolution is necessary only at very low sample temperatures and in our case, at 300 K, is not needed. Hence, we take just the Fermi-Dirac distribution with an arbitrary amplitude A and offset C for fitting

$$I = \frac{A}{\exp[\beta(E - E_V)] + 1} + C. \quad (3.3)$$

The fit is indicated by the red curve in Fig. 3.8(b) and the vacuum level position is $E_V = (8.27 \pm 0.01)$ eV. Now we can calculate the value of the work function (knowing that $\hbar\omega = 4.86$ eV) which amounts to $\Phi = (4.91 \pm 0.01)$ eV.

Much more extended analysis of the average work function for various graphene coverages is found Ref. [134]. One of the main conclusions is that the work function decreases linearly with graphene coverage (see Fig. 3.9). It is found that the work function of bare iridium is (5.79 ± 0.10) eV, which drops down to (4.65 ± 0.10) eV for $\theta_{\text{Gr}} = 1$ ML. Here calculated value of 4.91 eV for $\theta_{\text{Gr}} = 0.75$ ML fits very well to this decrease. Generally, the linear decrease of the average work function has been observed for other systems and has its origin in the averaging property of the photoemission process over the areas of

different work functions [135]. The work function of 1 ML sample is close to the value of 4.48 eV of free-standing graphene [136] which is a confirmation of weak interaction between graphene and iridium. As it will be discussed in Chapter 4, local work function variation on the sample is responsible for the localization of electrons on graphene islands.

3.5 Graphene wrinkles

3.5.1 Wrinkles network

An typical structural feature of epitaxial graphene are wrinkles caused by compression of the graphene governed by its substrate. Since wrinkles are an integral part of graphene layer and various samples originating from it, their detailed analysis is a necessity in order to fully understand a range of graphene properties. Fig. 3.10(a) shows LEEM image of a characteristic R0 area of Gr/Ir(111) grown by TPG and CVD procedures at 1270 and 1120 K, respectively. Graphene wrinkles are easily identified as thick dark lines extending $\sim 1 \mu\text{m}$ in length and forming a complex network. At first sight, it seems that wrinkles extend mainly in three directions rotated by an angle of $\sim 60^\circ$. As a consequence of that, wrinkles crossings most often contain three wrinkles separated by 120° . These speculations are confirmed after subtracting background from Fig. 3.10(a) and performing Fourier transformation, when a clear 6-fold symmetrical pattern is revealed as shown in Fig. 3.10(b). Because the pattern in the inverse space contains stripes and not spots, we conclude that the separation between two parallel wrinkles and their apparent thickness have relatively broad distribution, but directional preference is nevertheless obvious. In order to make our analysis more quantitative, we calculate radial sums of the Fourier transform from panel (b) and display the results in a polar plot in panel (c). Again, 6-fold symmetry is evident. After plotting the same data in the $x-y$ plot and fitting the six peaks with Gaussian curves (not shown), it is easy to calculate the directions of extension of wrinkles. They are $(53.5 \pm 0.3)^\circ$, $(112.5 \pm 0.3)^\circ$ and $(172.6 \pm 0.6)^\circ$ (with respect to the horizontal in the counterclockwise direction). The difference between those directions fits well to 60° , which is what we inferred from LEEM image in Fig. 3.10(a). This also suggests that the wrinkles network can be regarded as composed mostly of more-or-less distorted hexagons.

Next, we try to understand what is the defining factor of the three observed direc-

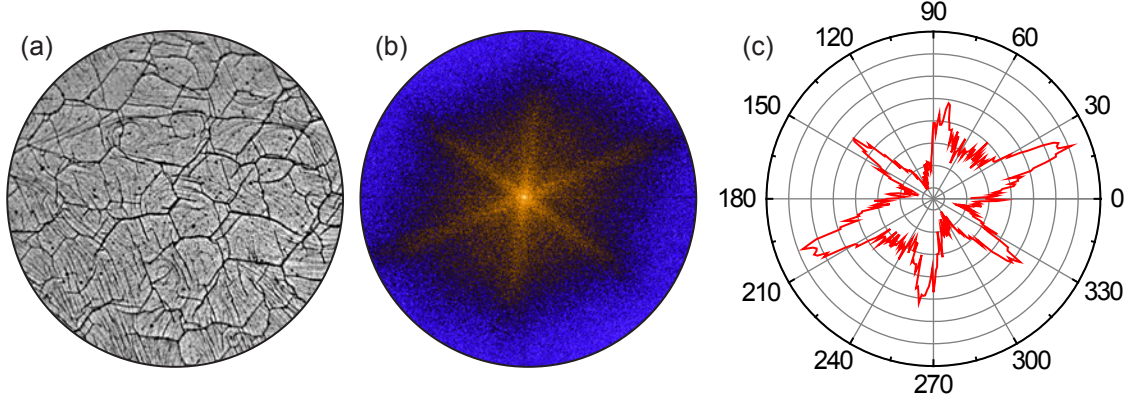


Figure 3.10: (a) LEEM image of a full graphene layer on Ir(111). Thick dark lines extending over the entire sample surface are graphene wrinkles. $\text{FOV} = 9.3 \mu\text{m}$, $E = 16 \text{ eV}$, $T_s = 369 \text{ K}$. (b) Fourier transform of (a). 6-fold symmetric pattern is visible corresponding to three dominant directions of wrinkle extension (c) Polar plot of radial sums extracted from (b) exhibiting 6-fold symmetry. The radial distance of the red curve is in arbitrary units.

tions. Knowing that the wrinkling process is closely related to the substrate structure, we determined the exact orientation of atom rows on iridium surface which is schematically illustrated in the circular inset in Fig. 3.11. Yellow dashed lines mark three calculated wrinkle-extending directions and a perfect coincidence between the dense-packed atomic rows of iridium and graphene wrinkles direction is found. In other words, during cooldown from high temperatures, iridium shrinkage can be described as reduction of separation between adjacent atomic planes (in the bulk) i.e. rows (on the surface). This shrinkage induces stress in graphene which is then relaxed through the formation of wrinkles in the direction parallel to atomic rows of iridium. From this we also infer that the wrinkles are formed parallel to the zig-zag direction of graphene. This relation was proposed earlier for graphene flakes on iridium [58].

Up to now, we only discussed wrinkles on R0 graphene. The symmetry and structure of R0-wrinkles does not have to be the same on other rotational variants of graphene. In order to investigate this, in Fig. 3.12(a) we show a LEEM image of a boundary between two rotational domains of graphene, exhibiting different reflectivity, which are identified via μ -LEED as R0 and R30. A network of wrinkles is present on both domains. Corresponding Fourier transform are also shown in Fig. 3.12(a). Whereas the symmetry of R0 transform is 6-fold, similar as in Fig. 3.10(b), this is not the case for R30 graphene where only two mutually perpendicular directions with large angular spread are found. This indicates that R30 graphene sheet is effectively subjected to stress in two directions

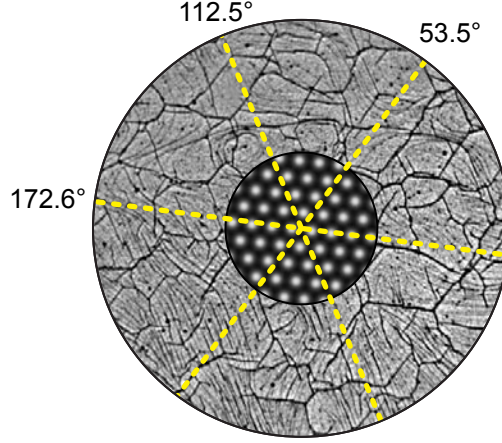


Figure 3.11: LEEM image [the same as in Fig. 3.10(a)] with superimposed circular inset depicting the orientation of atomic rows on the iridium surface and yellow dashed lines indicating dominant directions of graphene wrinkles extension.

and not in three as in the case of R0 graphene. It should be noted that iridium steps also contribute to the Fourier transform to some extent, but the absence of 6-fold symmetry is independent of this contribution. Knowing that two distinct directions are enough for stress relaxation in two dimensions, observation of three (two) directions in R0 (R30) graphene calls for an explanation. We propose that the origin of this is in difference of binding of graphene to Ir. From previous studies [50] it was argued that R30 graphene is more weakly bound to Ir as compared to R0 graphene. On one hand this means that R0 graphene is compelled to follow contraction of the substrate in each of the three equivalent directions defined by the (111) surface of FCC lattice. On the other hand, R30 graphene, being more weakly bound to Ir, does not have to keep track of the underlying Ir and is free to wrinkle in two approximately perpendicular directions. However, the absolute orientation of those two directions is to some extent defined by the substrate. It is visible from Fig. 3.12(a) that one part of the R30 wrinkles is parallel to Ir steps while the other part is perpendicular to them. Similar observations were made in the case of graphene on Pt(111) [9], a system in which graphene is more weakly bound to the substrate as compared to Gr/Ir(111). Careful inspection of the R0 Fourier transforms of Fig. 3.10(b) and 3.12(a) reveals miss-orientation of the two patterns by a few degrees. We explain this by the presence of R30-wrinkles in the vicinity of R0-wrinkles in Fig. 3.12(a) and their intermixing.

In the R30 area particularly long wrinkles extending $\sim 10 \mu\text{m}$ in length can be found, which we never observed on R0 graphene. Several wrinkles of that kind are marked by

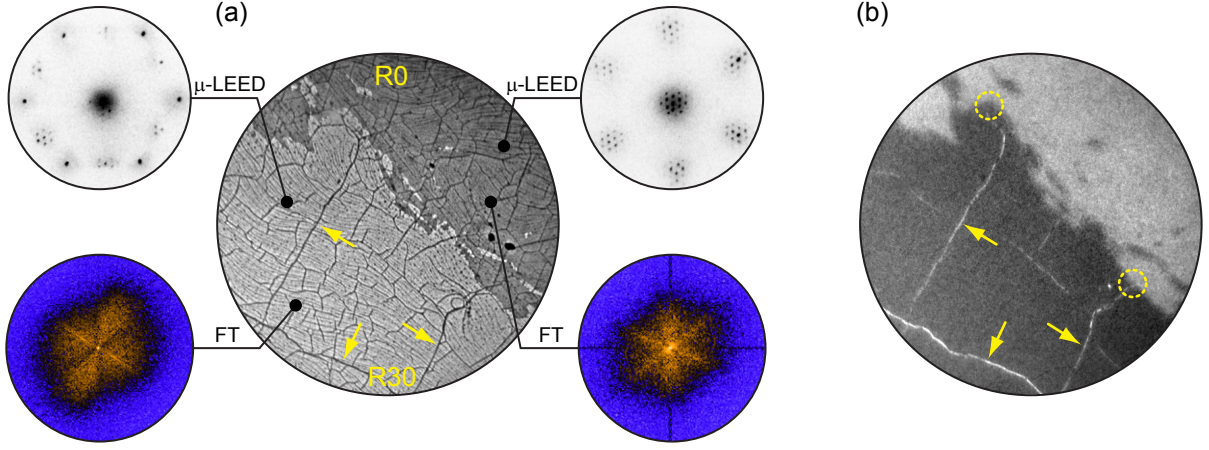


Figure 3.12: (a) LEEM image of R0/R30 graphene boundary (center) with the corresponding μ -LEED patterns and Fourier transforms (left and right). LEEM: FOV = 14 μm , $E = 3.8$ eV, $T_S = 371$ K. LEED: $E = 73$ eV. (b) The same area as in (a) recorded at higher electron energy ($E = 7.2$ eV). Wrinkles marked by yellow arrows [also marked in (a)] exhibit unusually high reflectivity. Such special property is found only in R30 graphene areas.

wrinkles marked by yellow arrows in Fig. 3.12(a). They also appear to have unusually large width in LEEM which, to some extent, reflects their true larger width because of increased incoherent electron scattering (and hence dark contrast). In Fig. 3.12(b) we show the same area as in (a) but recorded at different electron energy. Clearly, the wrinkles marked by arrows in (a) are exhibiting bright contrast in (b). Additionally, once those wrinkles reach the R0-R30 graphene boundary [cf. dashed circles in Fig. 3.12(b)], their bright contrast is diminished. It is safe to say that these unusual wrinkles are reserved only for the R30 graphene. The exact origin of their peculiar contrast is still not understood. One explanation could be that those wrinkles are for some reason decorated with additional atoms, presumably Ir atoms, which could influence their reflectivity. Additional microscopic measurement (LEEM, STM or AFM) are needed for more reliable explanation.

3.5.2 Localized stress relaxation and wrinkle pinning

In order to gain more locally-specific information on wrinkling process, after the formation of 1 ML graphene via TPG + CVD procedure (at 1470 and 1120 K, respectively) and cooling the sample to room temperature, we re-heated the sample up to 920 K and cooled it back down while simultaneously recording LEEM data. This enabled the observation of disappearance and reappearance of wrinkles, similarly as discussed in Ref. [58]. In Fig. 3.13 we show two areas on the sample recorded right before (frame 1) and after (frame

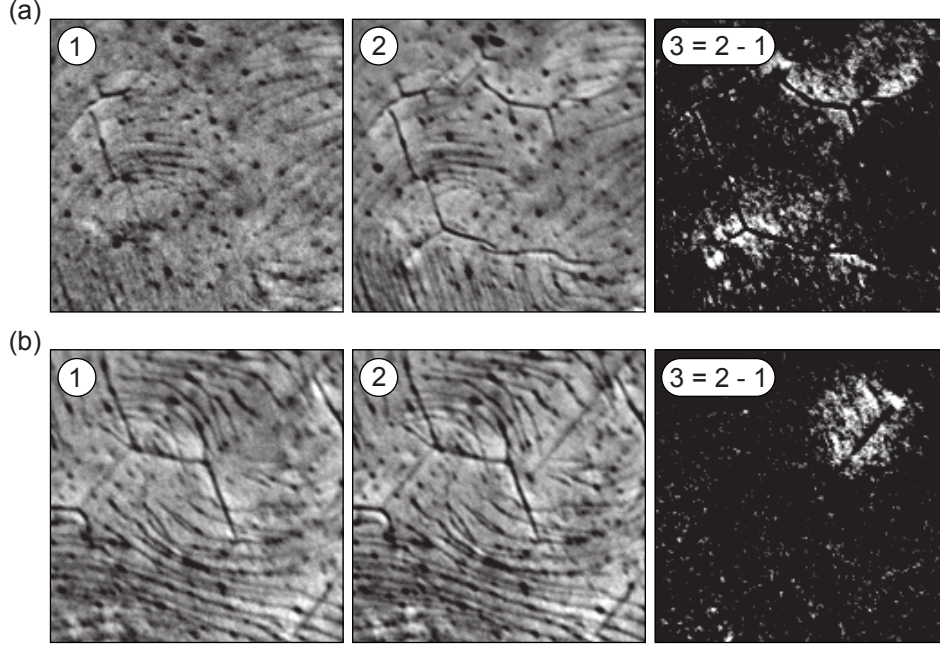


Figure 3.13: LEEM micrographs, $(3 \times 3) \mu\text{m}^2$ in size, showing two different areas (a) and (b) of Gr/Ir(111) right before (frames 1) and after (frames 2) wrinkle popping. Frames 3 displays the image difference $2 - 1$, highlighting the contrast changes in the vicinity of emerging wrinkles. (a) is recorded at 623 K, (b) at 543 K. $E = 3.8$ eV.

2) the appearance of several wrinkles during cooldown. Images in (a) were recorded at 623 K while in (b) they were recorded at 543 K. From comparison of frames 1 and 2, we deduce that the reflectivity of graphene surrounding the appearing wrinkles increases by 2.9% once the wrinkle is formed. This is even more obvious in frame 3, where we show the difference of frames 2 and 1. This observations is discussed in Ref. [58] to be a result of a change in interference conditions of incoming and reflected electron waves. However, we believe a more plausible explanation for this observation is offered by the following argumentation. LEEM images are recorded in bright field mode at 3.8 eV electron energy and at such low energies only (0,0) and a fraction of higher order moiré spots contribute to image formation [cf. Fig. 3.14(a)]. Furthermore, at the moment of wrinkle formation a_{Gr} increases and $k_{\text{moiré}}$ decreases (cf. Eq. 1.3 and 1.4). Because of that, moiré diffraction spots shift closer to (0,0) spot by $\sim 3\%$ [45] [cf. Fig. 3.14(b)]. Consequently, a decrease of $k_{\text{moiré}}$ can result in an increase of fraction of moiré spots intensity contributing to LEEM images. In other words, areas in LEEM images which become brighter after wrinkle formation are areas where $k_{\text{moiré}}$ is decreased i.e. a_{Gr} is increased. In this way, graphene lattice relaxation can be directly observed in real space. This also indicates that stress imposed on graphene is relaxed only locally in the vicinity

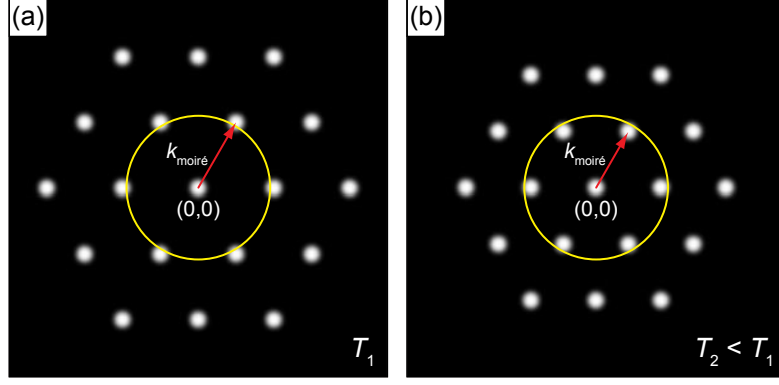


Figure 3.14: An illustration of the proposed origin of LEEM reflectivity changes upon wrinkle formation. White spots represent $(0,0)$ and first and second order moiré diffraction spots. **(a)** Before wrinkling (at temperature T_1), only $(0,0)$ spot and a small fraction of first order moiré spots located inside the yellow circle contribute to image formation. **(b)** After wrinkling (at temperature $T_2 < T_1$), $k_{\text{moiré}}$ decreases (cf. red arrows) and a fraction of the first order moiré spots contributing to the image formation increases (here exaggerated for clarity). As a result, the reflectivity in LEEM image is increased.

of the wrinkles and that graphene areas situated further from wrinkles remain stressed.

As described in the preceding paragraph, both disappearance and reappearance of the wrinkles were monitored in LEEM during re-heating. This enabled us also to see whether wrinkles form at the same sites, pinned to graphene or substrate features, or they form randomly over the graphene surface. Fig. 3.15 shows two LEEM images of the same area on the sample. Image (a) was recorded at 520 K during heating and image (b) at 520 K during cooling. In between the sample temperature reached a maximum of 920 K when all wrinkles were flattened out. Comparison of the two images directly tells us that some of the wrinkles reappeared on the same location (cf. red arrows in Fig. 3.15) but many other appeared on the positions which were wrinkle-free before re-heating (some of them marked by yellow arrows in Fig. 3.15). Surely, additional wrinkles appear when the sample is cooled down to room temperature, but due to thermal drift the exact information on this is not available to us. Also, because of the histeretic behavior of wrinkles [45] it is not expected that Fig. 3.15(a) and (b) look the same, but this does not underrate our observation that new wrinkles locations do not coincide with the old ones. Therefore, we conclude that different structural features of graphene or iridium can anchor the wrinkles and serve as nucleation sites for their formation with a note that many wrinkles form randomly i.e. not in the same locations as previously existing ones. This is in partial agreement with the previous findings on graphene flakes [58] where the authors claim that majority of wrinkles nucleate at defects, more precisely at heptagon-pentagon

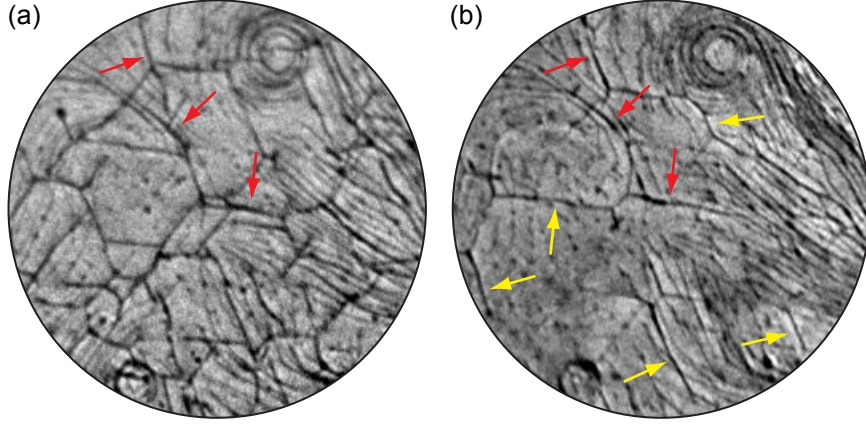


Figure 3.15: LEEM images of the same surface area illustrating wrinkle pinning. Several graphene wrinkles are visible (a) at 520 K during heating and (b) at 520 K during cooling. Some of the wrinkles reappeared at the same positions (red arrows) while some appeared at positions which were wrinkle-free before re-heating (yellow arrows). FOV = 7.2 μm , $E = 3.8$ eV.

pairs.

3.5.3 Voronoi approximation

On the basis of collected LEEM data, we hypothesize that the network of graphene wrinkles can to a good extent be approximated by Voronoi diagram (VD) i.e. a network obtained by Voronoi tessellation of 2D space [137]. Its construction is quite simple: for a given set of points (called centroids), the space is divided in cells (called Voronoi cells) associated to each centroid in a way that each cell contains points that are closer to a given centroid than to any other. Such construction is often exploited in solid state physics for the construction of Wigner-Seitz cells in real space and Brillouin zones in reciprocal space, where in both cases the centroids are defined by crystal lattice. In order to illustrate our hypothesis, in Fig. 3.16 we show an overlap of a recorded LEEM images and VD (yellow dashed lines) generated from centroids marked by red dots. Each centroid was moved by hand individually until satisfactory agreement between wrinkles network and VD was obtained. Clearly, majority of wrinkles coincide with yellow lines but there are some exceptions. For example, VD predicts existence of some wrinkles which are actually not there (cf. arrows 1 and 2) or absence of wrinkles which were found at certain location (cf. arrows 3 and 4). We believe that this approximation is valid and would get even better if various defects on the iridium surface as well as iridium steps were suppressed to a minimum. One should bare in mind that wrinkles of smaller dimensions are hard to

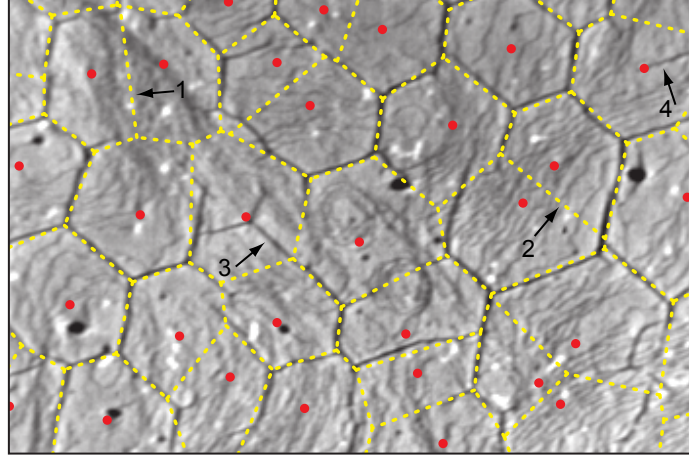


Figure 3.16: Graphene wrinkles network superimposed by a Voronoi diagram (yellow dashed lined) generated by red centroids. A good agreement between wrinkles network and Voronoi cells is found in most cases. Black arrows indicate several deviations. Image size: $(6.5 \times 4.3) \mu\text{m}^2$, $E = 1.9 \text{ eV}$, $T_S = 364 \text{ K}$.

resolve in LEEM images and that wrinkles in general can be mistaken for iridium steps and vice versa. As an alternative, power-Voronoi or area-Voronoi diagrams [137] can be used in this approximation but they would yield only minor improvements at the expense of more complicated analysis.

In the following, we deal with the spatial distribution of the centroids. It might seem that their distribution is random, but in that case the wrinkles directions would not exhibit preference in their direction and the Fourier transforms in Fig. 3.10(b) and Fig. 3.12(a) would be isotropic. As we have shown in the beginning of this section and as can be inferred from Fig. 3.16, a typical Voronoi cell is in principle similar to a hexagon. In other words, our wrinkles network as well as VD can be regarded as a network of distorted hexagons yielding a quasi-honeycomb structure as a whole. In Appendix C, we use this fact and try to simulate wrinkles network, beginning with regular triangular lattice as a set of centroids for VD generation. Then, a specific amount of disorder is introduced in that lattice by so-called thinning or/and displaced lattice processes (see Appendix C for details). By comparing the corresponding Fourier transforms, it can be inferred that indeed the simulated networks resemble to the real one [cf. Fig. C.1(e) and (f)].

A VD generated by a random distribution of centroids, then called Poisson-Voronoi diagram, have been studied extensively (see Ref. [137, 138] and references therein). Expected values of various parameters (cell area, cell perimeter, number of edges etc.) of such diagrams have been calculated and simulated. These parameters values are not ex-

Table 3.2: Relations between various parameters of the Poisson-Voronoi diagram and their calculated expected values for experimentally determined $n_v = 1.7 \mu\text{m}^{-2}$.

parameter	symbol	relation to n_v	expected value
density of vertices	n_v	n_v	$(1.7 \mu\text{m}^{-2})$
density of centroids	n_c	$\frac{n_v}{2}$	$0.9 \mu\text{m}^{-2}$
wrinkle length per unit area	l	$2\sqrt{\frac{n_v}{2}}$	$1.9 \mu\text{m}^{-1}$
area of a cell	A	$\frac{2}{n_v}$	$1.2 \mu\text{m}^2$
perimeter of a cell	P	$4\sqrt{\frac{2}{n_v}}$	$4.3 \mu\text{m}$
length of a single wrinkle	L	$\frac{2}{3}\sqrt{\frac{2}{n_v}}$	$0.7 \mu\text{m}$

pected to vary too much for centroid distributions other than random [137], so they can be adopted for characterization of quasi-honeycomb VD network found for graphene wrinkles. First of all, it is worth noting that the expected value of an angle at a typical vertex (a point where three wrinkles meet) is 120° , which agrees with the Fourier transform data presented in Fig. 3.10(b). One of the easiest quantities to obtain from LEEM data is the number of wrinkle vertices (wrinkle intersections) per unit area, n_v . Once this number is known, we can calculate expected values for several parameters following the theory of Poisson-Voronoi tessellation [137]. n_v for the LEEM image in Fig. 3.16 amounts to $1.7 \mu\text{m}^{-2}$. Other calculated parameters are given in Table 3.2. If our wrinkles network is approximated by VD, we can easily estimate various parameters which are relevant for their general description. The values from the table are not universal and differ depending on the preparation parameters of graphene, especially the growth temperature.

3.5.4 Internal structure

Up to now we were only dealing with the macroscopic concept of the wrinkles network, without considering what is the internal structure of individual wrinkles and the structure of wrinkles intersections. In order to investigate this, we performed STM measurements at room temperature. Fig. 3.17 displays several STM images of various wrinkle segments. In panel (a), we show a beginning of an individual wrinkle which appears to consist of several smaller folds. These folds impinge into graphene sheet with their ends protruding in one direction while merging into a bigger, complex structure in the opposite direction. A straight segment of a wrinkle is displayed in Fig. 3.17(b). Again, internal folded structure is evident. We can conclude that these wrinkles cannot be described by a simple

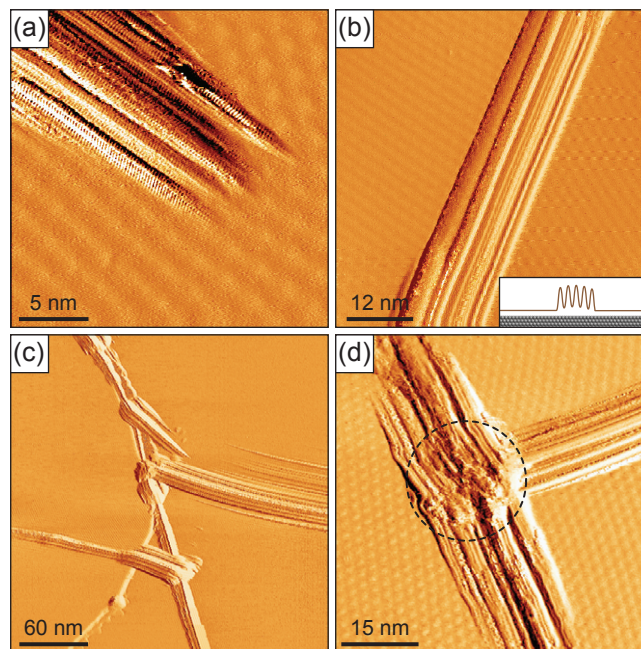


Figure 3.17: Sections of graphene wrinkles imaged by STM. (a) An end merging with the flat part of the graphene sheet ($U_t = 850$ mV, $I_t = 2.51$ nA), (b) straight segment ($U_t = 690$ mV, $I_t = 2.19$ nA) and (c), (d) crossing sites of several wrinkles ($U_t = 780$ mV, $I_t = 750$ pA and $U_t = 150$ mV, $I_t = 240$ pA). In all panels, multi-folded structure of wrinkles can be resolved, as sketched in the inset of (b). The crossing area highlighted by the dotted circle in (d) appears as highly crumpled structure.

semicircular profile but rather a more complex, multi-folded structure as schematically sketched in the inset of Fig. 3.17(b). This kind of structure can be a result of an interplay between the van der Waals interaction acting between different parts of wrinkles and the substrate and elastic energy of a constrained graphene sheet. In order to obtain more information on this structure and its formation, theoretical modeling is necessary.

In general, widths (10-50 nm), heights (1-5 nm) and the number of folds of different wrinkles vary which certainly also depends on the exact preparation parameters of graphene. Individual wrinkles can slightly change their direction and sometimes also width or height [cf. Fig. 3.17(c)]. In contrast to the homogeneous parts, the wrinkle crossing shown in Fig. 3.17(d) depict a highly inhomogeneous structure. Although it is not possible to resolve details in such crumpled regions, it is very probable that they contain cracks, holes and other kind of defective structures. As it will be shown in Chapter 5, these defects are crucial for the intercalation of graphene. Finally, we note that great care has to be taken during STM imaging of wrinkles (e.g. of V_t , I_t and scanning speed) due to their large lateral and vertical dimensions.

CHAPTER 4

Electronic structure at the Brillouin zone center

When it comes to graphene and its electronic structure, majority of literature is dealing with the Dirac cone located at the K point of the Brillouin zone. This is well justified since the Dirac cone bands cross the Fermi level and by that define a large number of graphene's physical properties. Furthermore, occupied electronic structure below the Fermi level is well documented, most often via ARPES, but relatively little is known about the unoccupied electronic structure of graphene above the Fermi level.. There, Rydberg-like IPS are found which are pinned to the vacuum level. A double series of IPSs is predicted to exist on freestanding graphene as a consequence of its 2D character [31]. The overall importance of IPSs is indisputable (see Section 1.1) and hence their thorough investigation is desired.

Consequently, in this chapter we present characterization of the occupied and unoccupied electronic band structure of Gr/Ir(111). As we will see, iridium surface states at the Γ point will be important for the mapping of the unoccupied structure, so we will begin with their description as inferred from ARPES measurements. Next, we focus on 2PPE results of IPSs of Gr/Ir(111) and provide their basic parameters: effective masses and binding energies. We also discuss the effect of resonant transitions from the occupied to unoccupied states. Finally, we address the confinement of IPS electrons on graphene islands.

4.1 Rashba-split surface states of iridium

Surface states can be regarded as electrons localized mainly within the surface of a crystal due to the presence of the crystal band gap on one side and the vacuum barrier on the

other. In other words, surface states originate at energy gaps of the bulk-band structure projected on the surface. In the simplest cases, electrons can move freely in directions parallel to the surface which results in parabolic dispersion of the state. One typical example of such state is the surface state of Cu(111) which exhibits free-electron-like dispersion [139]. Moreover, due to the presence of the surface, the inversion symmetry is broken which results in the lifting of the spin degeneracy and consequently splitting of the surface states [140, 141]. This kind of splitting is called Rashba splitting and it is most pronounced in heavy-atom systems where spin-orbit coupling is strong. A famous example of Rashba splitting is the parabolic surface state of Au(111) [139, 142]. If the split state is parabolic, the energy bands can be described by

$$E_{\pm}(\mathbf{k}_{\parallel}) = \frac{\hbar^2 \mathbf{k}_{\parallel}^2}{2m^*} \pm \alpha_R |\mathbf{k}_{\parallel}| + E_0 \quad (4.1)$$

where m^* is the effective mass of the state, α_R is the splitting parameter and E_0 is the binding energy of the state.

Recently, it has been shown that on (111) surface of iridium Rashba-split surface state exist at the Γ point [127, 134]. What is more interesting, that state persist even when the iridium is covered with graphene layer. In the first frame of Fig. 4.1(a) we show an ARPES maps recorded at the Γ point of Gr/Ir(111) sample. Immediately, two downward-dispersing parabolic features can be noticed. They are identified as the surface state of iridium. By performing EDC and MDC analysis of the spectrum up to 400 meV below the Fermi level (at higher binding energies the bands start to deviate from parabolic dispersion, cf. Fig. 4.3) and fitting the resulting data points to Eq. 4.1, we obtained their effective mass $m^* = -0.163 m_e$ and the splitting parameter $\alpha_R = 1.89 \text{ eV \AA}$. The splitting parameter is large and exceeds e.g. the splitting found on Au(111) by an order of magnitude, $\alpha_{R,Au} = 0.33 \text{ eV \AA}$ [142]. The k -space splitting between the parabolas is found to be $\Delta k = 0.081 \text{ \AA}^{-1}$ and the apex of the parabolas is located at 0.191 eV below the Fermi level. All obtained values agree well with the literature [127, 134]. The second and the third frame of Fig. 4.1(a) show ARPES spectra recorded at the noted k_y values, slightly away from the Γ point. The surface state now looks like two distinct parabolas with their apexes located one above the other. In order to clarify this kind of electronic structure, Fig. 4.1(b) shows a 3D model of the Rashba-split state plotted according to the calculated values of m^* , α_R and binding energy. Only for the plane $k_y = 0 \text{ \AA}^{-1}$, the true

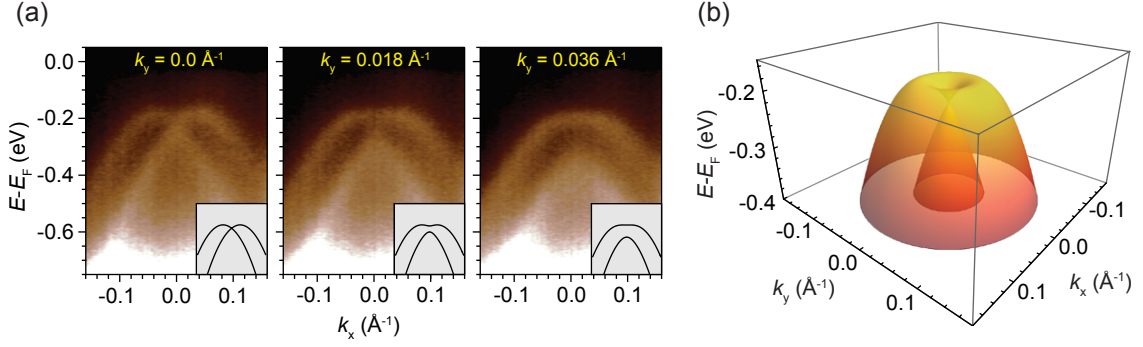


Figure 4.1: (a) ARPES spectra of the Rashba-split surface state of Gr/Ir(111) recorded at three different k_y values in the vicinity of the Γ point. At higher k_y values, the split state appears as two parabolas shifted in energy rather than in momentum. Zg-ARPES, $\perp \Gamma K$, $\hbar\omega = 21.2 \text{ eV}$, mixed polarization, $T_S = 250 \text{ K}$. (b) A 3D model of the Rashba-split state. Slices of the model at the corresponding k_y values are shown in the insets of (a).

character of the bands is revealed in the form of the two parabolas separated in k space by Δk . Slicing the 3D structure at $k_y \neq 0 \text{ \AA}^{-1}$ yields two parabolic-like bands located one above the other. Slices of the 3D band structure from panel (b) at the corresponding wavevectors are shown in the insets of frames in panel (a). Therefore, even a small sample misalignment i.e. deviation from the normal photoemission can result in data which does not reveal, at least not at first sight, the true Rashba character of the surface state. This was the case in Ref. [49] where also a more global overview of the Ir(111) band structure can be found.

The origin of the iridium surface state is well understood from the theoretical calculations. They show that the projected bulk-band electronic structure of Ir(111) exhibits a band gap of the sp character [134] which enables the existence of the surface state. Moreover, the state possesses p_z -like character only in the close vicinity of the Γ point. Away from the Γ point, it becomes $d_{x,z}$ -like and can be viewed as surface resonance due to the intermixing with the bulk states [143]. This can also be inferred from our experimental data: only close to the Γ point, the state exhibit parabolic shape characteristic for the s and p surface states while at higher wavevector values ($\gtrsim 0.13 \text{ \AA}^{-1}$) the dispersion strongly deviates from the parabolic one (cf. Fig. 4.1 and 4.3). Finally, we note that the surface state shifts by 150 meV to lower binding energies upon graphene formation [143]. Similar effect is found for the iridium surface state at the K point (see Section 3.2) which is ascribed to p -doping of graphene by iridium electrons.

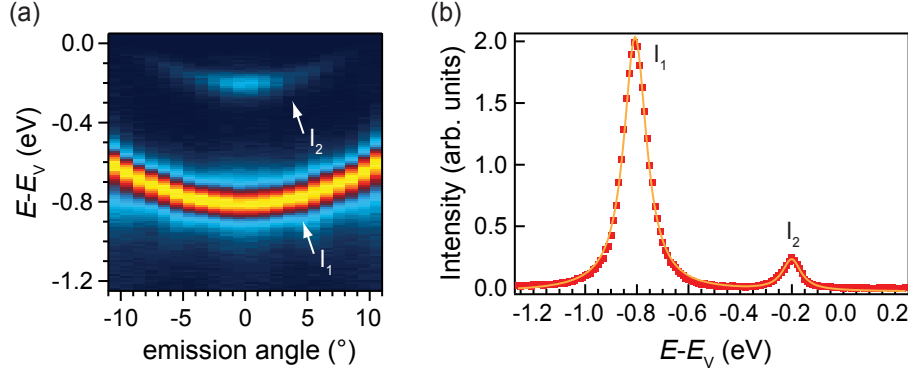


Figure 4.2: (a) Monochromatic 2PPE spectra of 1 ML Gr/Ir(111). Two parabolic image-potential states I_1 and I_2 are visible. $\hbar\omega = 4.68$ eV, $T_s = 300$ K. (b) EDC profile (red squares) of the normal emission 2PPE spectrum shown in (a) and the corresponding Lorentzian fit (orange line). Two peaks correspond to the first two image-potential states.

4.2 Image-potential states of graphene on Ir(111)

Fig. 4.2(a) shows monochromatic 2PPE intensity of 1 ML graphene sample measured with 4.68 eV (265 nm) photons in the range of angles $\pm 11^\circ$ off the normal emission. We note that due to the instability of the laser output power over time, the spectra in Fig. 4.2(a) is normalized to the maximum value of each EDC scan. Two electronic states marked as I_1 and I_2 are clearly resolved. They exhibit parabolic dispersion and are pinned to the vacuum level, which is nicely visible in the form of vanishing 2PPE intensity of the I_2 state at the vacuum level. In order to obtain the binding energies of the states, in Fig. 4.2(b) we plotted the normal emission EDC scan (red squares) and performed the fitting procedure by two Lorentzian curve (orange line). The binding energies of the states with respect to the vacuum level are $E_{B1} = (-0.8066 \pm 0.0003)$ eV and $E_{B2} = (-0.200 \pm 0.002)$ eV. These values are in fair agreement with our published data [134], especially bearing in mind that the moderate energy resolution of the analyzer (56 meV) can lead to broadening and shifting of the 2PPE spectra [144]. Due to the lack of exact angular calibration, the spectra from Fig. 4.2(a) are not converted to a momentum space. We will refer to our bichromatic 2PPE data presented in Ref. [134] for an additional information on the unoccupied band structure of Gr/Ir(111). There, an additional electronic state I_3 (not visible in Fig. 4.2) is observed between the I_2 state and the vacuum level. As we will see below, this is a result of choice of particular photon energy used for electron pumping from the occupied states. The effective masses of all three states are found to be $0.9 m_e$ and their binding energies are 0.83 eV, 0.19 eV and 0.09 eV with respect to the vacuum

level. These binding energies fit well to a Rydberg-like series of IPSs with a nonvanishing quantum defect [28, 134]. Accordingly, these states are identified as IPSs of graphene on Ir(111). It is worth noting that the effective masses of IPSs of Gr/Ir(111) system are almost equal to $1.0 m_e$ found for Gr on SiC(0001) [145].

Our data presented in Fig. 4.2 and in Ref. [134] does not show any indication of a double series of IPSs as predicted for freestanding graphene [31]. This is also true for graphene on other metal surfaces [146]. In contrast, a double IPS series has been observed via STS and 2PPE for graphene on SiC [145, 147]. We therefore conclude that the presence of a metal substrate effectively breaks the mirror symmetry of a graphene layer, which is not the case for SiC.

Next, we try to identify which occupied electronic states served as pump states in the 2PPE process [cf. Fig. 2.2(b)]. A good candidates for this role are states located at the Γ point, in the vicinity of the Fermi level. In the case of Gr/Ir(111), spin-split surface state of iridium is found there as was shown in Fig. 4.1(a). We show that state again in Fig. 4.3(a) recorded at a synchrotron facility. A deviation from the parabolic dispersion can be seen at the binding energies higher than ~ 0.5 eV. It should also be noted that at photon energy of $\hbar\omega = 55$ eV used for acquiring data in Fig. 4.3(a), the bulk band of iridium located at 1 eV below E_F is suppressed, unlike in Fig. 4.1(a) ($\hbar\omega = 21.2$ eV) where that band partially masks the surface states of iridium from below. We performed EDC analysis of the state from Fig. 4.3(a) and the resulting data points are shown in Fig. 4.3(b) as bands R_1 and R_2 . In that panel, we also plot the dispersions of the first three image states I_1 , I_2 and I_3 based on the binding energies and effective masses calculated in Ref. [134].

In order to achieve a maximum of 2PPE intensity, photon energy of the pump photon has to be tuned to be as close as possible to the resonant transition from the occupied to the unoccupied electronic states of interest. To investigate this in more detail, in Fig. 4.3(c) we plotted the difference in energy of the three IPSs and the two surface states. Resonant transition, at a certain $k_{||}$ -value, will be achieved if the pump-photon energy coincides with the energy difference of IPSs and surface states. At the photon energy of 4.68 eV used in Fig. 4.2(a), we see that resonant transitions can be achieved to state I_1 for $0.1 \text{ \AA}^{-1} \lesssim k_{||} \lesssim 0.2 \text{ \AA}^{-1}$ and to state I_2 for $k_{||} \approx 0 \text{ \AA}^{-1}$. Also, that photon energy is just below the onset for the resonant transition to the state I_3 which explains why we

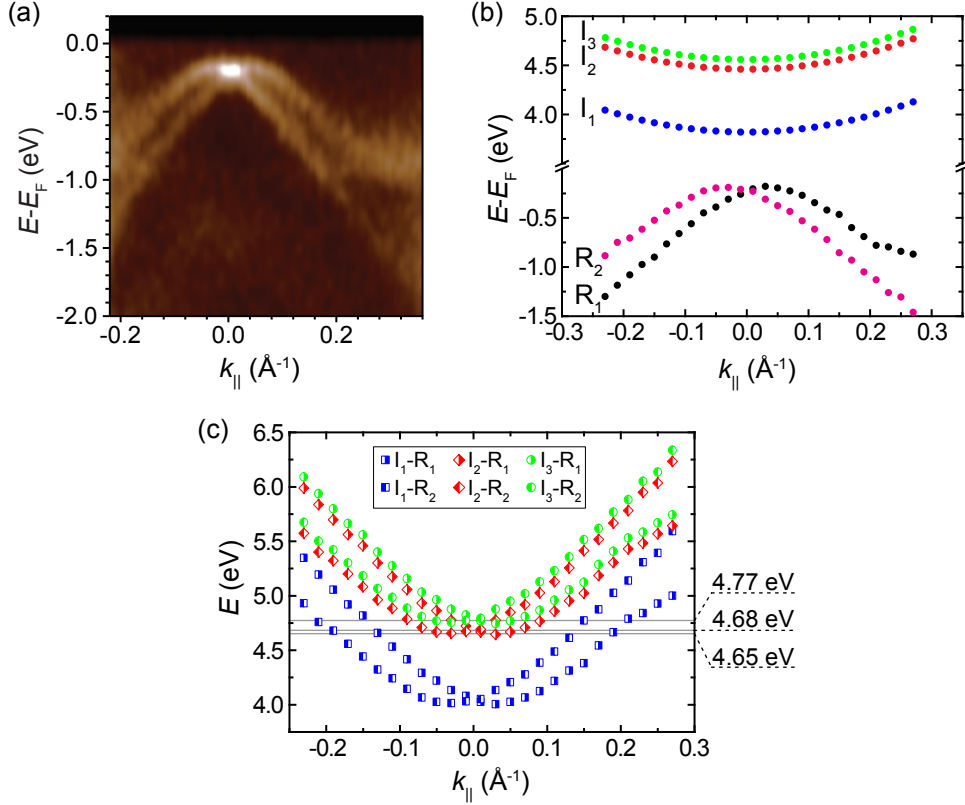


Figure 4.3: (a) ARPES spectra of the Rashba-split surface state of Gr/Ir(111). Elt-ARPES, $\parallel \Gamma K$, $\hbar\omega = 55$ eV, p -polarization, $T_S = 75$ K. (b) Data points from EDC analysis of the spectrum in (a) (R_1 and R_2) and data points representing first three IP states (I_1 , I_2 and I_3) plotted according to Ref. [134]. (c) Energy difference of the image-potential and surface states $I_n - R_m$ ($n = 1, 2, 3$, $m = 1, 2$). Several pump-photon energies used in our experiments are marked by gray horizontal lines. Resonant transition is achieved when the difference $I_n - R_m$ coincides with the pump-photon energy.

did not observe it in our 2PPE experiment in Fig. 4.2(a)—the photon energy was too low. By tuning the photon energies in the 2PPE process we have shown that the onsets for the resonant transitions to the states I_2 and I_3 (and hence for their notable visibility) are 4.65 and 4.77 eV, respectively (see supplementary material of Ref. [134]). Moreover, the effects of resonant transition at 4.77 eV of pump-photon energy to the I_1 state are clearly visible in Fig. 2(a) of Ref. [134]. The intensity of that band is the highest for $0.08 \text{\AA}^{-1} \leq k_{\parallel} \leq 0.17 \text{\AA}^{-1}$, which is in fair agreement with the prediction of Fig. 4.3(c). An additional shift of the intensity maxima to lower k_{\parallel} values is an effect of finite energy and angular resolution of the analyzer. It is safe to say that iridium Rashba spin-split surface states were indeed the initial, pump states in our 2PPE experiments. The existence of well-defined pump states ensures efficient population and high 2PPE intensity of the IPSs (cf. Fig. 4.2).

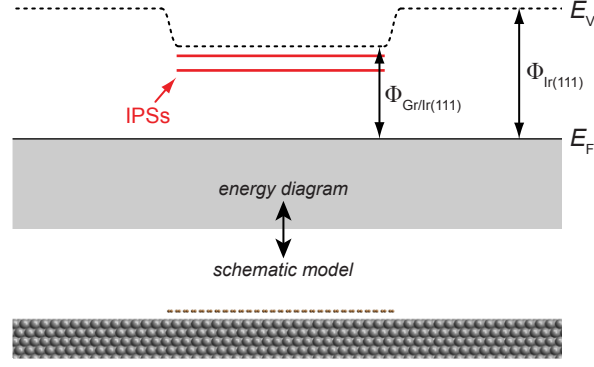


Figure 4.4: A model of graphene island on iridium and the corresponding energy diagram. Large work function difference $\Phi_{\text{Ir}(111)} - \Phi_{\text{Gr/Ir}(111)} = 1.14$ eV enables localization of the electrons occupying image-potential states at graphene islands.

In Section 3.4 we have determined the work function of 0.75 ML graphene sample which fits well to our data presented in Ref. [134]. Therein, we also observe IPSs for various graphene coverages (but not for 0 ML coverage!) and find that the energies of the states display constant energetic separation from the Fermi level (cf. Fig. 3.9). This is a direct evidence of localization of the electrons on the graphene islands because they respond only to local and not average work function which is probed in 2PPE experiments (see Fig. 4.4). We can say that the localization on the graphene islands is governed by large work function difference between bare iridium (5.79 eV) and graphene-covered iridium (4.65 eV). This is valid in situations when the average island dimension exceeds a typical distance of probability density maximum of IPS wavefunction. For the first few IPSs, this distance is of the order of nanometers while the characteristic graphene island dimension after just one TPG cycle is tens of nanometers (see Section 3.1).

The effects of confinement of electrons small islands was also studied by STS [148] where the IPSs (or more precisely field emission resonances) were registered as peaks in the local density of states (LDOS) while retracting the tip away from the sample surface. It should be noted that in their study, Craes et al. studied only small graphene islands i.e. quantum dots, where also the effects of lateral confinement come into play (these effects are irrelevant for large graphene islands). In addition, in STS experiments the electric field of the tip modifies the potential barrier confining the IPS electrons which additionally modifies the energies of IPSs. Because of these reasons, direct comparison of STS and 2PPE results is difficult. Nevertheless, in both studies electron confinement is found due to the large work function difference $\Phi_{\text{Ir}(111)} - \Phi_{\text{Gr/Ir}(111)}$.

CHAPTER 5

The mechanism and effects of caesium intercalation

Despite the large amount of literature which can be found on the intercalation of epitaxial graphene on Ir(111) with different atoms or molecules (see Section 1.6 for details), a detailed description of the intercalation process is still not given. The question of intercalation mechanism through an apparently perfect graphene membrane and the corresponding driving forces are of crucial importance for understanding of various graphene hybrid systems.

Cs intercalation of Gr/Ir(111) is used to gain insight on the fundamentals of intercalation process which can be extrapolated to some other similar epitaxial graphene systems. By monitoring Cs intercalation, with Cs atoms having one s electron in their outer shells, we are able to characterize the $s - \pi$ electronic interaction which can be used as a basic model for the interaction of intrinsic π electronic system with other, chemically added electrons. In this chapter we characterize the intercalation process by utilizing several experimental techniques. We begin with a description of phase separation of Cs as viewed by LEED, LEEM and STM. Complementary, ARPES results are presented which reveal inhomogeneous electron doping of graphene as a consequence of phase separation. Those experimental findings are in excellent agreement with theoretical calculations and together they highlight the importance of van der Waals interaction in weakly-bound epitaxial graphene systems. Besides static observations, we also reveal details of the intercalation dynamics and found its relation with structural features of graphene and iridium surface such as wrinkles and iridium steps. Additionally, by performing desorption experiments of the intercalated samples, which can be regarded as de-intercalation, we are able to fully understand all processes relevant for Cs on Gr/Ir(111). At the end of

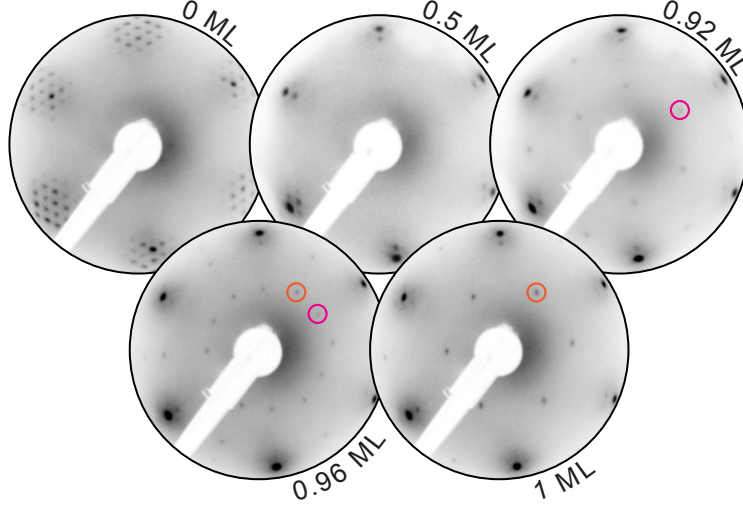


Figure 5.1: LEED characterization for the various amounts of deposited Cs (noted for each frame). All images were recorded at room temperature. Moiré diffraction spots are clearly visible for pristine graphene. A (2×2) with respect to graphene (magenta circles) and $(\sqrt{3} \times \sqrt{3})R30^\circ$ with respect to iridium (orange circles) structures are clearly resolved after reaching ~ 0.9 ML Cs coverage. Electron energies are 117 (0 ML) and 130.5 eV (other patterns).

the chapter, we deal with some additional effects observed in Cs intercalated Gr/Ir(111): quasiparticle scattering and ionic adsorption. They are common to many intercalated graphene systems and hence a comparison to some of them will be given.

5.1 Morphology and phase separation

5.1.1 LEED results

By depositing various amounts of Cs on graphene, various Cs structures are observed experimentally. Our goal is to investigate Cs structures for various coverages, up to one-layer saturation and we are not interested in the formation of multilayers or 3D clusters. It is found that the densest Cs superstructure which give sharp diffraction spots in LEED is $(\sqrt{3} \times \sqrt{3})R30^\circ$ with respect to iridium (111). The corresponding LEED image is shown in Fig. 5.1(e). Accordingly, this Cs structure is defined as 1 monolayer (ML) of Cs. If less than 1 ML of Cs was deposited, other structures were observed. For the LEED images recorded at room temperature, below ~ 0.9 ML of Cs no clear superstructure is visible [Fig. 5.1(b)]. Only after reaching 0.92 ML, a (2×2) structure with respect to graphene is apparent [Fig. 5.1(c)]. If more Cs is deposited, a mixture of (2×2) with respect to graphene and $(\sqrt{3} \times \sqrt{3})R30^\circ$ with respect to iridium superstructure is found

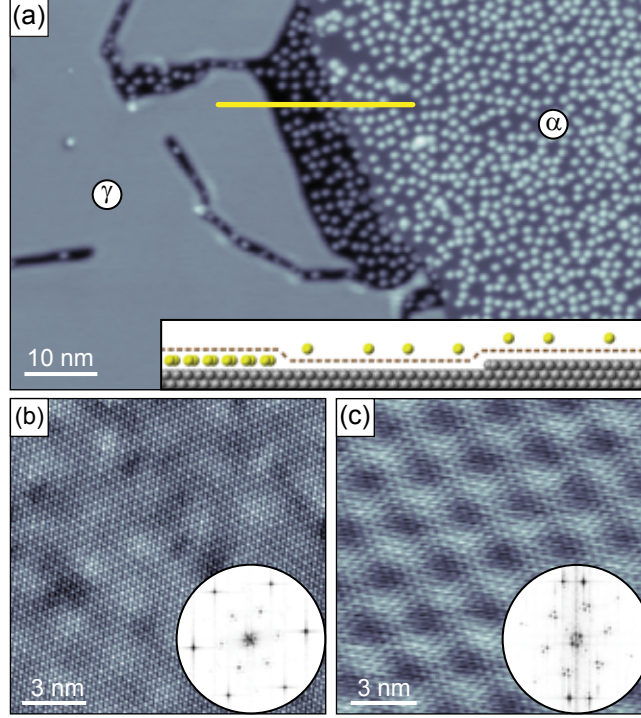


Figure 5.2: (a) An STM topograph of two characteristic areas found after the deposition of 0.5 ML of Cs on Gr/Ir(111): the adatom α -phase and the intercalated γ -phase. The inset shows a schematic illustration of the topographic profile across different regions as indicated by a yellow horizontal line. $U_t = 1$ V, $I_t = 10$ pA. (b,c) High-resolution STM topographs of two different superstructures revealed in the γ -phase areas: (2×2) relative to Gr in (b) and $(\sqrt{3} \times \sqrt{3})R30^\circ$ relative to Ir in (c). The circular insets show the corresponding Fourier transforms. Imaging conditions: (b) $U_t = 120$ mV, $I_t = 300$ pA and (c) $U_t = 40$ mV, $I_t = 300$ pA.

[Fig. 5.1(d)] which corresponds to ~ 0.96 ML of Cs. Consequently, further Cs deposition gives 1 ML samples.

The fact that Cs forms a structure with respect to iridium is strong evidence of possibility of Cs intercalation of epitaxial graphene. Clearly, Cs atoms easily switch their preference in binding from graphene to iridium as 1 ML coverage is reached. It should also be noted that the intensity of moiré diffraction spots is strongly reduced after Cs deposition which indicates that the amplitude of moiré superstructure is reduced.

5.1.2 STM results

After deposition of 0.5 ML of Cs at room temperature and cooling the sample to 6 K prior to STM measurements (to enable stable imaging), two characteristic areas can be distinguished on the sample. This is shown in Fig. 5.2(a) where we identify bright protrusions as Cs adatoms adsorbed on top of graphene and we name this Cs phase as

the α -phase, in accordance with previous studies [149]. The concentration of adatoms as obtained from a series of STM measurements varies slightly over the sample surface with the maximum corresponding to hexagonally arranged atoms (cf. Fig. 5.14) at a nearest neighbor distance of (1.86 ± 0.01) nm—that is, 0.063 ML which is equivalent to a (7.6×7.6) superstructure with respect to graphene (for more structural details of the α -phase see Section 5.7). In contrast, it was found that Cs atoms deposited on graphite (0001) surface at room temperature can form much denser superstructures, the densest being $(\sqrt{3} \times \sqrt{3})R30^\circ$ [150].

The flat area of Fig. 5.2(a) is apparently 0.4 nm higher than its surrounding, indicative for the presence of an additional dense layer, which we attribute to the intercalated Cs atoms forming compact islands. The corresponding Cs phase is labeled as the γ -phase. Obviously, phase coexistence in this system is possible and the two observed phases are separated by a sharp interface. A more detailed STM characterization of the γ -phase is possible through high-resolution STM imaging. The STM topographs in Fig. 5.2(b) and (c) show atomic resolution obtained while scanning over two different intercalated areas. In both images, one can resolve the graphene unit cell as well as a weak moiré superstructure. This is also visible in the Fourier transforms of the STM images shown in Fig. 5.2(b) and (c) insets. A closer inspection of the images and their Fourier transforms enables an identification of the two different underlying Cs superstructures: the (2×2) structure relative to graphene [panel (b)] and the $(\sqrt{3} \times \sqrt{3})R30^\circ$ structure relative to iridium [panel (c)]. The STM findings are thus fully in agreement with LEED characterization (cf. Fig. 5.1). All relevant (super)structures found in the two Cs phases are summarized in Table 5.1.

While scanning over different areas of the γ -phase with STM, a network of thin,

Table 5.1: A summary of various Cs superstructures and corresponding phases as determined via LEED and STM (w.r.t. = with respect to).

(super)structure	Cs unit cell area (\AA^2)	nominal coverage (ML)	allocated Cs phase
(1×1) w.r.t. Gr	5.20	3.68	n/a
(1×1) w.r.t. Ir	6.38	3.00	n/a
$(\sqrt{3} \times \sqrt{3})R30^\circ$ w.r.t. Ir	19.14	1.00	γ -phase
(2×2) w.r.t. Gr	20.79	0.92	γ -phase
(7.6×7.6) w.r.t. Gr	299.61	0.063	α -phase

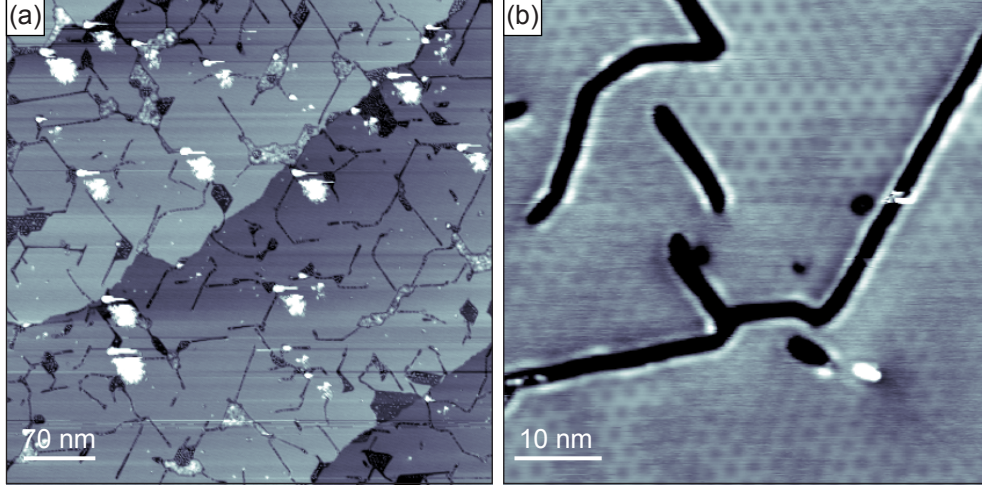


Figure 5.3: (a) A network of channels formed within the γ -phase as imaged by STM. The network consists of straight segments with an average length of several tens of nanometers. $U_t = 1$ V, $I_t = 100$ pA. (b) A zoom-in at several interconnecting channels. $U_t = 2$ V, $I_t = 100$ pA.

partially interconnecting channels can be found as shown in Fig. 5.3(a). The channels stretch out predominantly in three directions which form an angle of approximately 60° or 120° with respect to each other. That kind of morphology suggests close connection to the hexagonal symmetry of Gr/Ir(111) system. Indeed, it was shown in Ref. [86] for the case of Eu intercalation that these kind of channels are closely related to the inhomogeneous binding of graphene to iridium within the moiré unit cell. Additional factor in channels formation are changes in strain within graphene which are induced by intercalation. A closer view at several channels is given in Fig. 5.3(b). There, the moiré pattern can also be resolved and it can be clearly seen that the direction of the channels coincides with the three high-symmetry directions of the moiré.

5.1.3 LEEM results

The process of Cs adsorption and intercalation was also examined by LEEM at 370 K. Fig. 5.4(a) shows pristine graphene on Ir(111). Dark, straight lines are graphene wrinkles which were described and analyzed in Section 1.4. Also, iridium steps are visible as wavy lines extending in the entire field of view. Cs deposition was monitored in real-time and resulted in a sequence of LEEM images, so-called stack. Images from a stack were recorded each second (which defines temporal resolution of a stack) and can be analyzed separately.

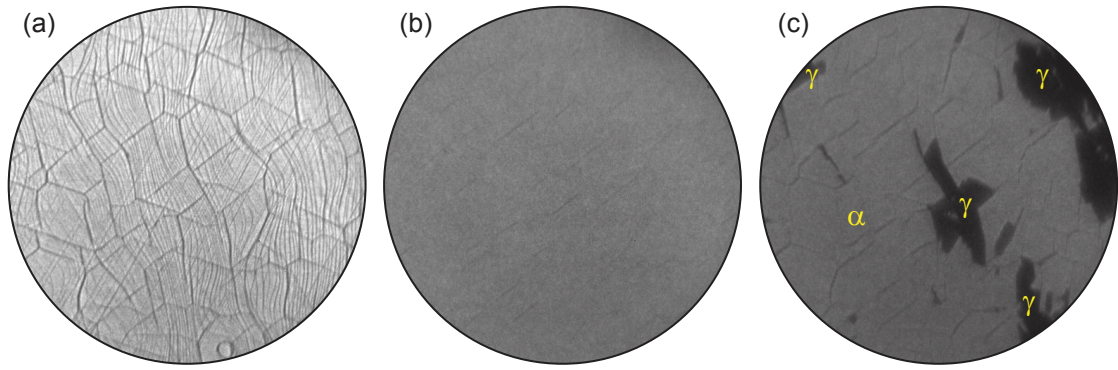


Figure 5.4: A sequence of LEEM images for various amounts of deposited Cs. (a) 0 ML. Graphene wrinkles and iridium steps are resolved as thicker and thinner lines, respectively. (b) ~ 0.06 ML. The whole sample is covered by the α -phase. (c) ~ 0.2 ML. Intercalated Cs islands appear, the α - and the γ -phase coexist on the sample. The focus of the instrument was readjusted in (b) and (c) in order to optimize visibility of emerging Cs structures. FOV = $14 \mu\text{m}$, $E = 1.5 \text{ eV}$, $T_S = 370 \text{ K}$.

The first change visible in LEEM after the start of Cs deposition is the overall moderate decrease in reflectivity, as can be seen by comparing Fig. 5.4(a) and (b). This change is attributed to the formation of the dilute α -phase. Since a decrease in reflectivity is homogeneous in the entire field of view, we conclude that Cs atoms spread evenly across the graphene surface. Further deposition of Cs yields appearance of distinct dark contrast on certain areas of the sample. Fig. 5.4(c) shows the sample surface after deposition of 0.2 ML of Cs. Randomly distributed dark patches of irregular shape are visible. They are attributed to the intercalated γ -phase. Obviously, phase separation can also be identified in LEEM as two contrasts which both differ from pristine Gr/Ir(111) contrast.

Additional insight comes from *IV*-LEEM spectroscopy of pristine and partially intercalated samples. Fig. 5.5 shows characteristic electron energy-dependent reflectivity curves

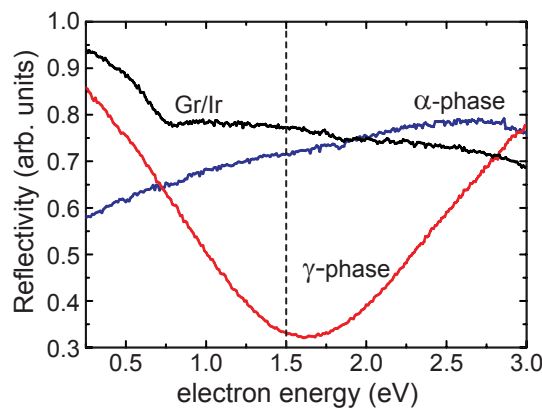


Figure 5.5: Three *IV*-LEEM curves recorded at three different areas on the sample. Dashed vertical line marks 1.5 eV, an electron energy used for imaging in Fig. 5.4.

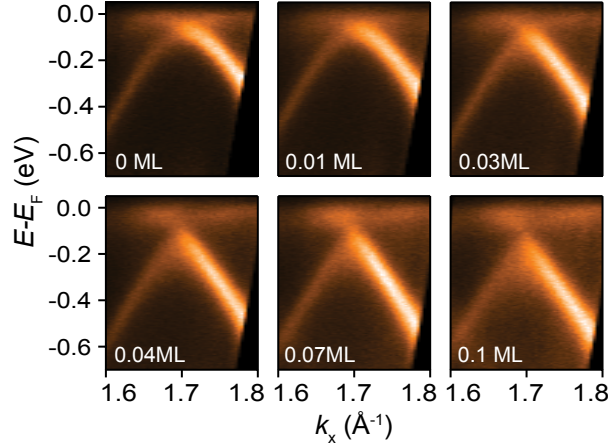


Figure 5.6: A sequence of ARPES spectra for various amounts of Cs in the α -phase (parallel to ΓK , azimuthal offset $\lesssim 1^\circ$). A continuous shift of the Dirac cone to higher binding energies is evident as more Cs is added. Zg-ARPES, $\parallel \Gamma K$, $\hbar\omega = 21.2$ eV, mixed polarization, $T_S = 300$ K.

extracted from pristine Gr/Ir(111), the α -phase and the γ -phase area on the sample. The difference between those three curves is evident which is a clear sign of formation of two dissimilar Cs phases on the sample. A dip in the reflectivity of the γ -phase is visible—a feature which is a clear indication of the formation of a new dense layer [151], in this case intercalated Cs layer. By comparing the values of three curves in Fig. 5.5 at 1.5 eV which was the electron imaging energy used in Fig. 5.4, one can easily understand the origin of contrast differences in Fig. 5.4.

5.2 Electronic structure

First we analyze the effects of α -phase formation on the electronic structure of graphene. A sequence of six ARPES maps around the graphene K point for various adatom gas concentrations is shown in Fig. 5.6. The approximate amount of deposited Cs is indicated in each panel. Pristine Gr/Ir(111) is characterized by a sharp Dirac cone, exhibiting slight p -doping of graphene, consistent with previous experiments [46, 47]. The deposition of Cs leads to the following modifications of the ARPES spectra: for Cs coverage of up to ~ 0.1 ML, the Dirac cone of slightly p -doped pristine graphene on iridium shifts continuously to higher binding energies as the Cs coverage is increased. The maximum shift of the Dirac point is ~ 0.2 eV below the Fermi level, making graphene slightly n -doped. From the ARPES spectra we obtain that the maximum electron doping in the α -phase is $n \approx 4 \times 10^{12} \text{ cm}^{-2}$ corresponding to a charge transfer of 0.11 electrons from each Cs atom in the α -

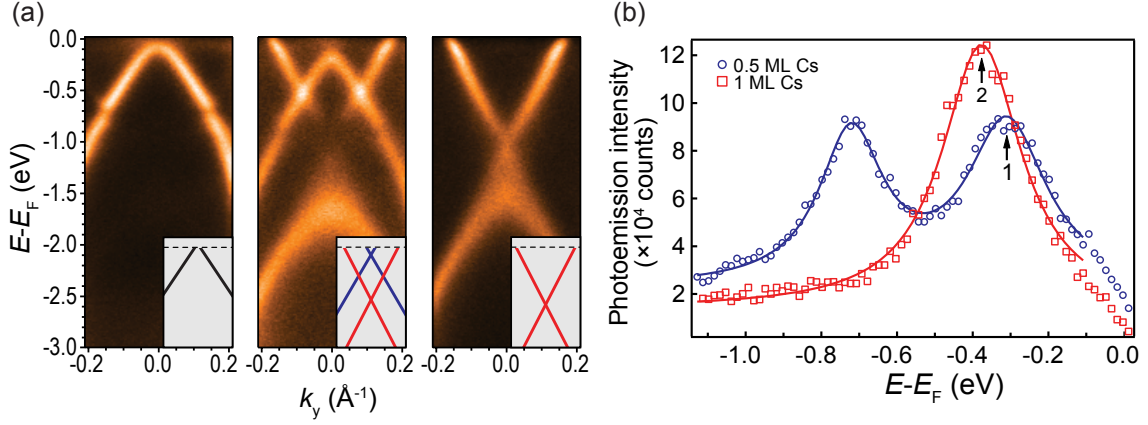


Figure 5.7: (a) ARPES spectra of 0 ML (left), 0.5 ML (center) and 1 ML (right) of Cs. Insets schematically indicate visible Dirac cones corresponding to pristine (black), light (blue) and heavy (red) electron-doping. BNL-ARPES, \perp Γ K, $\hbar\omega = 23.4$ eV, p -polarization, $T_S = 300$ K. (b) EDC data points (symbols) and the corresponding Lorentzian fits (full lines) taken at $k_y = -0.12$ \AA^{-1} of the center and right spectra in (a). Arrows 1 and 2 indicate the fitted positions of the π^* bands.

phase to graphene. Due to the small starting density of states at the Fermi level of pristine e-Gr/Ir [46], even a small charge transfer leads to notable shifts of the Dirac cone. Charge transfer also explains the origin of adatom binding to graphene. Once the Cs atom gets close enough to graphene, its s-electron partially delocalizes within graphene and lowers the total energy of the system. The result of this is adsorption i.e. formation of the α -phase.

For more than ~ 0.1 ML of Cs, an additional Dirac cone appears at higher binding energy (with Dirac point at 1.13 eV below the E_F) due to phase separation; center panel in Fig. 5.7(a) corresponds to 0.5 ML of Cs and it shows two Dirac cones, light and heavily electron doped, corresponding to the α -phase and the γ -phase, respectively. The α -phase cone decreases in intensity and completely disappears above ~ 0.9 ML of Cs and only the γ -phase cone remains visible. Once the entire sample is covered by the γ -phase, additional deposition from 0.9 ML to 1 ML [right panel in Fig. 5.7(a)] increases its density (consistent with the evolution of the LEED patterns, cf. Fig. 5.1) and an additional shift of the Dirac point to 1.20 eV below E_F is observed. Denser Cs packing implies more charge transfer to graphene which is reflected in the shift of the Dirac point. This is depicted in Fig. 5.7(b) where we show two energy distribution curves (EDCs) of the 0.5 $[(2 \times 2)]$ structure of the γ -phase and 1 ML sample $[(\sqrt{3} \times \sqrt{3})R30^\circ]$ structure of the γ -phase taken at the same wavevector $k_y = -0.12$ \AA^{-1} . The maximum doping of $n \approx 1 \times 10^{14}$ cm^{-2} , calculated via Eq. 1.2, implies a charge transfer of 0.20 electrons per

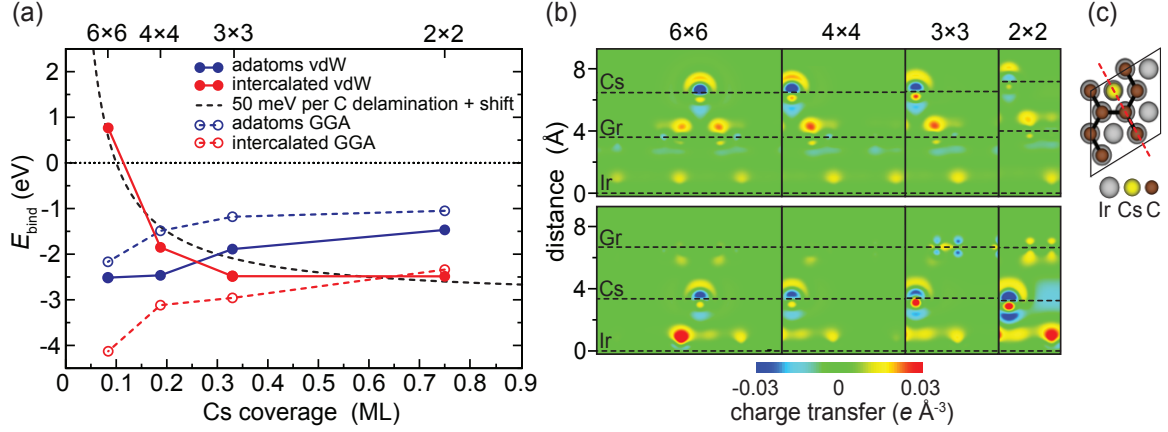


Figure 5.8: DFT results of adsorbed and intercalated structures of Cs. **(a)** Binding energies (E_{bind}) as a function of Cs coverage for the intercalated and the adatom phases. The open symbols and dashed lines show the results obtained using the GGA functional, whereas the full symbols and full lines are obtained with the inclusion of the non-local vdW correlation. The dashed black line is a guide to the eye simulating a 50 meV delamination energy per C-atom plus a constant offset. **(b)** Charge transfer in the adatom phase (upper row) and in the intercalated phase (lower row). The corresponding Cs concentrations are marked on top of the panel. Black-dashed lines indicate the positions of Ir, Gr and Cs layers. **(c)** A model indicating the position of a geometric plane (dashed red) across which the charge transfer in (b) is plotted.

Cs atom in the γ -phase to graphene.

5.3 Theoretical calculations

In this section we present the main results of DFT calculations on Cs intercalation. Details of the calculations can be found in Ref. [152]. Fig. 5.8(a) shows binding energies for different Cs concentrations (marked on top of the graph) corresponding to the adatom and intercalated phases. The plotted values are given per unit cell used in the calculations and referenced to the corresponding pristine Gr/Ir(111) system plus a free Cs atom. Calculations with the vdW interaction included (full lines) show a clear crossover between the adatom and intercalated phases for dilute and dense concentrations, respectively. This means that there is a switch in preference from adatoms to intercalation as Cs concentration gets higher which is in full agreement with our experimental results. In order to determine the importance of the vdW interaction, in Fig. 5.8(a) we also present the results obtained using a semi-local functional (GGA), which does not contain the vdW correlation effects. This functional fails to correctly describe the experimental observations.

For considered Cs concentrations, the charge transfer in the adatom and the intercalated phase is visualized in Fig. 5.8(b). Looking at the charge transfer alone, the main difference between the intercalated and the adatom structure comes from the much larger amplitudes of charge rearrangement in the intercalated system. There, the Cs atom causes a large redistribution of charge on both, the Ir surface and the graphene [lower row of Fig. 5.8(b)], mimicking the electrostatic glue for floating n -doped graphene. In contrast, in the adatom case most of the charge rearrangement takes place on the graphene sheet close to Cs [upper row of Fig. 5.8(b)]. Charge rearrangement is also closely connected to the spacing between Gr, Cs and top-Ir layer. The most significant to us is the Gr-Ir distance in both the adatom and the intercalated phase, since it is an indicator of the vdW interaction strength between graphene and iridium. Table 5.2 summarizes these distances. Because of the long-range reach of vdW force, corresponding attractive interaction is not negligible even for the largest Gr-Ir distances and it provides stable binding of graphene in both adatom and intercalated case (see supplement of Ref. [152]). From Table 5.2 we see that Gr-Ir distance significantly increases upon Cs intercalation (almost doubles at lower Cs concentrations), meaning that a substantial amount of energy has to be given to the system in order for the intercalation to be energetically favorable. The calculated Gr-Ir distances for the intercalated phase are very close to 6.27 Å as measured in the experiments [153]. In the next section we explain what is the origin of this intercalation-enabling energy.

5.4 Driving forces for intercalation

Knowing the morphology and electronic structure of the Cs + Gr/Ir(111) system backed up by theoretical calculations, we propose a complete picture of the mechanisms which governs the intercalation (cf. Fig. 5.9). In order to delaminate graphene from iridium, 50 meV of energy per C atom has to be invested into the system [51]. For small Cs concentrations, this energy cost is too high because one Cs atom would have to delaminate

Table 5.2: Graphene-iridium distances for various Cs structures in the adatom and the intercalated phase as calculated from DFT with the inclusion of the vdW interaction.

Cs phase	(6 × 6)	(4 × 4)	(3 × 3)	(2 × 2)
adatom phase	3.60 Å	3.60 Å	3.60 Å	4.00 Å
intercalated phase	6.74 Å	6.74 Å	6.74 Å	6.71 Å

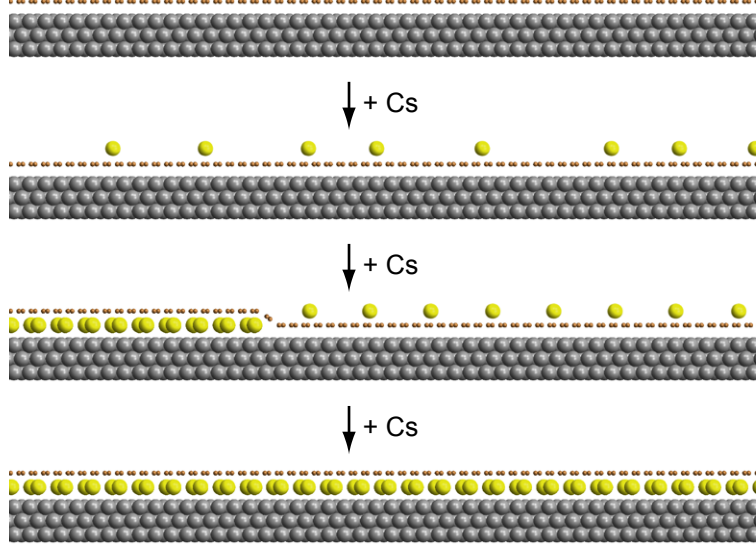


Figure 5.9: A model of Cs adsorption and intercalation on Gr/Ir(111), starting from a clean graphene on iridium (top) and ending with a completely intercalated Cs layer (bottom).

many C atoms. In that case it is more favorable for Cs atoms to form the adatom α -phase. As more Cs is added to the α -phase, the average distance between the charged adatoms gets smaller and yields an increase in the Coulomb repulsion penalty. Thus, the binding energy of the adatoms decreases. At a critical Cs concentration of 0.063 ML as determined from STM, intercalation becomes favorable because the cost for graphene delamination is then shared among many Cs atoms. In addition, once the partially ionized Cs atoms are intercalated, they are screened by the electrons from the iridium substrate which lowers the Coulomb penalty and increases the binding energy of Cs atoms in the γ -phase. Evidently, one of the key concepts in the intercalation mechanism is delamination which reflects the vdW nature of binding of graphene to iridium.

5.5 Intercalation dynamics

5.5.1 Graphene on Ir(111)

In addition to the effects attributed to the phase separation described in the previous sections, LEEM stacks recorded during Cs deposition provide information on the kinetics of the intercalation process. In Fig. 5.10 we display several snapshots extracted from one such stack. There, the same area of the sample [the area indicated by yellow square in

Fig. 5.4(a)] recorded at the indicated incremental times is shown. The analysis shows that the growth of the γ -phase is discontinuous, composed of sudden and rapid advancements followed by extended periods of stagnation. An area of pristine Gr/Ir(111) is shown in Fig. 5.10(a). In Fig. 5.10(b) the same area is shown but with the highlighted network of wrinkles (full lines) and steps (dotted lines). They divide the surface into an assembly of small tetragonal micro-tiles. We find that these features are essential for the evolution of the intercalated phase. In particular, the γ -phase always forms next to wrinkles, typically at crossing points of wrinkles. Almost at any time, all boundaries of such intercalated islands are identified as wrinkles or surface steps [Fig. 5.10(c)-(i)]. Hence their expansion can be described as tiling. Once the intercalated Cs island has nucleated, discontinuity of its expansion depends more strongly on the network of Ir steps, since this network is almost an order of magnitude denser than that of wrinkles—for the characteristic surface area studied in our work, surface densities are $1 \mu\text{m}^{-1}$ for wrinkles and $7 \mu\text{m}^{-1}$ for steps. Ir steps play the role of a kinetic barrier for diffusion of intercalated Cs atoms. An example of a tiling step is highlighted in panels (h) and (i) of Fig. 5.10 where an arrow points to an empty and filled tile, respectively. A movie showing the process of Cs adsorption and intercalation generated from a LEEM stack can be found as a part of the supplementary information of Ref. [152].

Since intercalated islands nucleate at crossing points of wrinkles, we assume that the entrance points for Cs atoms to pass under graphene are nano-scale cracks located at these crossing points. Although it is not possible to resolve cracks in highly distorted regions of wrinkles crossings [cf. Fig. 3.17(d)], their crumpling is consistent with being the entry areas for Cs atoms. It was proposed that a vacancy defect greater than four missing carbon atoms is needed to allow Cs intercalation to subsurface layers of graphite since e.g. the diffusion barriers for Cs atoms through 4- and 6-atom vacancies are 7.1 and 1.78 eV, respectively [100]. Wrinkles crossings are perfect candidates for containing such (and larger) defects. Less extensive defects have already been characterized by STM in epitaxial graphene samples; small graphene rotations within the sheet resulted in an array of heptagon-pentagon pairs [10] and larger rotations in nanometer-wide grain boundaries [154]. Although our LEED data indicate uniform graphene, small rotations (e.g. below 1°) and the existence of heptagon-pentagon pairs cannot be entirely excluded. However, the LEEM and STM data indicate that highly defective areas at wrinkles crossings enable

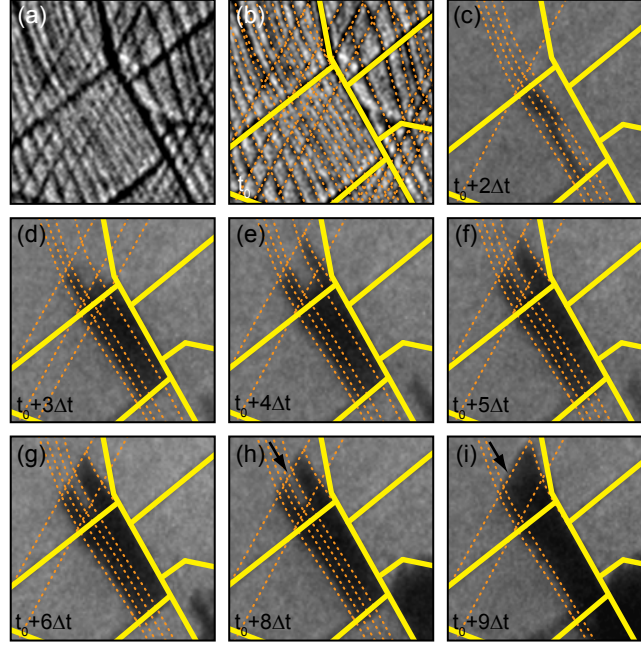


Figure 5.10: A series of $(2.52 \times 2.52) \mu\text{m}^2$ LEEM frames showing the same surface area (a), (b) before any Cs deposition and (c)–(i) after the appearance of the dark intercalated Cs islands. Snapshots were imaged at the indicated time intervals ($\Delta t = 72$ s) with respect to t_0 , the reference time when image (a) was taken. In (b), the entire network of wrinkles and steps is highlighted by full and dotted lines, respectively. In (c)–(i), only wrinkles and relevant steps are highlighted. In the last two panels, an arrow indicates an empty (h) and a filled tile (i).

the transport of atoms across graphene layers. The role of these entry cracks is additionally described in the desorption experiment in Section 5.6. The importance of wrinkles in the intercalation process is also stressed in Ref. [155] from another angle where Co intercalation of Gr/Ir(111) is studied. There the authors show that intercalation is facilitated at graphene wrinkles and also iridium steps which is explained by an increased probability of temporary vacancy formation at these strongly curved sites in the presence of Co clusters.

5.5.2 Graphene on Ir(100)

The role of substrate in intercalation can be further corroborated by examining intercalation dynamics of graphene grown on surfaces other than (111). We characterize Cs intercalation of graphene on a small-angle miscut Ir(100)-(5 × 1)-hex substrate (see Subsection 3.1.3 for a more detailed description of this substrate). The choice of this specific crystal is eligible in this case since large, parallel terraces can be found in only one dimension which is ideal for examining the influence of substrate steps on the intercalation

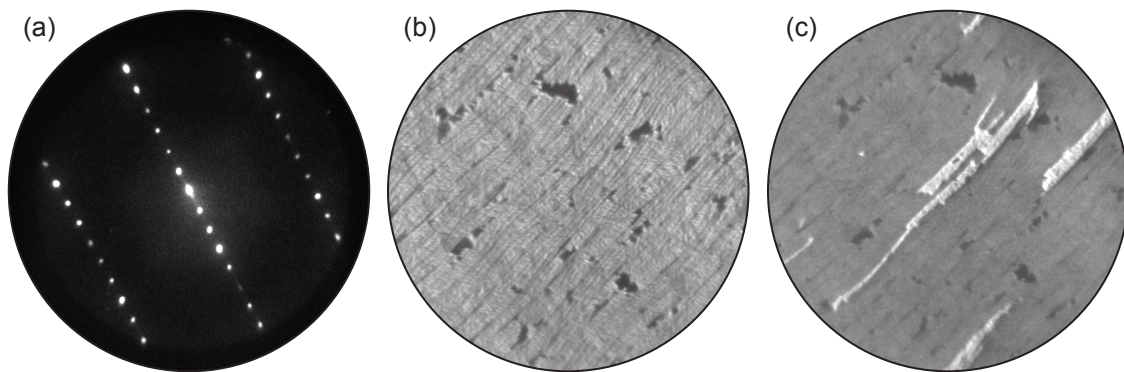


Figure 5.11: (a) LEED pattern of a small-angle miscut (100) surface of iridium exhibiting (5×1) reconstruction in one direction. $E = 40$ eV. (b) LEEM image of graphene grown on vicinal Ir(100). Iridium steps are visible as straight lines running diagonally through the image. Several impurities or uncovered areas are visible as dark patches. (c) The same area as in (b) after partial Cs intercalation took place. Cs islands (bright contrast) morphology follows the morphology of the iridium substrate. In (b) and (c): FOV = $9.3 \mu\text{m}$, $E = 4$ eV, $T_S = 370$ K.

process. The preservation of such one-dimensional structuring even after graphene synthesis is confirmed by LEEM image of Ir terraces and the corresponding steps in Fig. 5.11(b). The same area on the sample after deposition of Cs is shown in Fig. 5.11(c). Elongated intercalated Cs islands are visible and the direction of elongation obviously coincides with the direction of extension of Ir steps. This is a clear demonstration of the role of Ir steps as a barrier for diffusion of intercalated Cs atoms—Cs atoms diffuse much easier along the terrace than across the step.

5.6 De-intercalation

Once the sample is fully intercalated i.e. 1 ML of Cs is deposited, desorption or more precisely de-intercalation dynamics of Cs can be investigated. In Fig. 5.12 we show several LEEM images recorded at several temperatures during annealing of fully intercalated sample up to 1080 K at a rate of ~ 4 K/s. Dark contrast corresponds to the γ -phase and bright contrast corresponds to pristine Gr/Ir(111), as determined by comparison to Cs deposition experiments. By looking at the whole recorded LEEM stack, it can be concluded that the desorption takes place only above 770 K [Fig. 5.12(b)] and that even after reaching 1080 K well defined areas of the γ -phase still exist on the sample [Fig. 5.12(d)]. In order to make this more quantitative, we analyzed the area of the γ -phase as a function of sample temperature. The result is shown in Fig. 5.13(a). The γ -phase is

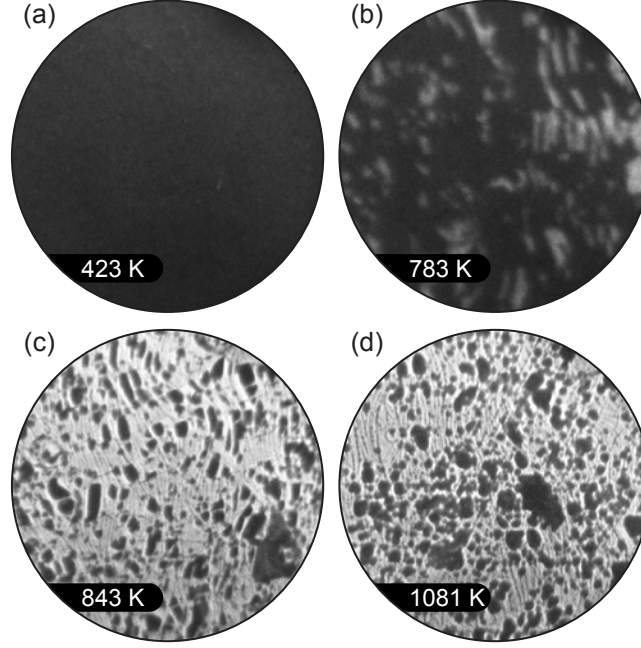


Figure 5.12: A sequence of LEEM images recorded at four different temperatures during annealing of fully intercalated (1 ML of Cs) Gr/Ir(111) sample. Completely intercalated Cs layer remains stable up to ~ 770 K while individual intercalated Cs islands are stable up to ~ 1080 K. Due to thermal drift, different images show different areas of the sample. FOV = $14\ \mu\text{m}$, $E = 2.4\ \text{eV}$.

stable up to 770 K when sudden de-intercalation of Cs atoms starts. This process lasts up to 820 K when 80% of the γ -phase contrast is lost and replaced by the contrast equivalent to pristine Gr/Ir(111). Further increase in the temperature does not alter the area of the γ -phase i.e. Cs islands remain trapped under the graphene even at high temperatures. A movie of Cs desorption can be found in the supplementary information of Ref. [152].

We interpret the desorption dynamics and its interruption as sketched in Fig. 5.13(b). At about 770 K, desorption takes place, by the principle of micro-reversibility, through the same channels that enabled intercalation—cracks in graphene associated with wrinkles. When the Cs concentration falls below a critical value, graphene will relaminate to Ir (cf. arrows in Fig. 5.13(b) lowermost panel). This will take place first in the surroundings of the entry/exit spots where the Cs has already been lost. Once an exit spot is surrounded entirely by relaminated graphene, desorption is not allowed through this spot any more. Eventually, very stable Cs pockets are trapped through the vdW adhesion of graphene to Ir(111). Once again, vdW interaction have proven to be essential in this system.

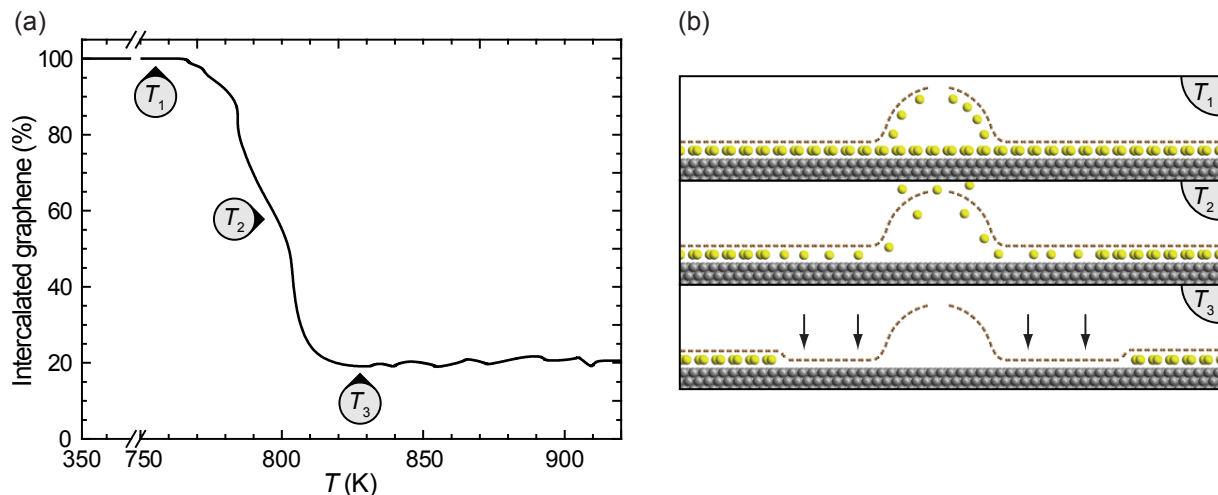


Figure 5.13: (a) A plot of the area-integrated γ -phase contrast as a function of temperature extracted from a LEEM stack. Whole desorption dynamics takes place in the narrow temperature range between 770 and 820 K. (b) Schematic sketch of the system structures at various temperatures: right before desorption starts (T_1), during intensive Cs desorption (T_2) and after desorption is suppressed by relamination of graphene (T_3), as indicated by arrows.

5.7 Adatom interaction in the α -phase

Basic properties of the α -phase are given in Section 5.1. Here we describe it in more detail. As already mentioned, various concentrations of Cs atoms can be found in the α -phase. Fig. 5.14 shows several Cs concentrations as imaged by STM. Regardless of the concentration, hexagonal ordering of the adatoms is apparent. The origin of this ordering is, of course, the effective potential acting on the adatoms. In the case of adsorption of Cs to Gr/Ir(111), contributions of the two potentials are relevant: (i) Coulomb repulsion between partially ionized Cs adatoms and (ii) graphene moiré potential acting on each individual Cs adatom. The importance of Coulomb repulsion is easily understood because of the charge transfer from Cs to graphene. Evidence that moiré potential is also crucial comes from the STM images. In Fig. 5.14(a) we highlighted several Cs adatoms by arrows. If only Coulomb repulsion would govern the arrangement of the adatoms, then they would migrate to sites energetically more favorable to them, which would certainly be further away from other adatoms. For low concentrations such as in Fig. 5.14(a) this would also yield random distribution of the adatoms. Therefore we speculate that hexagonal ordering inherited from the underlying moiré is established.

The influence of moiré is also visible for maximum adatom concentration we observed

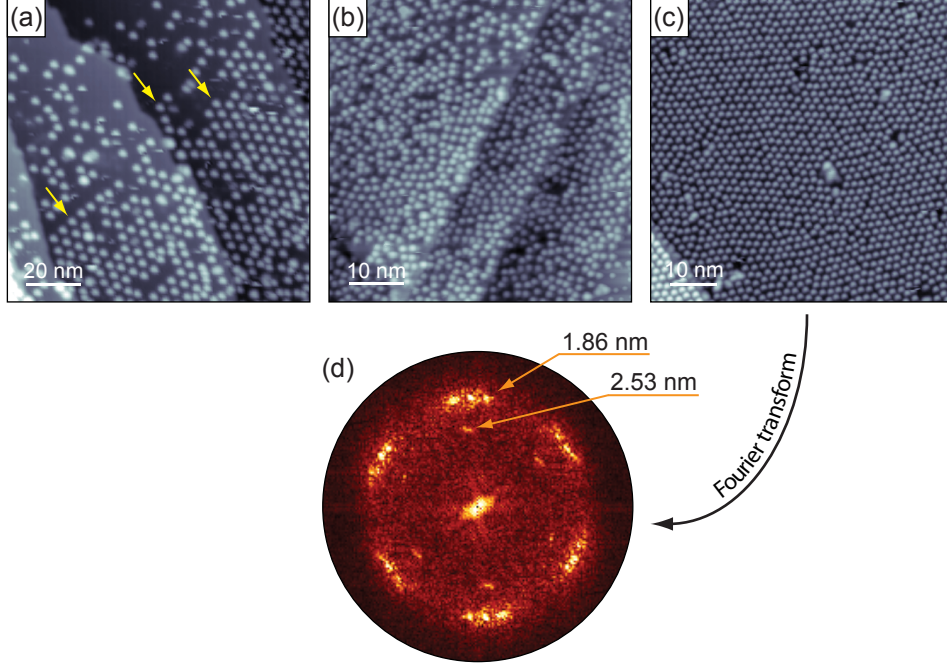


Figure 5.14: STM images of Cs adatoms in the α -phase at various concentrations (obtained by counting the Cs atoms): (a) 0.037 nm^{-2} ($U_t = 1.5 \text{ V}$, $I_t = 100 \text{ pA}$), (b) 0.296 nm^{-2} ($U_t = 1 \text{ V}$, $I_t = 80 \text{ pA}$) and (c) 0.334 nm^{-2} ($U_t = 1 \text{ V}$, $I_t = 81 \text{ pA}$). (d) Fourier transform of topograph from (c). Two marked periodicities are resolved, the smaller one is additionally split into three distinct orientations.

in STM shown in Fig. 5.14(c). The corresponding Fourier transform shown in Fig. 5.14(d) clearly demonstrates that the Cs adatoms are hexagonally ordered. This kind of ordering might be found in a system of adatoms deprived of any influence from the substrate and thus interacting only via repulsive Coulomb force. But in addition to hexagonal ordering, two characteristic periodicities are revealed in the FT: 1.86 nm and 2.53 nm. The first one corresponds to the average adatom-adatom distance in Fig. 5.14(c) as can be confirmed by e.g. inverse FT. The second one is an additional modulation of the 1.86 nm periodicity by moiré structure which is known to be 2.52 nm [41]. This moiré periodicity cannot be seen in the arrangement of the adatoms in STM image itself, but can be picked up by the FT. Also, the two periodicities are in very good rotational registry which is an additional proof of the influence of the moiré structure on the adatom arrangement. This indicates that there is some sort of preference in binding of Cs adatoms to specific sites within the moiré unit cell. This can be understood knowing that all carbon atoms within a single moiré cell are not equivalent; in hcp and fcc regions graphene exhibits a weak covalent bond to the iridium [51]. This inhomogeneity in binding to the substrate is then reflected, by means of corrugation and inhomogeneous chemical properties of graphene,

to more or less favorable sites for Cs adsorption. In combination with Coulomb repulsion, this yields hexagonal moiré-aligned structure of Cs adatoms. Similar observations have been made in the case of Cs adsorption on graphene on 6H-SiC(0001) [156]. There, the authors find that the hexagonal arrangement of the adatoms is governed by the monopole Coulomb repulsion as well as the inhomogeneous substrate potential originating from a 6×6 superperiodic reconstruction of the buffer layer. The preference in binding to specific sites within a 6×6 supercell is explained by an increased chemical activity of graphene regions exhibiting the largest curvature.

We also note one more specificity of the Cs adatom gas on graphene: the 1.86 nm spots in the FT [cf. Fig. 5.14(d)] are split in three clearly resolved individual spots which all correspond to the same wavelength. The splitting between two neighboring spots is $\sim 8^\circ$. The splitting i.e. the existence of three slightly rotated adatom domains is found only for the highest observed Cs concentrations. The origin of this domain formation is not clear yet. Various graphene rotations are excluded since then also 2.53 nm spots would appear split in the FT. Additional STM measurement and simulations are required in order to explain this phenomenon.

Ordering of adatoms (to a higher or lower degree) on various surfaces has been reported earlier. In many cases, the adsorbing surfaces were noble metals [157–161], where one of the key factors relevant for adatom arrangement are substrate surface states. In Gr/Ir(111), it is expected that the surface states of Ir should not have a significant influence on the adsorption because of the spatial separation of Ir surface layer and Cs adatoms.

5.8 Quasiparticle scattering

Despite large uniformity of graphene on Ir(111), various imperfections such as adsorbates, defects or substrate steps are often found by e.g. scanning probe techniques. These imperfections are a source of electron scattering in graphene which can be investigated experimentally. In this section we examine quasiparticle scattering on Cs intercalated Gr/Ir(111). It is shown in Section 5.2 that Cs intercalation n -dopes epitaxial graphene which is reflected in the shift of the Dirac point to higher binding energies, i.e. the Fermi level shifts up in energy. Upon Cs intercalation, the Fermi contour area (A_{FC}) increase proportionally to the amount of charge transferred (n) to the graphene, $A_{FC} = \pi^2 n$. This

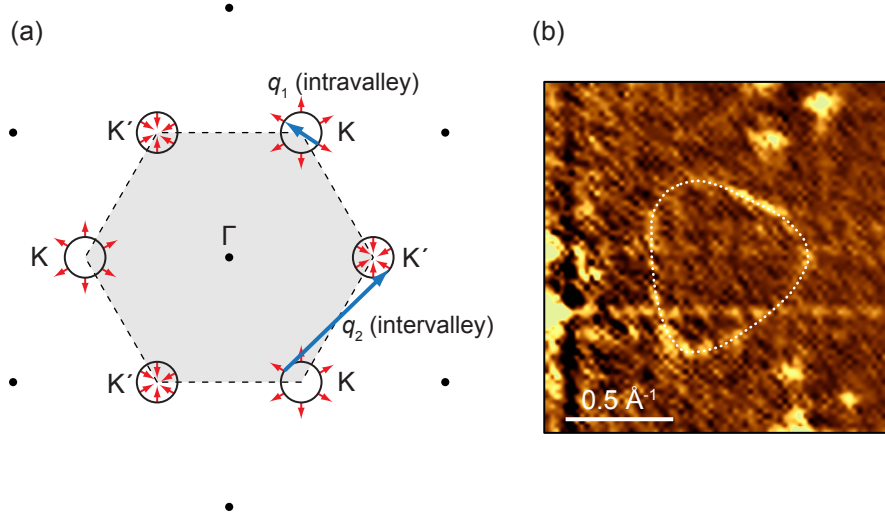


Figure 5.15: (a) An illustration of the first BZ of graphene (gray hexagon) along with six Dirac cones i.e. six Fermi contours (black circles centered at K and K' points) representing the Fermi surface and electronic states which are available for scattering processes. Intravalley scattering (marked as q_1) involves electronic states from a single Dirac cone while intervalley scattering (marked as q_2) involves electronic states from the neighboring cones. Red arrows indicate pseudospin of the Dirac electrons. Black dots are reciprocal lattice points. (b) A detail from the FT-STM map from Fig. 5.16(b) at the corner of graphene BZ. A contour corresponding to intervalley scattering (highlighted by a dotted line) can be resolved.

kind of phase-space availability increase also increases the number of possible scattering channels. In graphene, quasiparticle scattering can be categorized as intravalley and intervalley scattering [162, 163]. If the scattering occurs between two states of a single Dirac cone (either $K \rightarrow K$ or $K' \rightarrow K'$), it is referred to as intravalley scattering, whereas if it involves states from two neighboring cones (either $K \rightarrow K'$ or $K' \rightarrow K$) it is called intervalley scattering [cf. blue arrows in Fig. 5.15(a)]. Not always are both types of scattering possible. Due to the pseudospin degree of freedom [cf. red arrows in Fig. 5.15(a)] and its conservation which holds for Dirac electrons [25, 27], a strong scatterer is needed in order to flip the pseudospin and enable intravalley scattering. Pseudospin can be thought of as an additional degree of freedom which can be parallel (at K points) or anti-parallel (at K' points) to the momentum of the electrons (when momentum is referenced to the corresponding K and K' points). Fourier transforms of STM and STS images are suitable methods for the observation of such processes.

We performed STM and STS measurements of 1 ML graphene intercalated with ~ 1 ML of Cs [so that (2×2) and $(\sqrt{3} \times \sqrt{3})$ R30° structures were present on the sample, see Section 5.1 for details]. In order to observe scattering patterns, areas on the sample

containing defect i.e. imperfection in graphene lattice (grain boundary, adsorbate, substrate surface impurity etc.) had to be measured. In the first row of Fig. 5.16 several such areas on the sample are shown imaged in atomic resolution. In panels (a) and (g) a moiré structure is also visible. Panels (c) and (e) show the same area of the sample recorded in STM and dI_t/dV_t spectroscopic mode respectively, at a bias voltage of 100 mV. In both of those panels an additional oscillatory structure is visible (although more pronounced in STS image) in the form of concentric rings spreading out from the defect. In order to investigate these and other not so obvious patterns hidden in STM/STS images, Fourier transforms of the images were calculated and they are shown in lower panels of Fig. 5.16. Besides spots corresponding to the periodicity of carbon atoms in graphene (magenta circles), additional features in the form of contours can be observed. They are centered either at the Γ points (i.e. at 0th and 1st order carbon spots) or the K and K' points of the graphene BZ. These contours are a signature of quasiparticle scattering processes occurring in the graphene. Intravalley scattering is recognized as quasi-circular patterns centered at the Γ points (red arrows in Fig. 5.16). As can be inferred from Fig. 5.15(a), such patterns can be constructed if all allowed q_1 vectors are drawn in the reciprocal space. Also, it is easily concluded that the radius of the patterns will be twice as large as the radius of the real Fermi contour [164]. In a similar manner, intervalley scattering (yellow arrows in Fig. 5.16) is characterized by the contours located at the corners of the BZ. Again, those patterns can be constructed by plotting all allowed vectors q_2 indicated in Fig. 5.15(a) and their linear size will be a factor two larger than the size of the real Fermi contour. It is interesting to notice that intervalley scattering will reproduce the exact shape of the Fermi contour [164], only four times larger in area (factor of two in one dimension increases to $2^2 = 4$ in the case of an area). For visual comparison, theoretical calculations of the scattering patterns in freestanding graphene and graphite can be found in Refs. [165, 166].

Similar scattering contours have been reported earlier. Quasiparticle scattering in graphene on SiC(0001) has been investigated both experimentally and theoretically [162, 163]. Several studies report on FT-STM evidence of scattering found in HOPG [167, 168]. Intervalley scattering has also been observed for graphene on metal (111) surfaces of Pt, Cu and Au [169, 170]. It should be emphasized that in all those systems top-most graphene layer is neutral or just slightly doped i.e. the Dirac point is not far from

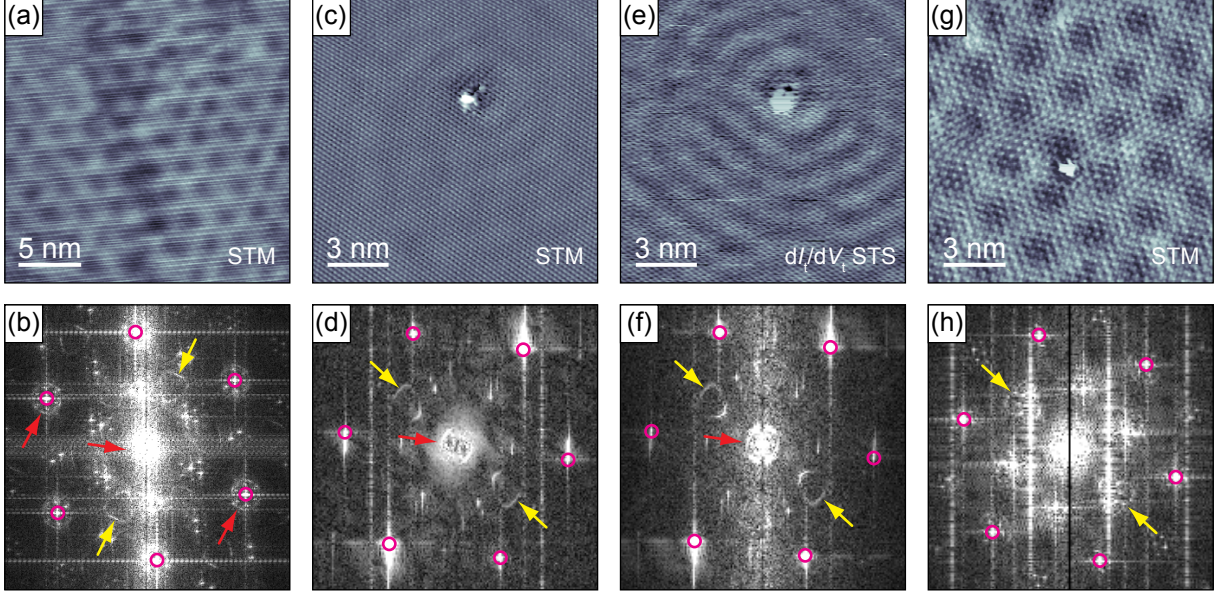


Figure 5.16: STM images [(a), (c) and (g)], dI_t/dV_t map (e) and their corresponding Fourier transforms [(b), (d), (f) and (h)] of Cs intercalated Gr/Ir(111). All images in the top row contain defects which causes electron scattering. Fourier transforms display intravalley (red arrows) and intervalley scattering (yellow arrows). To guide the eye, magenta circles indicate first order spots originating from the graphene periodicity. (a) $U_t = 40$ mV, $I_t = 300$ pA, (c) $U_t = 100$ mV, $I_t = 300$ pA, (e) $U_t = 100$ mV, $I_t = 300$ pA, (g) $U_t = 20$ mV, $I_t = 300$ pA. $T_S = 6$ K in all images.

the Fermi level. In our case of Gr/Cs/Ir(111), the Dirac point is shifted to 1.13 or 1.2 eV below the Fermi level because of caesium n -doping (see Section 5.2) with the dispersion relation outside the linear and isotropic regime where the electrons cannot be treated as massless Dirac quasiparticles any more. Due to this deviation from the Dirac regime, pseudospin is not a good quantum number and intravalley scattering is enabled even for the weak scatterer. That is why the observation of scattering patterns is greatly facilitated in the intercalated, highly doped graphene systems. Also, decoupling of graphene from the iridium via intercalation eases the formation of standing waves which constitute scattering patterns in the inverse space. Effective graphene decoupling is a crucial factor for quasiparticle scattering in e.g. O-intercalated system (see Ref. [171] and Section 6.3 for details).

As mentioned in the previous paragraph, the shape of intervalley scattering patterns is identical to the shape of the real Fermi contours and their area differs by a factor of four. Knowing this, one can exploit the patterns to calculate the charge transfer to graphene following the Eq. 1.2. In Fig. 5.15(b) we show a zoom-in on one such scattering pattern taken from FT-STM map displayed in Fig. 5.16(b). To estimate an area within

the pattern, we hand-fitted the 36-sided polygon to the data. The resulting polygon (contour) is represented by white dotted line in Fig. 5.15(b). From its area and Eq. 1.2, it follows that the charge transfer to graphene equals to $1.07 \times 10^{14} \text{ cm}^{-2}$. We see that this value is in excellent agreement with the charge transfer of $1 \times 10^{14} \text{ cm}^{-2}$ obtained from ARPES (cf. Section 5.2). Indeed, scattering of quasiparticles can be used for indirect determination of charge transfer to graphene.

As it is demonstrated in Fig. 5.16(e) and (f), scattering patterns can also be noted in the Fourier transforms of spectroscopic maps. By performing a series of such measurements at different tunneling voltages, scattering patterns at different energies can be obtained which can serve for extraction of the dispersion relation of quasiparticles in graphene. This procedure was performed for the determination of dispersion relation of monolayer and bilayer graphene on SiC(0001) in the work of Mallet et al. [163]. In such experiments, care has to be taken so that STS maps are recorded with high enough energy and space resolution as well as sufficient scan size so that the Fourier transformation can provide results of satisfying quality [163].

5.9 Properties of ionic adsorption

From Section 5.2 it follows that the adsorption of small amounts of Cs onto graphene leads to notable shifts of the Fermi level because of the marginal starting DOS of graphene at the Dirac point. Indeed, it was shown that adsorbates in general cause doping and thus a shift of the Fermi level within graphene [77, 172, 173]. Furthermore, shifting of the Fermi level by e.g. external gating can influence the adsorption properties of graphene. This was demonstrated in the case of gate voltage dependent ionization state of Co atoms adsorbed on graphene [174] and gate-controlled adsorption rate of molecular O on graphene [175]. Additionally, theoretical calculations confirmed that binding strength between adsorbed H atoms and graphene depend on the doping level of graphene [176]. Therefore we see that the position of the Fermi level is closely related to the adsorption properties of graphene. Since we know that the modification of the chemical potential within graphene is easily achieved by intercalation, it is interesting to see what is the relation between adsorption and intercalation in epitaxial graphene. In this section, we use Cs adsorption and intercalation to study this relation. In order to prove the universality of our findings

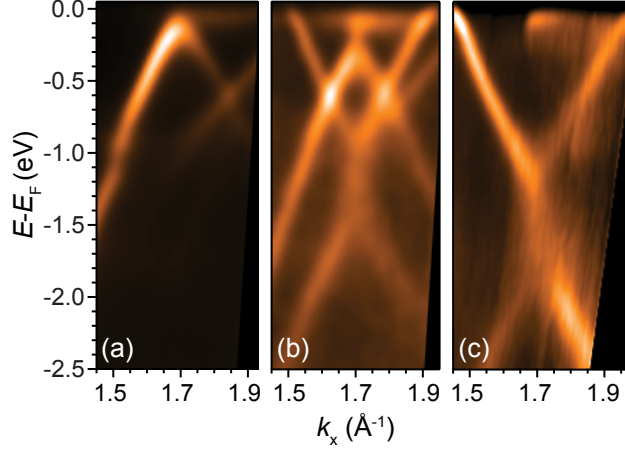


Figure 5.17: ARPES spectra of (a) pristine Gr/Ir(111) ($E_D = 0.1$ eV), (b) 0.3 ML Cs ($E_{D,\alpha} = -0.12$ eV, $E_{D,\gamma} = -1.13$ eV) and (c) 0.92 ML Eu ($E_D = -1.38$ eV) samples. In (a): Elt-ARPES, $\parallel \Gamma K$, $\hbar\omega = 40.5$ eV, s -polarization, $T_S = 300$ K. In (b): Elt-ARPES, $\parallel \Gamma K$, $\hbar\omega = 40.5$ eV, p -polarization, $T_S = 300$ K. In (c): Zg-ARPES, $\parallel \Gamma K$, $\hbar\omega = 21.2$ eV, mixed polarization, $T_S = 200$ K.

and applicability to other ionic adsorbates, relevant Eu intercalation data is also presented and discussed (additional data on Eu intercalation is given in Section 6.2).

5.9.1 Relating work function and Dirac point position

The knowledge of exact value of the sample work function is often important from physical but also experimental point of view. In the following we try to combine STM and ARPES results in order to relate the value of the work function of Gr/Ir(111) and the position of the graphene Dirac point. One of the main conclusions of Ref. [177] suggests of the difference between the work function of graphene doped by a metal substrate (Φ_M) and the corresponding shift of the Dirac point with the respect to the Fermi level (E_D) is approximately constant and equal to the value of the work function of freestanding graphene (Φ_{FS}): $\Phi_M - E_D \approx const. = \Phi_{FS}$. This means that the difference between the work functions of various areas on the sample is equal to the difference in their Dirac point positions i.e. $\Delta\Phi = \Delta E_D$. In Fig. 5.17(a) and (b) we show the ARPES spectra of pristine and 0.3 ML Cs intercalated graphene, respectively. Knowing the positions of the Dirac points, one could anticipate that the work function difference between the α - and γ -phase is roughly -0.12 eV $- (-1.13)$ eV = 1.01 eV.

We try to reconstruct this value by performing $I_t(z)$ measurement with STM. Several pairs of sites are chosen on the sample: one from the α -phase and another from the γ -phase

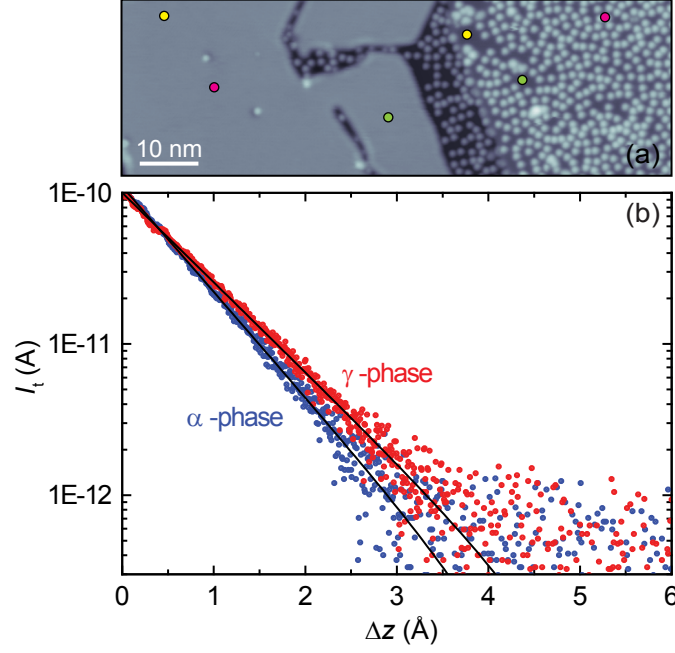


Figure 5.18: (a) STM image showing phase separation of partially Cs-intercalated graphene ($U_t = 1$ V, $I_t = 10$ pA). (b) $I_t(z)$ data recorded at the positions of yellow dots in (a). Tunneling voltage in all $I_t(z)$ measurements was 1.5 V.

[see colored dots in Fig. 5.18(a)]. For the case of yellow dots, the resulting $I_t(z)$ data is shown in Fig. 5.18(b). By performing simple analysis based on the Eq. 2.4 and 2.5 [109], we obtain $\Delta\Phi = \Phi_\alpha - \Phi_\gamma = 1.34$ eV which is somewhat larger than the value determined from ARPES. But the expected $\Delta\Phi$ between the γ -phase and pristine graphene is 0.1 eV $- (-1.13)$ eV = 1.23 eV which is in better agreement with $I_t(z)$ measurements. Since yellow dot in the α -phase was chosen to be in a small clearing between the adatoms, this means that locally graphene resembles to the pristine graphene rather than to slightly n -doped α -phase graphene. In addition, different $\Delta\Phi$ values were obtained for other pairs of $I_t(z)$ sites: 0.28 eV and 0.13 eV [green and magenta dots in Fig. 5.18(a)]. We conclude that the actual difference in the work function is locally inhomogeneous and greatly depends on the exact location of the $I_t(z)$ measurement within the α -phase which is a consequence of positive charge of Cs adatoms and associated localized charge transfer to graphene. Despite work function difference inhomogeneity, the relation $\Phi_\alpha > \Phi_\gamma$ was always found to be true. ARPES measurements are insensitive to the work function variations and are governed by the average work function [30, 134]. It should be noted that $I_t(z)$ measurement in the γ -phase channels are misleading and they yield lower work function than their surroundings. We assume that this is an effect of narrowness of the channels which causes higher tunneling current [and slower decay of the $I_t(z)$ curve] due

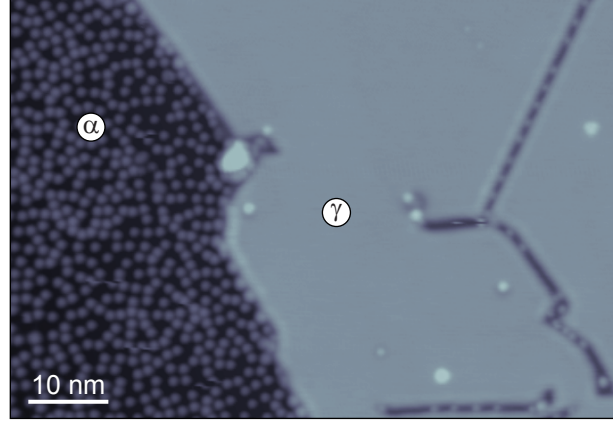


Figure 5.19: STM image of partially intercalated graphene with clear separation to the α - and γ -phase. Virtually all Cs adatoms are adsorbed to the non-intercalated areas—the α -phase or thin channels in the γ -phase. $U_t = 1$ V, $I_t = 10$ pA.

to the tunneling to the sides of the STM tip.

In Fig. 5.17(c) we show photoemission spectra of Eu intercalated graphene where Eu layer exhibits (2×2) structure with respect to the graphene lattice. The Dirac point is located at -1.38 eV which would yield a difference in work function with respect to pristine graphene of $\Delta\Phi = \Delta E_D = 0.1$ eV $- (-1.38)$ eV = 1.48 eV. Indeed, in Ref. [86] it is shown via $I_t(z)$ spectroscopy that $\Delta\Phi = \Phi_{\text{Gr/Ir}} - \Phi_{\text{Gr/Eu/Ir}} = 1.5$ eV which is in excellent agreement with the ARPES data. From these findings and from the ones stated in the previous paragraph we infer that the relation $\Delta\Phi \approx \Delta E_D$ holds and that the intercalated areas exhibit lower work function as compared to the non-intercalated ones. A more detailed analysis of the electronic structure of the Eu-intercalated graphene will be given in Section 6.2.

5.9.2 Three-step adsorption model

One of the main effects of intercalation of various species under the graphene is the charge transfer to or from graphene. Knowing that charge transfer effectively changes graphene band structure and that adsorption of atoms and molecules involves electron delocalization within graphene, one could ask what is the influence of intercalation on adsorption processes in epitaxial graphene systems. In Fig. 5.19 we show an area of partially Cs intercalated graphene with sharp boundary between the α - and γ -phase. Virtually all Cs adatoms are adsorbed on Gr/Ir(111) and not on top of the γ -phase, indicating a preference in adsorption to non-intercalated areas. The same conclusion can be drawn when

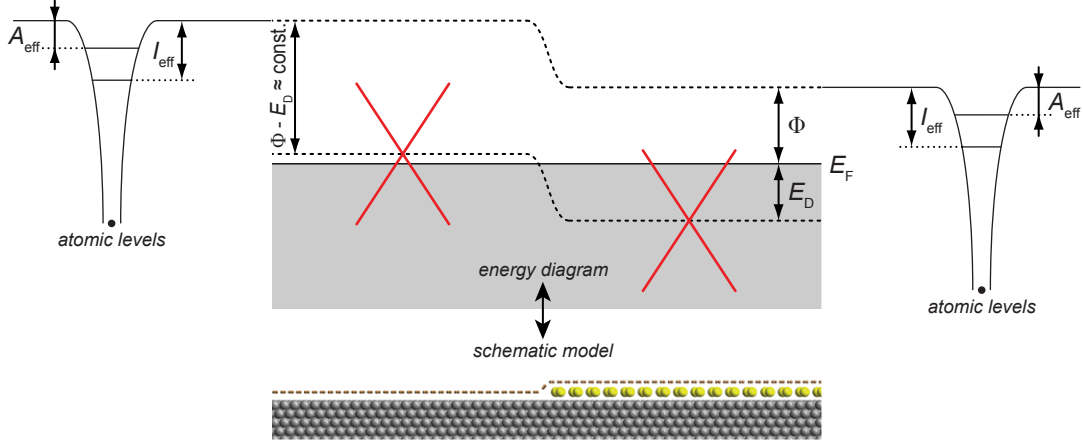


Figure 5.20: A schematic model of partially intercalated graphene on a metal substrate with the corresponding energy diagram, including the relevant atomic levels of the atom which will be adsorbed (effective ionization and affinity energies, I_{eff} and A_{eff}). The intercalated area of the sample is characterized by n -doping of graphene i.e. a shift of the Dirac cone (red lines) to higher binding energies and the corresponding work function decrease ($\Delta\Phi = \Delta E_D$), which yields a preference of adsorption on non-intercalated areas. Based on the figure from Ref. [178].

looking at Fig. 5.2. Moreover, in Fig. 5.19 several channels (described in Section 5.1) in the γ -phase are visible which contain a sequence of Cs atoms. Evidently, adsorbed Cs atoms are only found in the channel, not in its surroundings. This is an additional proof of higher adsorption energy in the non-intercalated graphene areas. Similarly, it was found that Eu atoms prefer to adsorb to the non-intercalated graphene areas where they form clusters [178]. Together with the relation $\Delta\Phi = \Delta E_D$ we conclude that the adatoms prefer to adsorb to the areas of higher work function.

In order to explain this phenomenon, in Fig. 5.20 we give a schematic model and the corresponding energy diagram of partially intercalated graphene together with the energy diagram of the atom which is about to be adsorbed. The energy diagram of an adatom is given for the case when it is sufficiently far from the substrate so that the overlap of the adatom and substrate wavefunctions is negligible. The relevant atomic energies in adsorption are effective ionization energy (I_{eff}) and effective affinity energy (A_{eff}) [179]. We focus on the situation of slightly p -doped non-intercalated and n -doped intercalated graphene (but the following discussion is analogous in other cases) and we assume that the adatom will donate electrons to the graphene. The later implies that $I_{\text{eff}} < \Phi$, while the electrons would be transferred from graphene to the adatom if $A_{\text{eff}} > \Phi$. Next, we depict the process of adsorption as a Gedankenexperiment and divide it into three steps, as described in Ref. [178]. In step (1) the atom which is about to be adsorbed is ionized.

To a good approximation the ionization energy is independent of the electronic structure of the substrate i.e. $I_{\text{eff}} \approx \text{const.}$ in left and right atomic energy scheme of Fig. 5.20. In step (2) the electron is delocalized within the substrate and gains energy identical to Φ . Hence, total energy gain is $\Phi - I_{\text{eff}}$ and more energy will be gained in this step if the work function of the substrate is larger. In the final step (3) the remaining positive ion is moved onto the substrate. We can again approximate that the energetics of this step is independent of the electronic structure of the substrate. Considering all three steps together, it is evident that only Φ determines the energy gain upon adsorption and this is in agreement with our experiments. Following this model, adsorption to the non-intercalated areas is preferred by [1.01, 1.23] eV in the case of Cs (depending on the α -phase concentration) and 1.48 eV in the case of Eu. This adsorption preference can be directly readout from the ARPES spectra.

Of course, the model presented here is an oversimplification of the real adsorption process. For example, the amount of energy an electron gains upon delocalization is actually less than Φ because the electron itself transfers charge to graphene and induces ΔE_D and $\Delta\Phi$. It was also assumed that moving the positive ion to the substrate does not depend on the substrate electronic structure. There, screening of the ion was neglected which becomes important as the LDOS at the Fermi level increases with increasing n -doping of graphene. Because of these approximations only qualitative (but not quantitative) agreement is found between our experiments and DFT results presented in Ref. [178]. Calculations show that the bond between adsorbing adatoms and the substrate is ionic and is characterized by donation of approximately one electron from the adatom to the substrate (for adsorption to both intercalated and non-intercalated areas), which is what we have assumed in our model. But the preference of binding to the non-intercalated areas was found to be less than the values determined from the experiment: 0.6 eV for Eu and 0.7 eV for Cs.

CHAPTER 6

Intercalation with other species

Results of Cs intercalation presented in the previous chapter have been used to gain knowledge on fundamental concepts important for intercalation of epitaxial graphene in general. Despite the applicability of those results to other similar intercalated systems, one should bare in mind that they are Cs-specific—that is, intercalation of other species will only to some extent be similar to Cs intercalation.

In this chapter we are studying several other intercalated systems of epitaxial Gr on Ir(111) formed by Li, Eu and O deposition. Li intercalation specificities as well as comparison with Cs intercalation are given which is especially interesting since Li and Cs are chemically very similar elements. In addition, Eu intercalation results are given where we focus on the electronic structure in the vicinity of the graphene K point. As will be shown, both Li and Eu atoms, once they are intercalated, have the ability to increase the binding energy of Ir surface states. Furtheron, we show our results on O intercalation, representing p -doped family of graphene intercalation compounds and which provide an irrefutable evidence of quantum confinement of Dirac electrons in graphene quantum dots.

6.1 Lithium intercalation

In Chapter 5 we studied Cs intercalation in great detail and found that van der Waals interaction plays crucial role in the transition from the adatom α - to the intercalated γ -phase of Cs atoms. To make our study more comprehensive, we also characterize the intercalation of Li, which is on the opposite side of the alkali metals group. Li deposition is carried out at room temperature on 1 ML graphene on Ir(111). In Fig. 6.1 we show several stages of Li intercalation as seen by ARPES. A continuous shift of the Dirac cone to higher binding energies due to the n -doping can be noted until a maximum

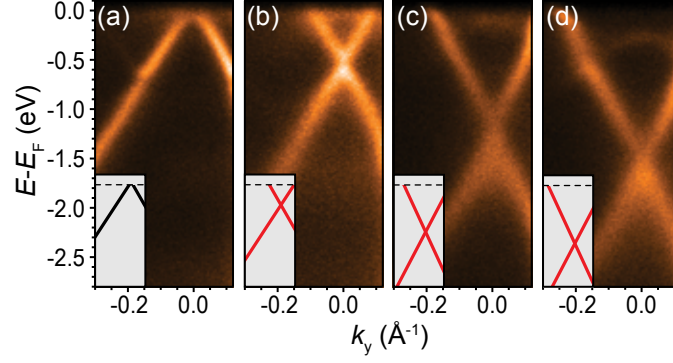


Figure 6.1: A sequence of four ARPES spectra showing the Dirac cone for different amounts of deposited Li. Only one Dirac cone is visible at any stage of Li deposition implying the absence of phase separation in this system. Insets schematically indicate the position of the Dirac cone. BNL-ARPES, $\perp \Gamma K$, $\hbar\omega = 22.7$ eV, p -polarization, $T_S = 300$ K.

Li concentration of (1×1) structure relative to Ir is formed. At any doping level, only one Dirac cone is visible. This means that there is no phase separation to the adatom and intercalated phases, as observed for Cs (cf. Fig. 5.7). We explain the absence of phase separation in the following way: Li atoms are small in size and hence they do not have to lift off graphene notably and pay much for delamination energy in order to form intercalated structures. Thereby, it can intercalate at any density with much smaller cost of graphene partial delamination.

Our idea is further supported by the results of the vdW-DFT calculations of Li intercalation [152]. It is found that the graphene-iridium separation is similar in both adatom and intercalated Li structures (see Table 6.1), meaning that the Li atom has to pay much lower cost for small (partial) graphene delamination as compared to more extensive (full) delamination that Cs atom has to pay (cf. Table 5.2). Taking also into account that Li ions are better screened close to the Ir surface, it is calculated that the intercalation is energetically more favorable both for the dense and the dilute Li structures. Because of very small partial delamination energy (i.e. the absence of significant relamination), a complete desorption of Li cannot be prevented. Indeed, after annealing fully intercalated sample up to 870 K, the Dirac cone identical to the one of clean graphene on Ir(111) is restored in ARPES.

Additional ARPES measurements of fully Li-intercalated sample were carried out in the ΓK geometry and are shown in Fig. 6.2. Again, n -doped Dirac cone is evident with the Dirac point located at ~ 1.6 eV below the Fermi level. As opposed to other

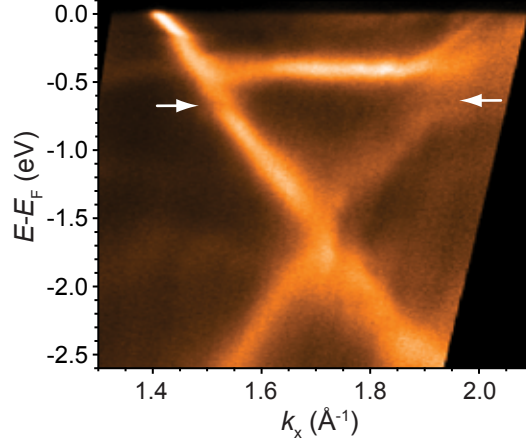


Figure 6.2: ARPES spectrum of fully intercalated Gr/Li/Ir(111) in the vicinity of the K point. Due to electron doping, the iridium surface state is shifted to higher binding energies, visible as a flat band at 0.4 eV below the E_F . Hybridization between π^* and iridium states is apparent in the form of anticrossing (white arrows). Zg-ARPES, $\parallel \Gamma K$, $\hbar\omega = 21.2$ eV, mixed polarization, $T_S = 300$ K.

alkali metals, Li intercalation yields one additional interesting feature—almost flat band located at 0.4 eV below the Fermi level. This band is identified as the iridium surface state which is located at the Fermi level for nearly neutral graphene (cf. Fig. 3.6) or for the graphene of more moderate doping level (cf. Fig. 5.6 and 5.17). Shifted iridium state can also be noted in Fig. 6.1(d) in the form of a faint, parabolic-like feature with downward dispersing curvature. From this we conclude that the overall 3D shape of the state is similar to a paraboloid with very large curvature in the direction parallel to ΓK . Iridium surface state does not shift immediately upon Li intercalation; at first, only the Dirac cone is shifted continuously to ~ 1.2 eV below E_F . Then, additional Li deposition yields simultaneous shifting of the Dirac cone and the iridium surface state in such way that their energetic separation remains constant. Obviously, only at some later point of the intercalation process it becomes affordable to transfer electrons both to graphene π^* orbitals and iridium surface state. It is unclear whether this kind of behavior is universal to all intercalated Gr/Ir(111) systems (and would be achievable if enough charge is supplied by the intercalated species) or is Li-specific. On one hand, preliminary DFT calculations

Table 6.1: Graphene-iridium separation for two Li concentrations in the adatom and the intercalated phase as calculated from DFT with the inclusion of the vdW interaction.

Li phase	(4×4)	(1×1)
adatoms	3.23 Å	3.00 Å
intercalated	4.24 Å	4.23 Å

[180] indicate that intercalated Li atoms are situated unusually close to the Ir surface which might result in an increased charge transfer to iridium surface states. On the other hand, similar effect is also found in Eu-intercalated graphene (see Section 6.2).

Having the iridium surface state away from E_F , it is easier to examine its influence on the electronic states of the Dirac cone. Closer inspection of Fig. 6.2 reveals that the two bands exhibit anticrossing at points where they meet (white arrows). In other words, a hybridization between the graphene π^* orbitals and the surface state of iridium is evident. This observation is in agreement with findings that these states hybridize even in the case of pristine Gr/Ir(111) [50]. We also note a strong electron-phonon coupling effect visible on the left branch of the cone, close to the Fermi level, which was studied before in several intercalated systems [87, 88, 181–183].

6.2 Europium intercalation

We already showed some ARPES data of the europium intercalated graphene in Section 5.9 in the context of work function change. Here we will focus on the very electronic structure in greater detail. Interest for the exploration of Eu intercalation stems from the large magnetic moment of $7 \mu_B$ per Eu atom and possible effects it may have on the electronic structure of graphene. We also note that both alkali and Eu atoms have s -orbitals as last filled orbitals with the difference in occupation number: one for alkalis and two for Eu. Because of this, comparison of intercalation effects is of interest. Similar as in the case of Cs, Eu deposition on epitaxial graphene exhibits a variety of structures in the surface-adsorbed or intercalated form. If Eu is deposited on the sample at room temperature, intercalation is inhibited and Eu islands and clusters are formed on top of graphene [86, 109]. If deposition temperature is increased to 720 K, then Eu atoms intercalate [86, 178] and form either (2×2) or $(\sqrt{3} \times \sqrt{3}) R30^\circ$ structure with respect to graphene, depending on the exact deposited amount. In a similar manner, two possible superstructures were observed for the Cs-intercalated system (cf. Section 5.1). The corresponding diffraction patterns we observed are shown in Fig. 6.3(a) and (b). Moiré spots are almost completely gone, indicating that the interaction between graphene and iridium is reduced.

Next, we examine the electronic structure in the vicinity of the K points for the two Eu

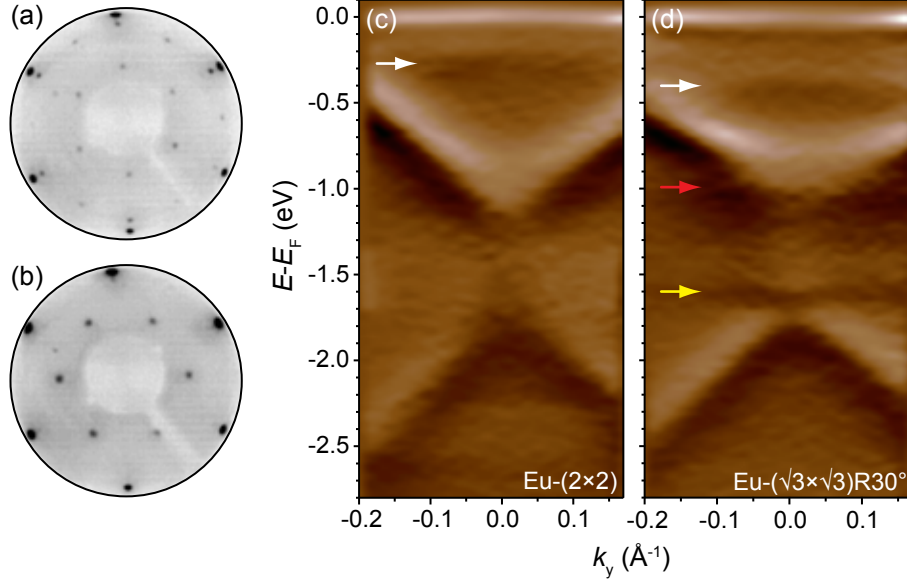


Figure 6.3: (a), (b) LEED patterns for Eu (2×2) and $(\sqrt{3} \times \sqrt{3})$ R30° structures, respectively ($E = 45$ and 49 eV). (c), (d) First derivative of ARPES spectra displaying the Dirac cone for the two intercalated Eu structures: (2×2) and $(\sqrt{3} \times \sqrt{3})$ R30°, respectively. In both structures, faint feature is visible at several hundred of meV below E_F (white arrows). In the case of $(\sqrt{3} \times \sqrt{3})$ R30° structure, additional bands are perceived at higher binding energies (red and yellow arrows). Zg-ARPES, \perp Γ K, $\hbar\omega = 21.2$ eV, mixed polarization, $T_S = 250$ K.

superstructures shown in Fig. 6.3(c) and (d). In both cases the Dirac cone exhibits strong n -doping due to the electron transfer from the Eu s - to graphene π -orbitals. By linear fits to the bands, we estimated the positions of the Dirac points to be $E_{D,(2 \times 2)} = -1.36$ eV and $E_{D,(\sqrt{3} \times \sqrt{3})\text{R30}^\circ} = -1.43$ eV. We see that for the denser $(\sqrt{3} \times \sqrt{3})$ R30° structure the charge transfer is larger, which is logical; the same observation has also been made for Cs-intercalated graphene (cf. Section 5.2). One of the motivational factors for studying Eu intercalation is, as already mentioned, large magnetic moment of Eu atoms which could induce spin-splitting of the Dirac cone. Such splitting is not observed in our ARPES data. One of the reasons for this could be too coarse resolution of our analyzer which prevents the observation of two separate spin-split cones. Or the influence of Eu atoms magnetic moments on graphene π -system is negligible and there is no spin splitting at all. In either case, spin-polarized ARPES measurements should be performed in order to gain more information on this issue.

In the photoemission spectra of both structures a faint band can be resolved at several hundred of meV below E_F [white arrows in Fig. 6.3 (c) and (d)]. This band is identified as the iridium surface state which is shifted to higher binding energies because of n -doping.

We observed the same effect in Li-intercalated graphene, as presented in the previous section [cf. Fig. 6.1(d) and 6.2]. For comparison, ARPES spectra of the Dirac cone recorded in the $\parallel \Gamma K$ geometry for the Eu- (2×2) intercalated structure is given in Fig. 5.17(c). When intercalated Eu atoms form $(\sqrt{3} \times \sqrt{3}) R30^\circ$ superstructure, additional features can be resolved in the ARPES spectra. Their position is noted in Fig. 6.3(d) by red (-1 eV) and yellow arrows (-1.6 eV). The origin of those two bands is, at a time of writing of this thesis, still not well understood. Both of them seem to hybridize, at least partially, with the graphene states in the vicinity of the Dirac point.

Based on our photoemission spectra, it is hard to estimate if a band gap exists at the Dirac points for the Eu-intercalated systems. One of the crucial factors limiting this is the band line-width in the ARPES spectra and we have performed MDC analysis in order to assess the quality of our data. From the original (non-derivative) data of Fig. 6.3 we obtained the following FWHMs at $E = E_F - 0.5$ eV: $(0.077 \pm 0.004) \text{ \AA}^{-1}$ for the (2×2) structure and $(0.071 \pm 0.005) \text{ \AA}^{-1}$ for the $(\sqrt{3} \times \sqrt{3}) R30^\circ$ structure. For comparison, the corresponding width of Cs $(\sqrt{3} \times \sqrt{3}) R30^\circ$ spectra from Fig. 5.7 is $(0.045 \pm 0.001) \text{ \AA}^{-1}$. So we see that Eu spectra line-widths are somewhat increased. There are several explanations for this: (i) enhanced electron-electron scattering due to the significant charge transfer from Eu atoms to the graphene, (ii) inhomogeneous intercalation which yields several slightly different doping levels which are averaged in our ARPES setup and (iii) intercalated Eu layer introduces small spin-splitting to the electronic structure of graphene and causes broadening. In addition, the aforementioned hybridization of the Eu bands and the Dirac cone additionally disturbs the assessment of the band gap existence and size for the $(\sqrt{3} \times \sqrt{3}) R30^\circ$ superstructure.

6.3 Oxygen intercalation

Graphene quantum dots can be used to induce quantum-size effects on the electronic states. In STS measurement of such structures, confinement effects are observed as discrete peaks in the LDOS and the respective spatial STS maps of confined states reveal standing wave patterns of scattered electrons or holes. There are several explanations of the origin of confined states found on graphene quantum dots on Ir(111) (see Section 1.5). The source of the problem is the similarity of energy and slope of the Dirac cone and

the iridium surface states at the Γ point (see Section 4.1 for their description). In this section, we provide the evidence which will unambiguously support the scenario of Dirac electrons confinement in quasi-freestanding graphene. In order to do so, we performed O intercalation experiments of nearly full layer of graphene on Ir(111). Such graphene coverage was achieved by performing six TPG cycles at 1420 K followed by a CVD step using ethylene pressure of 1×10^{-7} mbar for five minutes at 1120 K. In this way we obtained high photoemission intensity not just from the graphene but also from the iridium surface states because of low density of graphene step edges which are known to scatter iridium surface states (see Section 3.2 and Ref. [47]). To successfully intercalate oxygen at such high graphene coverage, high doses (5400 L, L = Langmuir) of molecular O_2 were applied in the UHV chamber at elevated temperatures (520 K).

6.3.1 Electronic structure

The electronic structure of pristine and O-intercalated sample in the ΓK direction is shown in Fig. 6.4. In panel (a) a characteristic linear dispersion of the Dirac cone can be seen, with the Dirac point located at 0.1 eV above the Fermi level [46]. In addition, an iridium surface state [46, 50] at the Fermi level is also visible. Panel (c) shows the Brillouin zone center where the spin-split iridium surface states are found (see Section 4.1 and references therein for more information). After O intercalation, the Dirac point is shifted up in energy because the electrons are transferred from graphene π -orbitals to other available states of the system [Fig. 6.4(b)]. Later on, we will discuss on the details of charge rearrangement. Also, the photoemission intensity corresponding to iridium surface state in panel (a) is not visible in panel (b). The same observation is made for the surface states at the Γ point—upon O intercalation, spin-split states are completely suppressed [cf. Fig. 6.4(c) and (d)]. The intensity of the bulk band centered at 1 eV below the Fermi energy is slightly reduced, but remains clearly visible. Evidently, the presence of intercalated O layer quenches the surface states of iridium.

In order to quantitatively describe the Dirac cone after O intercalation, we also record ARPES data in the ΓK geometry which, in Zg-ARPES, enables more detailed k -space mapping in the k_x direction. Graphene is formed by $6 \times$ TPG only because (i) it yields high enough graphene coverage to obtain satisfactory photoemission intensity, (ii) oxygen intercalation is more efficient since there is more uncovered iridium surface available for

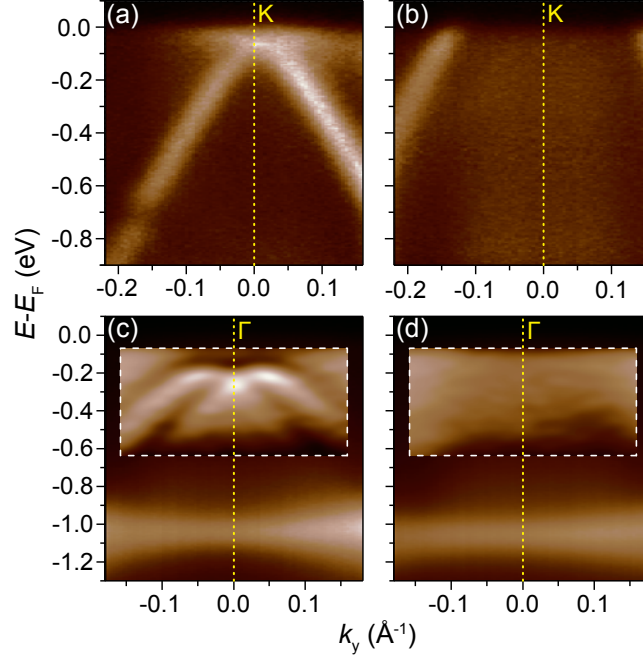


Figure 6.4: ARPES spectra of Gr/Ir(111) sample prior to (left panels) and after O intercalation (right panels). (a) and (b) show the electronic structure in the vicinity of the K point, (c) and (d) in the vicinity of the Γ point. Dashed rectangles in (c) and (d) show first derivative of the raw photoemission data in order to optimize the visibility of the surface states. Zg-ARPES, $\perp \Gamma K$, $\hbar\omega = 21.2$ eV, mixed polarization, $T_S = 150$ K.

oxygen dissociation preceding the intercalation [69] and (iii) we are not concerned by the effects of the graphene flake edges. The resulting spectrum is shown in Fig. 6.5(a). The MDC analysis on the left branch of the cone in the energy range between -0.2 and -1 eV is performed since in this range a reliable fit is possible (avoiding the electron-phonon kink close to the E_F and variations in the band intensity below -1 eV). By fitting the resulting Lorentzian peak centers to linear function $E(k)$, we obtained the position of the Dirac point $E_D = (0.68 \pm 0.05)$ eV and the band velocity $v_F = (1.03 \pm 0.01) \times 10^6$ m/s. The Dirac point position is in good agreement with other results [90] while the band velocity is almost identical to pristine Gr/Ir(111) values [47].

The structure of the intercalated O layer is (2×1) with respect to Ir(111) as reported earlier [69] which is in agreement with our diffraction pattern shown in Fig. 6.5(b). We can also notice that the moiré spots are almost completely gone which suggests that the interaction between graphene and iridium is reduced to even lower level as compared to non-intercalated graphene.

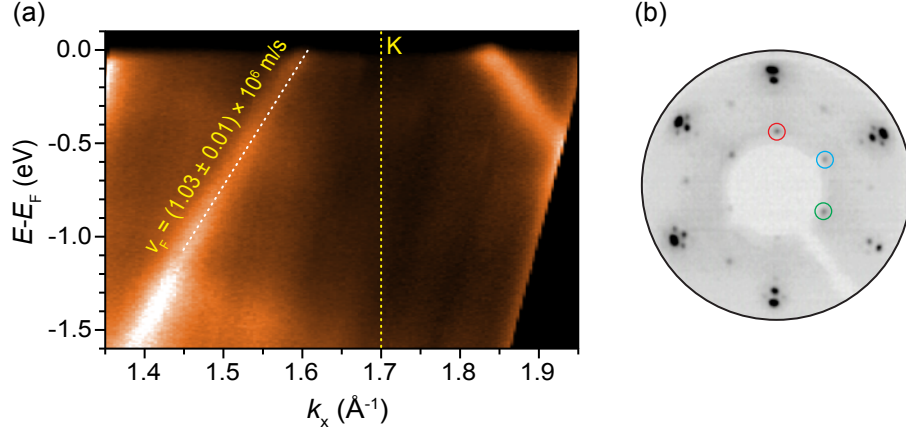


Figure 6.5: (a) ARPES spectra of Gr/O/Ir(111) at the K point. Dashed line indicates a linear fit to the positions of the Lorentzian lineshapes fitted to the MDC curves. Zg-ARPES, $\parallel \Gamma K$, $\hbar\omega = 21.2$ eV, mixed polarization, $T_S = 70$ K. (b) LEED diffraction pattern of Gr/O/Ir(111). O layer exhibits (2×1) structure with respect to iridium which, when all three possible rotations are present on the sample (red, blue and green circles), exhibits a diffraction pattern resembling to a (2×2) structure. The moiré satellite spots are heavily suppressed. $E = 60$ eV.

6.3.2 Confined Dirac electrons and graphene decoupling

In Ref. [171] confined electronic states found on graphene quantum dots intercalated by oxygen are studied. From the combination of STS mapping and a simplistic model of infinite potential cylindrical well used for wavevector determination, a discrete $E(k)$ relation of observed electronic states is derived. We have shown in the preceding subsection that O intercalation undoubtedly destroys the surface states of iridium, meaning that the electronic states observed by STS must be confined Dirac electrons. Moreover, from spectroscopic measurements shown in Ref. [171] it is found that $v_F = (0.96 \pm 0.07) \times 10^6$ m/s and $E_D = (0.64 \pm 0.07)$ eV, which is in excellent agreement with the values obtained from ARPES spectra of the Dirac cone from Fig. 6.5(a).

Based on the reduction of moiré spots intensity in LEED upon O intercalation [cf. Fig. 6.5(b)] we infer that Gr-Ir interaction is reduced which is expected because of increased Gr-Ir distance due to the insertion of O layer in between. This kind of effective decoupling of graphene has several additional consequences [171]. First of them is an observation of pronounced dip in the density of states (via point STS) of Gr/O/Ir(111) quantum dot located at approximately 0.6 eV which is related to the shift of the p -doped Dirac cone. An analogue dip has never been observed for non-intercalated Gr/Ir(111) areas because of the dominant contributions to the STS spectrum from the nearby iridium states, especially

when one considers a large parallel momentum transfer which is required for tunneling from the K-point of the graphene [184]. Second effect of graphene decoupling is intervalley scattering observed only in O-intercalated areas. As shown in Section 5.8, the scattering manifests itself through scattering patterns which are visible in Fourier transforms of the STS maps. We speculate that the scatterers are the edges of the graphene quantum dots. In accordance with our elaboration from Section 5.8, the shape i.e. diameter of the pattern agrees well with our ARPES data.

The validity of our experimental results is additionally corroborated by DFT calculations presented in Ref. [171]. It is calculated that the average Gr-Ir distance increases from 3.41 to 4.23 Å after O intercalation and that graphene corrugation drops from 0.35 to 0.19 Å. In addition, position of the Dirac point is found to be $E_D = 0.55$ eV which agrees well with our ARPES result. Noted shift of the Dirac point is related to the charge transfer from graphene π -orbitals into the O/Ir(111) interface states. Charge rearrangement is such that no charge accumulation occurs between C and O or Ir atoms which suggests that chemical bonds are not formed between them. The absence of such chemical bonding as well as induced structural changes clearly indicate that O intercalation causes effective decoupling of graphene from the iridium.

In this section we presented evidence confirming that the observed confined states on O-intercalated graphene quantum dots on Ir(111) are Dirac electrons. This finding is in agreement with several previous studies [70–72] and also excludes the possibility of assignment of those states to the surface states of Ir as was suggested in Ref. [73]. Recent STS study of graphene on Au(111) [185], however, does show that it is possible to recognize surface states of the substrate on graphene flakes in the form of quasiparticle scattering patterns. Simultaneously, scattering patterns corresponding to the Dirac electrons are identified. Therefore, the origin of the electronic states found on graphene islands synthesized on metal surfaces has to be interpreted with great care.

CHAPTER 7

Conclusion

A series of TPG growth cycles of graphene on Ir(111) was monitored by STM and LEEM. It results in the initial formation of small graphene islands, having typical size of the order of 10 nm, and the overall exponential increase of graphene coverage. A fraction of bare iridium surface covered by graphene after each TPG cycle is 19 and 15%, as determined by STM and LEEM, respectively. Due to the instrumental resolution, LEEM results should be taken as a lower limit. In addition, the photoemission intensity of the Dirac cone and of the Ir(111) surface state at the K point has been monitored during the TPG growth of graphene. The Ir(111) surface state ARPES intensity drops significantly for a full layer of graphene, which cannot be explained by intensity attenuation due to increasing graphene coverage only. Possible reasons for this finding are the specific interaction of the Ir surface state and graphene states at the Dirac point and the upward energy shift of the Ir surface state upon graphene formation. Furthermore, the intensity of the surface state decays faster than the graphene coverage grows. This indicates an additional quenching mechanism, which can be found in the scattering from strongly bound graphene edges. The increase of the Dirac cone intensity is in agreement with the increase of the graphene area deduced by STM. Also, by conducting 2PPE experiments for a series of TPG cycles, the average work function of Gr/Ir(111) was measured and it is found that it decreases linearly from 5.79 eV for bare iridium to 4.65 eV for 1 ML graphene sample.

A network of interconnecting wrinkles on a full graphene layer has been studied by *in-situ* LEEM. For R0 graphene, the network exhibits quasi-hexagonal ordering with wrinkles extending in three preferential directions. The three directions coincide with the three directions of dense-packed atomic rows of the Ir(111) surface indicating a close connection

between graphene wrinkling and iridium lattice contraction during sample cooldown. In contrast, hexagonal ordering is absent in R30 graphene and only two dominant directions of wrinkle extension are found, one of which is defined by the Ir surface steps. This observation is explained by weaker binding of R30 graphene to Ir(111) as compared to R0 graphene. It is also found that the wrinkles network can be approximated by a Voronoi diagram which greatly facilitates its description and parametrization.

From re-heating experiments of 1 ML graphene samples, we investigated disappearance and reappearance wrinkles in real time. Wrinkle formation is accompanied by an increase of LEEM reflectivity in its immediate vicinity. We propose that the reason for this is localized stress relaxation where the graphene lattice is relaxed only close to wrinkles and yields an increase in the diffraction intensity contributing to LEEM image formation. Moreover, structural features of graphene or iridium can act as nucleation sites for wrinkle formation and because of that the wrinkling process is only partially random.

Various segments of individual wrinkles and wrinkle crossings were investigated by room temperature STM. Presumably due to the interplay between van der Waals interaction and elastic energy, wrinkle profiles exhibit complex multi-folded structure exceeding simple semi-circular shape. The exact wrinkle shape depends on the details of the sample preparation procedure. Wrinkles crossings display highly crumpled and inhomogeneous structure, most probably consisting of various defects. These defects are crucial for the intercalation since they facilitate the penetration of atoms through the graphene sheet.

Electronic structure of Gr/Ir(111) at the Γ point was characterized by ARPES and 2PPE. Rashba-split surface states are found below the Fermi level, persisting on graphene-covered (111) surface of iridium. They are of p -character in the vicinity of the Γ point and hence can be described by the nearly-free electron model. The Rashba parameter of the states, calculated by fitting the two spin-split bands by parabolas, is 1.89 eV Å. In our 2PPE experiments, we observed three IPSs for various graphene coverages that are situated just below the vacuum level and can be described by a Rydberg series of parabolic electronic states with an effective mass equal to free-electron mass. There is no indication of a second prominent series of IPSs as predicted for freestanding graphene. The reason for this can be found in the impaired mirror symmetry of graphene due to the presence of the Ir substrate. By tuning the photon energy, we were able to identify the spin-split surface states of Ir as pump states for the 2PPE process. This is additionally

strengthened by the observation of a resonant transitions to IPSs at specific k_{\parallel} values. In addition, we found that electrons occupying IPSs are localized on graphene islands due to the large work function difference between clean Ir and Gr/Ir(111) areas.

Presented Cs intercalation results are important for understanding of the intercalation mechanism in epitaxial graphene and also in other layered systems where van der Waals interaction dictates interlayer binding. It is revealed that the Cs intercalation is preceded by the formation of a dilute adatom phase on top of graphene. Only when the critical adatom concentration is reached and the Coulomb repulsion between them is large enough to overcome the cost of graphene delamination, intercalated Cs phase begins to form. Therefore, intercalation is governed by a fine interplay between the Coulomb and van der Waals interactions. Evidence of phase separation is found in LEEM, STM, ARPES and also theoretical calculations. The overall dynamics of intercalation is governed by graphene wrinkles and, after the penetration of Cs atoms through the graphene sheet, iridium steps. The importance of the van der Waals interaction is additionally supported by desorption experiments where pockets of intercalated Cs remain stable at high temperatures due to the partial relamination of graphene to iridium.

On Cs-intercalated areas of graphene, signatures of quasiparticle scattering were readily identified in Fourier transforms of STM and STS images due to the phase-space availability increase emerging from graphene n -doping. By analyzing the intervalley scattering contours, graphene doping was calculated and it is in excellent agreement with our ARPES results. Electron doping also influences the properties of ionic adsorption on graphene. Modification of the work function associated with the charge transfer defines preference in adsorption to non-intercalated areas of graphene, as was deduced by our combined STM and ARPES study of Cs and Eu intercalation.

We also characterized intercalation of several other atoms: Li, Eu and O. During deposition on Gr/Ir(111), Li atoms intercalate immediately which in turn results in the absence of phase separation as was found in the case of Cs intercalation. This is ascribed to small dimensions of Li atoms which do not have to delaminate graphene significantly in order to intercalate. At higher concentrations of intercalated Li charge is transferred to Ir surface state, shifting it to higher binding energies. Shift of the Ir surface state has also been observed in Eu intercalated systems, which in addition display bands originating from the intercalated Eu layer. By performing O intercalation, we effectively destroyed the

surface states of Ir and unambiguously proved that it is possible to confine Dirac electrons in graphene quantum dots. In addition, O-intercalated graphene is quasi-freestanding as can be deduced from spectroscopic measurements.

Appendix A

Tight binding approximation of graphene: dispersion relation, DOS and charge transfer

Very good description of graphene valence and conduction band can be achieved within the tight-binding approximation. Moreover, only the first nearest neighbors (1NN) have to be considered in order to obtain excellent agreement with the experimentally observed graphene dispersion. Here, we follow the derivation of graphene TB 1NN band structure as given in Ref. [186]. In the notation of the first quantization, Bloch functions are given by

$$\Phi_j(\mathbf{k}, \mathbf{r}) = \frac{1}{\sqrt{N}} \sum_{\mathbf{R}}^N e^{i\mathbf{k}\mathbf{R}} \varphi_j(\mathbf{r} - \mathbf{R}) \quad (\text{A.1})$$

where φ_j is the atomic wavefunction in the state j and the sum goes over all lattice points at positions \mathbf{R} . Graphene eigenfunction, $\psi_j(\mathbf{k}, \mathbf{r})$, is then given by the linear combination of the Bloch functions $\Phi_{j'}(\mathbf{k}, \mathbf{r})$

$$\psi_j(\mathbf{k}, \mathbf{r}) = \sum_{j'=1}^2 C_{jj'}(\mathbf{k}) \Phi_{j'}(\mathbf{k}, \mathbf{r}) \quad (\text{A.2})$$

where the summation goes to 2 (because of the two-atom basis of graphene) and $C_{jj'}$ are (at the moment) unknown coefficients. The energy of a certain state i is then given by

$$E_i(\mathbf{k}) = \frac{\langle \psi_i | \mathcal{H} | \psi_i \rangle}{\langle \psi_i | \psi_i \rangle} = \frac{\sum_{jj'=1}^2 \mathcal{H}_{jj'}(\mathbf{k}) C_{ij}^* C_{ij'}}{\sum_{jj'=1}^2 \mathcal{S}_{jj'}(\mathbf{k}) C_{ij}^* C_{ij'}} \quad (\text{A.3})$$

where we have used the abbreviations $\mathcal{H}_{jj'}(\mathbf{k}) = \langle \Phi_j | \mathcal{H} | \Phi_{j'} \rangle$ for the transfer integral and $\mathcal{S}_{jj'}(\mathbf{k}) = \langle \Phi_j | \Phi_{j'} \rangle$ for the overlap integral matrix elements. In order to find the energy $E_i(\mathbf{k})$, Eq. A.3 has to be minimized with respect to C_{ij}^* $\left(\frac{\partial E_i(\mathbf{k})}{\partial C_{ij}^*} = 0 \right)$. Then, if non-zero wavefunctions are sought (i.e. if C -coefficients are $\neq 0$), a secular equation conditioning this is obtained

$$\det [\mathcal{H} - E\mathcal{S}] = 0. \quad (\text{A.4})$$

So, in order to obtain the valence and conduction band energies as a function of wavevector \mathbf{k} , we must first find all matrix elements of \mathcal{H} and \mathcal{S} . Taking into account the labeling of the two graphene sublattices as A and B, the matrix elements are

$$\begin{aligned} \mathcal{H}_{AA}(\mathbf{k}) &= \langle \Phi_A | \mathcal{H} | \Phi_A \rangle = \frac{1}{N} \sum_{\mathbf{R}, \mathbf{R}'} e^{i\mathbf{k}(\mathbf{R}-\mathbf{R}')} \langle \varphi_A(\mathbf{r}-\mathbf{R}') | \mathcal{H} | \varphi_A(\mathbf{r}-\mathbf{R}) \rangle \\ &= \frac{1}{N} \sum_{\mathbf{R}=\mathbf{R}'}^N \epsilon + \mathcal{O}(\mathbf{R} \neq \mathbf{R}') \approx \epsilon \\ \mathcal{H}_{BB}(\mathbf{k}) &= \mathcal{H}_{AA}(\mathbf{k}) \approx \epsilon \end{aligned} \quad (\text{A.5})$$

where consider only contributions from the orbitals located at the same lattice sites which give the orbital energy of the $2p_z$ level, ϵ . Furthermore,

$$\begin{aligned} \mathcal{H}_{AB} &= \langle \Phi_A | \mathcal{H} | \Phi_B \rangle = \frac{1}{N} \sum_{\mathbf{R}, \mathbf{R}'} e^{i\mathbf{k}(\mathbf{R}-\mathbf{R}')} \langle \varphi_A(\mathbf{r}-\mathbf{R}') | \mathcal{H} | \varphi_B(\mathbf{r}-\mathbf{R}) \rangle \\ &= \frac{1}{N} \sum_{\mathbf{R}, \mathbf{R}'=1\text{NN}}^N e^{i\mathbf{k}(\mathbf{R}-\mathbf{R}')} (-\gamma_0) + \mathcal{O}(\mathbf{R}' \neq 1\text{NN}) \\ &\approx -\gamma_0 (1 + e^{-i\mathbf{k}\mathbf{a}_1} + e^{-i\mathbf{k}\mathbf{a}_2}) = -\gamma_0 f(\mathbf{k}) \\ \mathcal{H}_{BA} &= \mathcal{H}_{AB}^* \approx -\gamma_0 f(\mathbf{k})^* \end{aligned} \quad (\text{A.6})$$

where we restrict ourselves to electron hopping only between the first nearest neighbors (1NN) by using the geometry depicted in Fig. 1.1 and we use the notation γ_0 ($\gamma_0 > 0$) for the hopping (tunneling) energy between neighboring atoms. It is easy to see from the definition of $\mathcal{S}_{jj'} = \langle \Phi_j | \Phi_{j'} \rangle$ that $\mathcal{S}_{AA} = \mathcal{S}_{BB} = 1$ and by performing mathematical steps analogue to the ones from Eq. A.6 we obtain $\mathcal{S}_{AB} = \mathcal{S}_{BA}^* = s_0 f(\mathbf{k})$ where s_0 is the overlap between the $2p_z$ -orbitals of neighboring C atoms. We have calculated all matrix elements of \mathcal{H} and \mathcal{S} which can be written explicitly as

$$\mathcal{H} = \begin{pmatrix} \epsilon & -\gamma_0 f(\mathbf{k}) \\ -\gamma_0 f(\mathbf{k})^* & \epsilon \end{pmatrix}, \quad \mathcal{S} = \begin{pmatrix} 1 & s_0 f(\mathbf{k}) \\ s_0 f(\mathbf{k})^* & 1 \end{pmatrix}. \quad (\text{A.7})$$

Eq. A.4 can now also be solved to yield the valence and conduction band of graphene

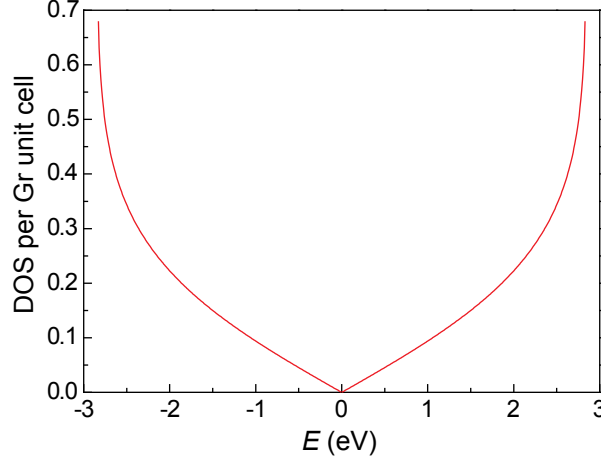


Figure A.1: Graphene density of states per unit cell as a function of energy. DOS vanishes at 0 eV where the Dirac point is located and is linear in energy in its vicinity. Additionally, van Hove singularities are noticed as divergences in the DOS. Calculation was performed for $\epsilon = 0$ eV, $s_0 = 0$ and $\gamma_0 = 2.848$ eV.

$$E(\mathbf{k}) = \frac{\epsilon \pm \gamma_0 w(\mathbf{k})}{1 \pm s_0 w(\mathbf{k})} \quad (\text{A.8})$$

with $w(\mathbf{k}) = |f(\mathbf{k})| = \sqrt{1 + 4 \cos\left(\frac{a\sqrt{3}}{2}k_y\right) \cos\left(\frac{a}{2}k_x\right) + 4 \cos^2\left(\frac{a}{2}k_x\right)}$.

Once the dispersion relation is known, we can also calculate the density of states (DOS) of graphene π orbitals. This can be done by using the standard equation for the density of states adopted to 2D systems. In the case of graphene, where double degeneracy in spin ($g_s = 2$) and valley ($g_v = 2$) has to be taken into account, the DOS per unit cell has the following form

$$\rho_{\text{Gr}}(E) = g_s g_v \frac{A_{\text{Gr}}}{(2\pi)^2} \int_{\text{FC}} \frac{dl}{|\nabla_{\mathbf{k}} E|} \quad (\text{A.9})$$

where A_{Gr} is the area of the graphene unit cell ($A_{\text{Gr}} = a^2 \sin 60^\circ$) and the integration is performed over the Fermi contour (FC). The overlap s_0 in Eq. A.8 is often negligibly small and neglected; We also use this simplification to facilitate the numerical integration of Eq. A.9. The resulting graphene DOS per unit cell is plotted in Fig. A.1 and as can be seen it is linear in the vicinity of the Dirac point (located at 0 eV) and also exhibits van Hove singularities.

By integrating the Eq. A.1 up to certain energy, we can derive an expression useful for calculating charge transfer to (or from) graphene related to doping. We define the areal density of the transferred charge n to be positive for electron-doped and negative for

hole-doped graphene. n can then be written as (having dimension of electrons per area)

$$\begin{aligned}
 n &= \frac{1}{A_{\text{Gr}}} \int_{E_{\text{D}}}^{E_{\text{F}}} \rho_{\text{Gr}}(E) dE = \frac{g_{\text{s}} g_{\text{v}}}{(2\pi)^2} \int_{E_{\text{D}}}^{E_{\text{F}}} \int_{\text{FC}} \frac{dl}{|\nabla_{\mathbf{k}} E|} dE \\
 &= \frac{1}{\pi^2} \int_{E_{\text{D}}}^{E_{\text{F}}} \int_{\text{FC}} \frac{\sqrt{dk_{\text{x}}^2 + dk_{\text{y}}^2}}{\sqrt{\left(\frac{\partial E}{\partial k_{\text{x}}}\right)^2 + \left(\frac{\partial E}{\partial k_{\text{y}}}\right)^2}} dE = \frac{1}{\pi^2} \int_{\text{FC}} dk_{\text{x}} dk_{\text{y}} = \frac{A_{\text{FC}}}{\pi^2}
 \end{aligned} \tag{A.10}$$

as can be obtained after simplification of the differentials dE and $dk_{\text{x,y}}$. Hence, the charge transfer is linearly proportional to the area of the Fermi contour A_{FC} .

Appendix B

Moiré superstructure

If two lattices having slightly different lattice constants are overlapped over each other, a moiré effect occurs. This is illustrated in Fig. B.1 where we show two overlapped triangular lattices simulating iridium (111) surface ($a_{\text{Ir}} = 2.715 \text{ \AA}$) and graphene ($a_{\text{Gr}} = 2.45 \text{ \AA}$). In panel (a), graphene zig-zag rows are aligned with the dense packed rows of iridium—an orientation known as R0 graphene. Panel (b) displays R30 graphene where graphene armchair rows are aligned with the dense packed rows of iridium. The resulting moiré structure is evident in panel (a) as an additional, long-wavelength modulation containing approximately ten graphene unit cells. By using Eq. 1.4, it is easy to calculate the moiré periodicity which for the R0 graphene amounts to 2.51 nm. For the R30 moiré, which may not be so easy to recognize in panel (b), the periodicity is 4.89 Å and it is the smallest moiré periodicity achievable for graphene on Ir(111). Insets in Fig. B.1 show the corresponding Fourier transforms where, besides the graphene and iridium spots, moiré superstructure spots can also be recognized.

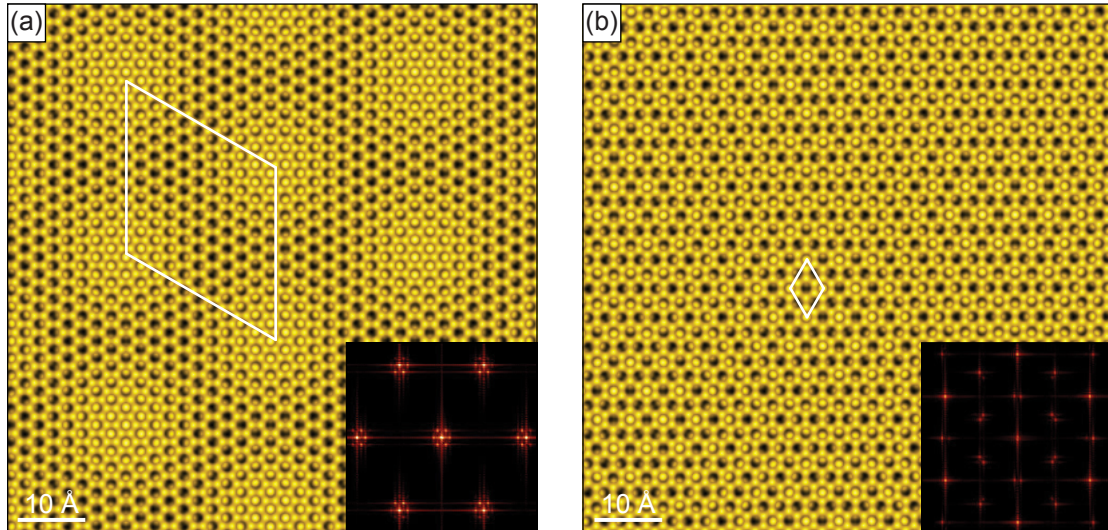


Figure B.1: (a) R0 and (b) R30 graphene on Ir(111) with the corresponding moiré superstructures visible. White rhombi mark the superstructure unit cells as calculated from Eq. 1.4. Insets show the corresponding Fourier transforms.

We note that our modeled images do not represent a simulation of real STM images (simulation of STM images require theoretical calculations utilizing e.g. DFT [187]). We have simply overlapped two triangular lattices in which individual atoms are represented as peaks of continuous periodic functions. By doing so, the corresponding Fourier transforms also give more realistic results (as opposed to e.g. simple ball model)

Appendix C

Wrinkles network simulation

Here we provide several simulated Voronoi diagrams (VDs) which will serve for a comparison with the real wrinkle networks obtained from LEEM measurement. We start with a perfectly arranged set of centroids constituting a triangular lattice [red dots in Fig. C.1(a)]. The corresponding VD is then a perfect honeycomb structure consisting of identical hexagons [dark lines in Fig. C.1(a)]. Obviously, this diagram does not match our experimentally measured wrinkles network, the degree of ordering is too high. The corresponding Fourier transform is shown in panel (b) where a highly ordered 6-fold symmetric pattern is visible.

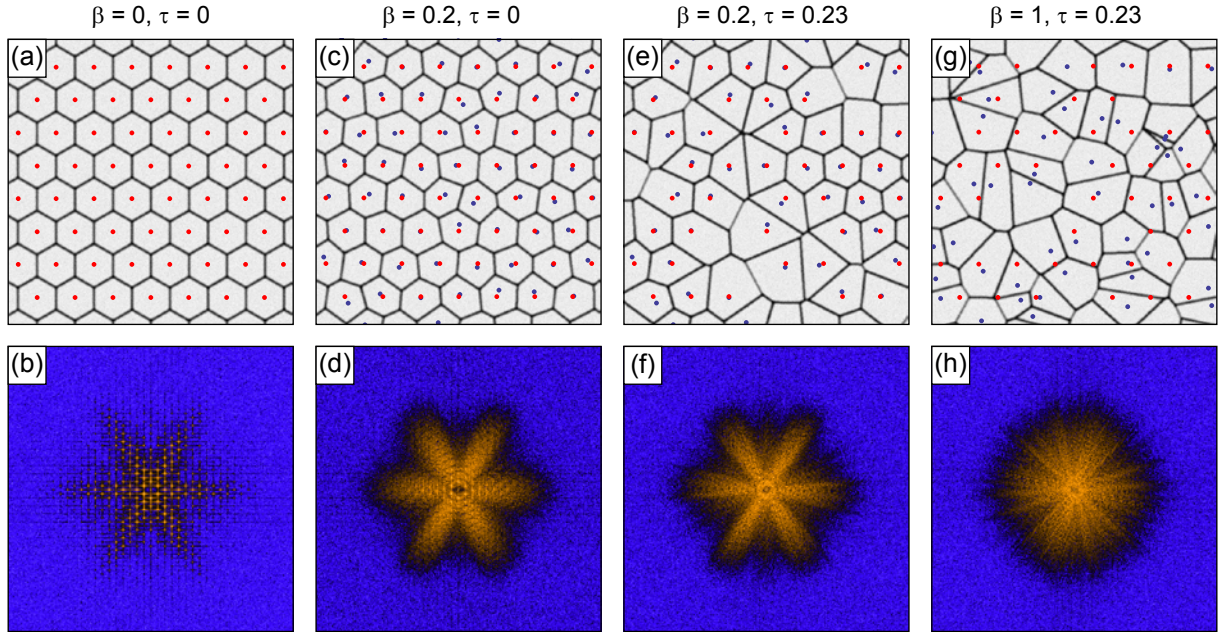


Figure C.1: A set of simulated Voronoi diagrams (upper row) and their Fourier transforms (lower row). The starting point of all diagrams is an arranged set of centroids shown in panel (a) as red dots—the same dots are shown also in all upper row panels. In panel (c), a displaced lattice process has been applied which resulted in a blue set of centroids. On top of that, in panel (e) a thinning process has also been applied resulting in a new set of blue centroids. In panel (g), displaced lattice process has been increased to yield randomly distributed blue centroids. The corresponding Voronoi diagrams generated by red [panel (a)] and blue [panels (c), (e) and (g)] centroids are marked as thick dark lines.

We want to introduce a certain amount of disorder (i.e. randomness) to our simulated diagrams. Knowing that measured wrinkles network has quasi-honeycomb structure, this step is fully justified. Disorder can be introduced by so-called displaced lattice processes and thinning processes [137]. In a displaced lattice process each of the centroids is displaced by $\alpha\beta d$ in a random direction ϕ ($0 \leq \phi < 2\pi$), where d is the distance between neighboring centroids prior to their displacement, β is displacement factor and α is a random variable ($0 < \alpha < 1$). As $\beta \rightarrow 1$, centroids start to correspond to randomly distributed set of points and their original ordering is completely lost. In a thinning process, certain fraction τ of initial centroids is randomly removed. As τ increases, the corresponding VD loses its initial ordered structure. The result of application of a displaced lattice process ($\beta = 0.2$) to our initial set of centroids from panel (a) is shown in panel (c) and is marked by blue dots. We can see that the original honeycomb structure can still be discerned in the generated VD—but now it consists of distorted 6-sided polygons. The corresponding Fourier transform, shown in panel (d), exhibits a clear 6-fold symmetric pattern with an additional fine structure still resolved (in the form of dots), reflecting the high ordering of the pre-displaced diagram. If we in addition apply a thinning process ($\tau = 0.23$) to an already displaced set of centroids, it results in VD shown in panel (e). The diagram is more irregular, consisting of polygons with 4-7 sides. Such diagram is certainly more similar to a wrinkles network recorded in LEEM which is also confirmed by the corresponding Fourier transform in panel (f). The fine substructure is now gone and the 6-fold symmetric pattern is very similar to the experimentally obtained pattern shown in Fig. 3.10(b). If the amount of randomness is increased by setting $\beta = 1$, 6-fold symmetry is completely gone from the Fourier transform is almost isotropic [cf. panels (g) and (h)]. From the comparison of these simulations and LEEM experiments we conclude that indeed the wrinkles network can be approximated by a VD and that the wrinkles distribution within that network is not random but contains a certain amount of ordering.

Sažetak na hrvatskom jeziku

Poglavlje 1 - Uvod

Kristalna struktura grafena je određena 2D heksagonalnom rešetkom s dva atoma u bazi što rezultira strukturom pčelinjih saća [vidi sl. 1.1(a)]. Takva struktura ima svoje podrijetlo u tri sp^2 hibridne orbitale koje nastaju linearnim kombinacijama $2s$, $2p_x$ i $2p_y$ ugljikovih orbitala. Te tri hibridne orbitale leže u istoj ravnini i međusobno tvore kut od 120° , što je karakterističan kut strukture pčelinjih saća. Preostale $2p_z$ orbitale ne sudjeluju u hibridizaciji i ostaju stajati okomito na sp^2 hibridnu ravninu. sp^2 orbitale susjednih atoma ugljika sačinjavaju σ veze koje pak tvore σ vrpce u grafenu. σ veze su odgovorne za izuzetnu mehaničku čvrstoću grafena te ujedno definiraju C-C atomsku udaljenost koja je jednaka 1.42 \AA . Tuneliranje elektrona između $2p_z$ orbitala stvara π veze i odgovarajuće π vrpce koje su polupopunjene i koje definiraju većinu elektroničkih i optičkih svojstava grafena. Na sl. 1.1(b) su obilježene točke visoke simetrije u Brillouinovoj zoni (BZ) grafena: Γ , M, K i K'. U kutovima BZ nalazimo K i K' točke koje su neekvivalentne budući da nije moguće izvesti translaciju iz K u K' pomoću jediničnih vektora \mathbf{b}_1 i \mathbf{b}_2 . Kako se u bazi jedinične ćelije grafena nalaze dva atoma, valne funkcije elektrona se opisuju s dvije komponente. Matematički gledano, te dvije komponente mogu se shvatiti kao dva moguća smjera spina što omogućuje definiciju tzv. pseudospinskog stupnja slobode elektrona.

Zbog toga što grafenske π vrpce potječu od tuneliranja elektrona između susjednih $2p_z$ orbitala, one se mogu opisati aproksimacijom čvrste veze. Uzimajući u obzir samo tuneliranje između prvih susjeda, disperzijska relacija valentne π i vodljive π^* vrpce ima oblik $E(\mathbf{k}) = [\epsilon \pm \gamma_0 w(\mathbf{k})] / [1 \pm s_0 w(\mathbf{k})]$ gdje je ϵ orbitalna energija $2p_z$ ni-

voa, γ_0 i s_0 su energije tuneliranja i preklap između $2p_z$ orbitala susjednih atoma, a $w(\mathbf{k}) = \sqrt{1 + 4 \cos\left(\frac{a_{\text{Gr}}\sqrt{3}}{2}k_y\right) \cos\left(\frac{a_{\text{Gr}}}{2}k_x\right) + 4 \cos^2\left(\frac{a_{\text{Gr}}}{2}k_x\right)}$. Grafički prikaz ove disperzijske relacije se nalazi na sl. 1.2. Zbog linearne ovisnosti $E(\mathbf{k})$ u blizini K i K' točaka, elektroni se mogu opisati Diracovom jednažbom za bezmasene čestice, a odgovarajuća elektronska stanja predstavljaju tzv. Diracove stošce u k -prostoru. U skladu s time, točke stožaca u kojima se dodiruju π i π^* vrpce se nazivaju Diracovim točkama.

Kroz ovu tezu ćemo se baviti epitaksijalnim grafenom sintetiziranim na (111) površini iridija [Gr/Ir(111)]. Takav grafen pokazuje iznimnu strukturnu kvalitetu što je posljedica gotovo savršenog slaganja između $\langle 10\bar{1} \rangle$ i $\langle 11\bar{2}0 \rangle$ smjerova iridija i grafena (tzv. R0 grafen). Sinteza grafena se ostvaruje na visokim temperaturama u uvjetima ultra-visokog vakuumu pomoću katalitičke dekompozicije plinovitih ugljikohidrata [10, 41] i uvijek rezultira samo jednim grafenskim slojem. Iz STM mjerenja je utvrđeno da konstanta rešetke grafena na Ir(111) iznosi $a_{\text{Gr}} = 2.45 \text{ \AA}$ [41]. Dodatna karakteristika Gr/Ir(111) je tzv. moiré superperiodičnost ($a_{\text{moiré}} = 25.3 \text{ \AA}$) koja nastaje preklapanjem dviju dobro definiranih rešetki čije se jedinične ćelije razlikuju za mali iznos. Osim kristalne strukture, grafen na Ir(111) pokazuje iznimno dobro očuvanu intrinzičnu elektronsku strukturu. Stanja Diracovog stošca su gotovo netaknuta [46–48, 50] što se može vidjeti na sl. 1.6(b). Uočavaju se dvije linearne grane Diracova stošca koje se sastaju na 0.1 eV iznad E_F [46]. Osim toga, vide se mini-procjepi i replike Diracova konusa koje su posljedica postojanja moiré superstrukture.

Prilikom hlađenja s visokih temperatura na kojima se odvija sinteza, grafen i iridij se sakupljaju u skladu sa svojim koeficijentima termalne ekspanzije. Kako je taj koeficijent za grafen zanemariv u odnosu na iridij, tijekom hlađenja se u grafenu javlja naprezanje koje se u određenom trenutku relaksira u vidu tzv. grafenskih nabora koji se formiraju u smjeru okomitom na grafensku ravninu (vidi sl. 1.7 i 1.8). Ovakvi nabori se nalaze u mnogim sistemima epitaksijalnog grafena [9, 53–57] uključujući i Gr/Ir(111) [44, 45, 58]. Osim cjelovitog sloja, na iridiju se mogu sintetizirati grafenski otoci čije karakteristične dimenzije mogu biti svega nekoliko nanometara, kada se nazivaju grafenskim kvantnim točkama. Vrlo detaljna STM studija o morfologiji grafenskih otoka je dana u Ref. [66]. Zbog srastanja, više temperature sinteze grafena daju veće otoke i manju površinsku gustoću otoka. XPS i DFT rezultati pokazuju da se otoci najjače vežu s iridijem na svojim rubovima gdje je interakcija između C $2p$ i Ir d vrpce najjača [68]. U grafenskim

kvantnim točkama postaju izraženi efekti kvantnog zatočenja elektrona koji su istraženi tehnikama kao što su STM i STS, ali i putem teorijskih proračuna [70–73], gdje je jedan od glavnih rezultata vizualizacija valnih funkcija elektrona iz čega se može odrediti i njihova disperzijska relacija.

Interkalacija je jedan od najčešćih načina za promjenu svojstava epitaksijalnog grafena i kao takva je zanimljiva iz nekoliko različitih aspekata. Jedan od njih je smanjenje međudjelovanja grafena s podlogom [11, 74, 75]. Nadalje, učinak karakterističan za gotovo sve interkalirane sustave je kemijsko dopiranje grafena [77] koje može biti n ili p tipa. Zbog male gustoće stanja grafena na Fermijevom nivou, čak i mali transferi naboja u grafen rezultiraju značajnim pomakom Diracove točke. Ovi i neki drugi efekti interkalacije su također važni za potencijalne primjene grafena [76, 79–85]. I u slučaju Gr/Ir(111) je pokazano da se različiti atomi i molekule mogu uspješno interkalirati između grafena i iridija [69, 76, 84, 86–94]. Međutim, još uvijek ne postoji zadovoljavajuće objašnjenje o načinu na koji dolazi do penetracije atoma kroz naizgled savršenu grafensku membranu kakva je grafen na Ir(111). Logična pretpostavka jest da je za interkalaciju potrebno postojanje neke vrste defekata ili pukotina. Ti defekti mogu biti prisutni u grafenu prije interkalacije ili mogu biti privremeno inducirani prisutnošću atoma u neposrednoj blizini grafena. Dodatno, nije jasno koja je pokretačka sila interkalacije. Teoretski proračuni pokazuju da prolazak atoma kroz defekte u grafenu iziskuje relativno velike količine energije (i do 10 eV) [96, 100]. Osim toga, svaki C atom u Gr/Ir(111) sustavu je vezan na iridij energijom od 50 meV [51] koja se treba nadoknaditi prilikom umetanja drugih atoma između grafena i iridija. Dakle, da bi interkalacija bila uspješna, svi ti troškovi u energiji moraju biti pokriveni.

Na kraju uvodnog poglavlja navodimo glavne ciljeve ove teze. S aspekta rasta, pratit će se evolucija popunjene i nepopunjene elektronske strukture tijekom povećanja pokrivenosti iridijeve površine grafenom. Također će se karakterizirati strukture koje nastaju tijekom formiranja potpunog grafenskog sloja s posebnim naglaskom na grafenske nabore. Drugi zadatak ovog rada je razjašnjavanje mehanizma i dinamike interkalacije epitaksijalnog grafena. Nadalje, želimo istražiti učinke interkalacije različitih atoma na elektronsku strukturu i morfologiju grafena i iridija te vidjeti kako ti efekti utječu na međudjelovanje grafena s okolinom.

Poglavlje 2 - Priprema uzorka i eksperimentalne metode

Priprema uzorka kao i svi eksperimenti se obavljaju u uvjetima ultra-visokog vakuuma s osnovnim tlakom reda veličine 10^{-11} do 10^{-10} mbar. Sintezi grafena prethodi čišćenje monokristala iridija koje se odvija u nekoliko koraka. Prvo se vrši bombardiranje ionima plemenitih plinova (najčešće Ar^+) u rasponu energije iona između 1 i 2 keV. Ovaj korak se provodi na sobnoj ili povišenim temperaturama (~ 870 K). Zatim slijedi nekoliko ciklusa grijanja sa i bez prisustva kisika. Tijekom tretmana kisikom, obično na 1120 K, velika većina preostale prljavštine na površini uzorka oksidira i biva uklonjena. Grijanje bez kisika (u temperaturnom rasponu između 1370 i 1570 K) osigurava strukturnu kvalitetu podloge i odsutnost adsorbata. Nakon toga slijedi sinteza grafena kod koje se koriste dva glavna postupka—temperaturno programirani rast (TPG) i kemijska depozicija para (CVD) u kojima se koristi svojstvo površine iridija da katalitički rastavlja ugljikovodike na njihove sastavne dijelove [66]. Kao izvor ugljika koristio se eten (etilen) ili metan. TPG se sastoji od adsorpcije ugljikovodika na površini iridija na sobnoj temperaturi do zasićenosti. Tipična doza potrebna za to je 5×10^{-8} mbar ugljikovodika tijekom 50 s. Zatim slijedi kratko grijanje (1070-1470 K, 30 s) koje rezultira formiranjem grafenskih otoka čija prosječna veličina ovisi o temperaturi grijanja [66]. Ponavljanjem TPG postupka više puta povećava se pokrivenost iridija grafenom i na kraju se dobiva jedan cjeloviti grafenski sloj. CVD podrazumijeva izlaganje vruće površine iridija (~ 1120 K) atmosferi ugljikovodika u dozi od 1×10^{-7} mbar tijekom 15 min što rezultira stvaranjem potpunog sloja grafena. Također, različite kombinacije TPG i CVD postupaka su moguće. Nakon što se čitava površina iridijevog kristala prekrije jednim slojem grafena, rast sljedećeg sloja je onemogućen zbog nedostatka slobodne, katalitički aktivne iridijeve površine. Dodatna depozicija različitih elemenata na uzorak je izvršena posebno dizajniranim evaporatorima (Cs, Li, Eu) ili puštanjem plina u vakuumsku komoru (O).

Mjerenja elektronske strukture su izvršena pomoću dviju tehnika. Prva od njih je kutno-razlučiva fotoemisijska spektroskopija (ARPES) koja je idealna za istraživanje popunjenih elektronskih vrpca. Metoda se temelji na fotoelektričnom efektu u kojem upadni foton uzrokuje izbacivanje elektrona iz uzorka [vidi sl. 2.2(a)]. Nakon izbacivanja, kinetička energija elektrona (E_{kin}) i kutevi izlaska iz površine (φ , τ i θ) određuju se anali-

zatorom elektrona [vidi sl. 2.1(a)]. Iz zakona očuvanja energije i impulsa se tada lako dobiva disperzijska relacija $E_B(k_x, k_y)$ gdje je E_B vezivna energija elektrona u odnosu na Fermijev nivo a k_x i k_y su komponente valnog vektora elektrona. Treba naglasiti da dobiveni fotoemisijski spektri sadrže i doprinose od višečestičnih međudjelovanja čiji se točan oblik može odrediti analizom podataka. Fotoemisijski spektri prikazani u ovoj tezi su snimljeni na jednom od tri korištena eksperimentalna postava smještena na Institutu za fiziku (Zagreb), sinkrotronu Elettra (Trst) i Nacionalnom laboratoriju Brookhaven.

Dvo-fotonska fotoemisijska spektroskopija (2PPE) je druga tehnika korištena za karakterizaciju elektronske strukture uzorka, specifično njenog nepopunjenog dijela. U toj tehnici se koriste dva fotona kako bi se dobile informacije o elektronskim stanjima iznad Fermijevog nivoa: prvi foton pobuđuje elektron ispod E_F u međustanje između E_F i E_V dok drugi foton izbacuje elektron iznad E_V [vidi sl. 2.2(b)] i omogućava njegovu detekciju. Daljnji princip određivanja disperzijske relacije je isti kao i u slučaju ARPES-a s time da se određuje vezivna energija elektrona u odnosu na vakuumski nivo. 2PPE mjerenja prikazana u tezi su obavljena na Sveučilištu Columbia (New York).

Pretražnom tunelirajućom mikroskopijom i spektroskopijom (STM i STS) su određena morfološka i spektroskopska obilježja uzorka na atomskom nivou. Princip rada instrumenta prikazan je na sl. 2.3. Tuneliranje elektrona se odvija između atomski oštre špice i uzorka kada se između njih primjeni razlika potencijala V_t . Rezultirajuća struja tuneliranja I_t se mjeri kao funkcija položaja špice iznad uzorka. Konačna STM slika ovisi o gustoći elektronskih stanja špice i uzorka kao i o udaljenosti špica-uzorak. Uz pomoć lock-in pojačala moguće je dobiti strujni signal koji odgovara tuneliranju elektrona iz uzorka točno određene energije, što je onda spektroskopski način rada instrumenta (tj. STS). Instrumenti koji su korišteni za STM i STS eksperimente se nalaze na Institutu za fiziku (Zagreb) i Sveučilištu u Kölnu.

Dodatne informacije o morfologiji uzorka dobivene su pomoću nisko-energetske elektronske mikroskopije (LEEM) [vidi sl. 2.4]. Elektroni emitirani iz elektronskog topa se ubrzavaju električnim poljem, putuju prema objektivu prolazeći pritom kroz magnetski separator koji ih zakreće. Prije dolaska do uzorka, elektroni se usporavaju na energije od nekoliko eV (zbog čega postaju površinski osjetljivi), reflektiraju se od uzorka i bivaju ubrzani natrag kroz objektiv i prema analizatoru prolazeći još jednom kroz magnetski separator. Ako uzorak ima kristalnu strukturu, refleksija elektrona od površine je u principu

difrakcija i difrakcijska slika uzorka nastaje u stražnjoj žarišnoj ravnini objektiva. Jedan od ključnih dijelova mikroskopa je magnetski separator koji se koristi za odvajanje dolazne i reflektirane elektronske zrake i omogućuje realizaciju reflektivne geometrije mikroskopa. Uz adekvatnu opremu, takav instrument je također sposoban za druge vrste mjerenja—već je spomenuta difrakcija (odnosno nisko-energetska elektronska difrakcija, LEED) te su tu još *IV*–LEEM spektroskopija, fotoemisijska elektronska mikroskopija (PEEM), spinsko-polariziran LEEM (SPLEEM), zrcalna elektronska mikroskopija (MEM), ARPES i fotoemisijska spektroskopija x-zrakama (XPS).

Poglavlje 3 - Mikroskopska karakterizacija rasta grafena

Nakon svakog TPG ciklusa rasta, određeni udio slobodne iridijeve površine f biva prekriven grafenom. Kao što je pokazano, pokrivenost iridija grafenom θ_{Gr} nakon N TPG ciklusa se može opisati jednačbom $\theta_{\text{Gr}}(N) = 1 - (1 - f)^N = 1 - e^{-\lambda}$ gdje je $f = 1 - e^{-\lambda}$ a λ je brzina rasta grafena [47]. Određivanjem pokrivenosti grafena nakon nekoliko različitih brojeva TPG ciklusa te uz pomoć gore dane jednačbe moguće je precizno odrediti vrijednost λ . To je i učinjeno analizom niza STM slika iz koje proizlazi da je $\lambda_{\text{STM}} = 0.21$ [47]. Slična analiza je napravljena i za niz LEEM slika prikazanih na sl. 3.3 koja daje vrijednost $\lambda_{\text{LEEM}} = 0.162$. Treba naglasiti da je pouzdanost ovih vrijednosti ograničena zbog konačne površine uzorka dostupne u mjerenju (u STM-u) te rezolucije instrumenta (u LEEM-u).

Dodatan opis rasta grafena dolazi iz promatranja evolucije elektronske strukture u okolini K točke. Snimljen je niz ARPES spektara Diracovog stošca i iridijevog površinskog stanja tokom rasta grafena koji se sastojao od 17 uzastopnih TPG ciklusa. Neki od tih spektara su prikazani na sl. 3.6(a). Ono što se može vidjeti jest postepeno povećanje fotoemisijskog intenziteta Diracovog stošca i isto tako smanjenje intenziteta iridijevog površinskog stanja. Analizom intenziteta stošca i prilagodbom podataka na jednačbu eksponencijalnog rasta iz prethodnog odjeljka [$I_{\text{Gr}}(N) \sim (1 - e^{-\lambda N})$, vidi sl. 3.6(c)], dobiva se vrijednost $\lambda_{\text{ARPES}} = 0.196$ što je u dobrom slaganju s vrijednošću dobivenom iz STM mjerenja. Razumna je pretpostavka da se intenzitet iridijevog površinskog stanja također smanjuje prema eksponencijalnom zakonu $I_{\text{Ir}}(N) \sim e^{-\lambda N} + I_{\text{off}}$ gdje je I_{off}

uveden zbog činjenice da intenzitet iridijevog površinskog stanja ne pada na nulu ni u slučaju $\theta_{\text{Gr}} = 1$. Analiza podataka daje vrijednost $\lambda_{\text{Ir}} = 0.45$, odnosno intenzitet iridijevog površinskog stanja pada puno brže no što raste intenzitet Diracovog stošca. Ta razlika se objašnjava raspršenjem iridijevih elektrona na rubovima grafenskih otoka, potencijalno mogućim pomakom površinskog stanja iznad Fermijevog nivoa te gušenjem fotoemisijskog intenziteta koje je proporcionalno θ_{Gr} [47]. Nadalje, iz serija rasta grafena od 17 TPG ciklusa na različitim temperaturama (1070, 1170, 1270, 1370 i 1470 K), dobivene vrijednosti λ_{ARPES} ostaju iste dok se λ_{Ir} smanjuje kako temperatura raste (vidi sl. 3.7). Time je dokazano da rubovi grafenskih otoka (čija je površinska gustoća veća na višim temperaturama rasta) zaista raspršuju elektrone iridijevih površinskih stanja što je posljedica relativno jačeg vezanja grafenskih rubova na iridij.

Važna fizikalna veličina usko vezana uz elektronsku strukturu uzorka je izlazni rad. Koristeći metodu 2PPE, izlazni rad uzorka se lako izračunava prema izrazu $\Phi = 2\hbar\omega - \Delta E$ gdje je $\hbar\omega$ korištena fotonska energija a, ΔE je energetska razlika između visokoenergetskog i niskoenergetskog ruba u 2PPE spektru. Ponavljajući TPG proceduru za rast, pripremljeni su uzorci s različitim grafenskim pokrivenostima te se dobiva da izlazni rad linearno opada sa θ_{Gr} od 5.79 eV za čisti iridij do 4.65 eV za iridij u potpunosti prekriven grafenom (vidi sl. 3.9).

Nadalje, fokusiramo se na grafenske nabore koji su neizostavna karakteristika grafena na Ir(111) i kao takvi zahtijevaju detaljno razumijevanje. Sl. 3.10(a) pokazuje karakteristično područje na Gr/Ir(111) u kojemu se grafenski nabori lako identificiraju kao debele tamne linije $\sim 1 \mu\text{m}$ duljine i koje tvore složenu mrežu. U Fourierovom transformatu te slike [sl. 3.10(b)] jasno se razaznaje simetričan uzorak koji nam govori da postoje tri preferentna smjera u kojima se grafenski nabori pružaju. Znajući da je proces nastajanja nabora usko povezan sa strukturom iridija kao podloge, utvrđen je razmještaj atoma na iridijevoj površini te proizlazi da se smjerovi pružanja nabora i smjerovi gusto pakiranih atomskih redova iridija savršeno poklapaju (vidi sl. 3.11). Ovakvo slaganje nađeno je samo za R0 grafen; kod grafena rotiranog za 30° u odnosu na iridij ne nalazimo ovakvo uređenje zbog reduciranog vezanja grafen-iridij [50]. Snimanjem LEEM slika u realnom vremenu tokom ciklusa zagrijavanja i hlađenja već potpuno formiranog Gr/Ir(111) uzorka, promatrana je dinamika nestajanja i ponovnog nastajanja grafenskih nabora. Pokazuje se da u trenutku nastajanja nabora dolazi do promjene LEEM kontrasta u njihovoj okolini

(sl. 3.13) što se objašnjava lokalnom relaksacijom napetosti u grafenu odnosno lokalnoj promjeni udaljenosti između grafena i iridija te također udaljenosti između pojedinih C atoma. Nadalje, utvrđeno je da dio nabora nastaje uvijek na istom mjestu na uzorku dok se drugi dio raspoređuje nasumično, vidi sl. 3.15, što znači da je njihovo nastajanje povezano s defektima, bilo iridijeve površine bilo grafenske rešetke, koji služe kao sidrišta za nastanak nabora.

Što se tiče cjelokupne mreže grafenskih nabora, napravljena je njena usporedba s Voronoi dijagramom koji nastaje tako da se za dani skup točaka u prostoru konstruira mreža linija koje odgovaraju polovištima između svakog para točaka. Preklop jednog takvog dijagrama i LEEM slike na kojoj se vide grafenski nabori je prikazan na sl. 3.16. Može se vidjeti da postoji znatno podudaranje između dijagrama i mreže nabora što znači da se može iskoristiti matematički aparat koji je razvijen za opis Voronoi dijagrama kako bi se kvantificirale karakteristike mreže nabora. Štoviše, pokazano je da prikazani Voronoi dijagram nije nasumičan tj. da točke koje ga generiraju nisu nasumično raspoređene u prostoru [tada bi npr. Fourierov transformat na sl. 3.10(b) bio izortopan] već da one odgovaraju heksagonalnoj rešetci u koju je unesena malena količina nereda. To je dodatna potvrda da mreža grafenskih nabora zaista u sebi sadrži kvazi-heksagonalno uređenje koje je usko povezano sa simetrijom (111) površine iridija.

Sada se okrećemo unutarnjoj strukturi pojedinih nabora i mjesta na kojima se nabori križaju. Sl. 3.17 prikazuje nekoliko STM slika različitih segmenata nabora snimljenih na sobnoj temperaturi. Iz njih se može zaključiti da se pojedini nabor ne može opisati jednostavnim polukružnim profilom već složenijim oblikom koji unutar sebe sadrži više manjih nabora. Takva struktura je posljedica međugre između van der Waals interakcije koja djeluje između pojedinih dijelova nabora i iridija te elastične energije savnutih segmenata grafena. Općenito, širina (10-50 nm) i visina (1-5 nm) nabora variraju što ovisi i o točnim uvjetima pripreme grafena. Za razliku od ravnih dijelova, križanja nabora prikazuju vrlo nehomogenu strukturu [vidi sl. 3.17(d)]. Iako nije moguće u detalje razaznati strukturu grafena u takvim područjima, vrlo je vjerojatno da oni sadrže pukotine, rupe i druge vrste defekata. Pokazuje se da su ti defekti od iznimne važnosti za interkalaciju grafena.

Poglavlje 4 - Elektronska struktura u centru Brillouinove zone

U Γ točki iridijeve (111) površine nalazimo površinska stanja koja su spinski rascijepljena odnosno u kojima je razbijena spinska degeneracija. Disperzija takvih Rashba-rascijepljenih stanja može se općenito zapisati kao $E_{\pm}(\mathbf{k}_{\parallel}) = \hbar^2 \mathbf{k}_{\parallel}^2 / 2m^* \pm \alpha_R |\mathbf{k}_{\parallel}| + E_0$ gdje je m^* efektivna masa, α_R parametar cijepanja a E_0 vezivna energija stanja. Važno je što ta stanja postoje čak i kad je površina iridija u potpunosti prekrivena grafenom [127], odgovarajući ARPES spektri na kojima je to vidljivo prikazani na sl. 4.1(a). Mogu se zamijetiti dva parabolična stanja s negativnim efektivnim masama koja su međusobno razmaknuta u k -prostoru. Analizom spektara izračunata je njihova efektivna masa $m^* = -0.163 m_e$, parametar cijepanja $\alpha_R = 1.89 \text{ eV \AA}$ i vezivna energija $E_0 = 0.191 \text{ eV}$ što su vrijednosti koje se podudaraju s literaturom [127, 134]. 3D model površinskih stanja temeljen na izračunatim parametrima je prikazan na sl. 4.1(b). Teorijski proračuni pokazuju da su stanja p_z tipa samo u blizini Γ točke dok su na većim valnim vektorima $d_{x,z}$ karaktera [143] što znači da tamo prelaze u površinske rezonancije. Ovakvo ponašanje tih stanja je također u slaganju s APRES rezultatima prikazanih na sl. 4.3(a) gdje se vidi odstupanje od parabolične disperzije za $k \gtrsim 0.13 \text{ \AA}^{-1}$.

Također u Γ točki, ali u nepopunjenom dijelu elektronske strukture Gr/Ir(111) nalaze se stanja zrcalnog potencijala (IP stanja) koja su istražena 2PPE-om. Disperzija IP stanja je prikazana na sl. 4.2(a) gdje se jasno mogu razaznati dva takva stanja blizu vakuumskeg nivoa, I_1 i I_2 , koja imaju paraboličnu disperziju. Vezivne energije tih stanja dobivene su analizom profila 2PPE spektra prikazanog na sl. 4.2(b) i one iznose $E_{B1} = -0.81 \text{ eV}$ i $E_{B2} = -0.20 \text{ eV}$ u odnosu na vakuumski nivo, što je u dobrom slaganju s otprije dobivenim rezultatima [134]. Također, dobivene vrijednosti vezivne energije dobro se uklapaju u Rydbergovu seriju energetskih nivoa s kvantnim defektom kao što se i očekuje za IP stanja. Treba napomenuti da nije uočena dvostruka serija parnih i neparnih IP stanja kao što je predviđeno za slobodnostojeći grafen [31] što je posljedica prisutnosti iridija i lomljenja zrcalne simetrije sustava.

U 2PPE procesu, Rashba-rascijepljena iridijeva površinska stanja i IP stanja grafena na Ir(111) su blisko povezana. Jednostavnom usporedbom njihovih disperzija te uz poznavanje fotonske energije pobude, pokazuje se da su upravo površinska stanja početna

stanja u 2PPE procesu [vidi sl. 4.3(b) i (c)]. Štoviše, moguće je ostvariti rezonantni prijelaz između površinskih stanja i IP stanja za određeni interval valnih vektora preciznim ugađanjem fotonske energije što se očituje kao značajno povećanje fotoemisijskog intenziteta u 2PPE spektru. Zanimljivo je da je energetska udaljenost između IP stanja i Fermijevog nivoa konstantna bez obzira na izlazni rad uzorka koji linearno pada s pokrivenošću grafena (vidi sl. 3.9). Ova činjenica je direktan dokaz lokalizacije elektrona koji populiraju IP stanja na grafenskim otocima zbog velike razlike u izlaznim radovima $\Phi_{\text{Ir}(111)} - \Phi_{\text{Gr/Ir}(111)} = 1.14 \text{ eV}$. Slični efekti lokalizacije su uočeni i u STS eksperimentima na grafenskim kvantnim točkama [148].

Poglavlje 5 - Mehanizam i efekti interkalacije cezijem

Interkalacija grafena na Ir(111) cezijem iskorištena je za dobivanje novih saznanja o osnovama procesa interkalacije koja se mogu primijeniti i na druge epitaksijalne sisteme, pogotovo na one u kojima je elektronsko $s - \pi$ međudjelovanje od temeljne važnosti. Pomoću LEED-a su istražene različite strukture koje se javljaju pri depoziciji cezija na Gr/Ir(111). Utvrđeno je da je najgušća Cs struktura koju je moguće dobiti $(\sqrt{3} \times \sqrt{3})R30^\circ$ u odnosu na Ir(111) i ona je definirana kao jedan sloj (ML) cezija. Za manje koncentracije manje od $\sim 0.9 \text{ ML}$ u LEED-u se ne raspoznaje jasna Cs struktura, no idući dalje prema 1 ML cezija dobivaju se redom (2×2) struktura u odnosu na grafen, mješavina (2×2) i $(\sqrt{3} \times \sqrt{3})R30^\circ$ struktura te na kraju samo $(\sqrt{3} \times \sqrt{3})R30^\circ$ struktura (vidi sl. 5.1). Iz niskotemperaturnih STM mjerenja uzorka sa $\sim 0.5 \text{ ML}$ cezija (sl. 5.2) utvrđeno je da postoji fazna separacija atoma cezija na rijetku adsorbiranu fazu (α fazu) i gustu interkaliranu fazu (γ fazu). Snimanjem interklairarnih područja u atomskoj rezoluciji pokazano je da Cs atomi ispod grafena zaista tvore (2×2) i $(\sqrt{3} \times \sqrt{3})R30^\circ$ strukture, što potvrđuje strukturne rezultate dobivene iz LEED-a. Promatranjem *in situ* depozicije cezija na Gr/Ir(111) u LEEM-u također je jasno uočena fazna separacija gdje dvije faze cezija daju različiti kontrast (vidi sl. 5.4) kao i drugačiji potpis u $IV - \text{LEEM}$ spektroskopiji (sl. 5.5). Dodatno, utvrđeno je da formiranje α faze po čitavoj površini uzorka prethodi pojavi γ faze. Dodatni uvid dolazi iz ARPES mjerenja. Za malene količine deponiranog cezija uočen je kontinuirani pomak Diracovog stošca prema većim vezivnim energijama (vidi sl. 5.6) što je posljedica prijenosa elektrona s atoma cezija α faze u grafen. Daljnje dodavanje

cezija na uzorak rezultira pojavom dodatnog Diracovog stošca na većim vezivnim energijama što se vidi na fotoemisijskim spektrima prikazanim na sl. 5.7(b). Dodatni stožac je posljedica dopiranja grafena elektronima atoma cezija iz γ faze koja se počela formirati na uzorku. Dakle, dva Diracova stošca su jasan potpis postojanja dviju različitih faza na površini uzorka. Očigledno je da je dopiranje puno veće u γ fazi i ono iznosi $\approx 1 \times 10^{14} \text{ cm}^{-2}$.

Detaljno objašnjenje o razlozima fazne separacija kao i točnom mehanizmu interkalacije cezija kod Gr/Ir(111) dobivamo iz teorijskih računa [152]. Uzimanjem u obzir van der Waals međudjelovanje, proizlazi da je za male Cs koncentracije energetski najpovoljnije da se atomi cezija smještaju na grafen, u α fazu (vidi sl. 5.8). Međutim, za velike Cs koncentracije postaje povoljnije za atome cezija da budu interkalirani između grafena i iridija. Ovakvo ponašanje je upravo ono što je uočeno u eksperimentima. Razlog tome je međuigra između Coulombovog odbijanja između atoma i dominantno van der Waals vezanja grafena na iridij. Za početne, male koncentracije cezija interkalacija nije dozvoljena zbog van der Waals vezanja grafena na iridij koje treba kompenzirati kako bi interkalacija bila energetski povoljna. Međutim, za velike Cs koncentracije, Coulombovo odbijanje nabijenih Cs atoma u α fazi postaje jako i u jednom trenutku atomima cezija postaje povoljnije da interkaliraju između grafena i iridija plaćajući pritom energetski trošak delaminacije grafena koji je tada podijeljen između mnogo Cs atoma. Dodatno, nabijeni Cs atomi su bolje zasjenjeni kada se nalaze blizu površine iridija što dodatno smanjuje Coulombovo odbijanje u interkaliranoj fazi.

In situ LEEM mjerenja interkalacije jasno pokazuju da su mjesta prolaska cezijeve atoma kroz grafen križanja grafenskih nabora ili njihova neposredna blizina (sl. 5.10). Ovo opažanje u skladu je s našim STM mjerenjima [vidi sl. 3.17(d)] gdje je utvrđeno da su križanja nabora mjesta koja sadrže defekte koji omogućuju prolazak atoma kroz grafen. Nadalje, rast interkaliranih Cs otoka je predodređen prostornim rasporedom grafenskih nabora i stepenica iridijeve površine koje predstavljaju energetsku barijeru za difuziju atoma cezija. Važnost iridijevih stepenica za rast interkaliranih Cs otoka je dodatno potvrđena LEEM mjerenjima interkalacije grafena na vicinalnoj Ir(100) površini (sl. 5.11) gdje je pokazano da Cs otoci rastu gotovo isključivo paralelno s iridijevim stepenicama.

Dodatni uvid u važnost van der Waals međudjelovanja u sistemima epitaksijalnog grafena dolazi iz eksperimenata de-interkalacije grafena što se postiže zagrijavanjem pot-

puno interkaliranog uzorka do visokih temperatura. Sl. 5.12 prikazuje površinu uzorka na nekoliko različitih temperatura. Postoji temperaturna granica od ~ 770 K ispod koje de-interkalacija nije moguća. Međutim, čim se ta granica prijeđe, dolazi do de-interkalacije kroz defekte u grafenu (po pretpostavci također smještenih na križanjima nabora) što se u LEEM-u očituje kao nagla promjena kontrasta na $\sim 80\%$ površine uzorka koja odgovara čistom, neinterkaliranom grafenu. Preostalih $\sim 20\%$ površine ostaje interkalirano čak i na puno višim temperaturama od ~ 1070 K. Dakle, dio interkaliranog cezija ostaje zarobljeno u obliku dobro definiranih otoka okruženih grafenom koji se natrag vezao van der Waals silama na iridij i na taj način zatvorio put prema defektima kroz koje bi de-interkalacija bila moguća.

Interkalirani grafen je također dobar poligon za promatranje efekata raspršenja kvazi-čestica na defektima. Zbog prijenosa naboja u grafen koji rezultira povećanjem Fermijeve površine, povećava se i dostupan fazni prostor u kojem se raspršenja mogu dogoditi čime je olakšano njihovo eksperimentalno opažanje. Zbog očuvanja pseudospinskog stupnja slobode, raspršenje između elektronskih stanja istog stošca su zabranjena za Diracove elektrone, ali tih zabrana nema za elektrone na Fermijevom nivou interkaliranog odnosno dopiranog grafena za koje više ne vrijedi $E \propto \mathbf{k}$. Efekti raspršenja su istraženi pomoću STM-a i STS-a za grafen na Ir(111) interkaliran cezijem. Stojni valovi koji nastaju prilikom raspršenja elektrona na defektima stvaraju konture u k -prostoru centrirane oko Γ , K i K' točaka (vidi sl. 5.16). Oblik tih kontura odgovara oblicima Fermijevih kontura za određeno dopiranje i kao takve se mogu iskoristiti za izračunavanje prijenosa naboja u grafen.

Kombiniranim STM i ARPES mjerenjima istražene su posljedice koje interkalacija ima na svojstva ionske adsorpcije atoma na grafen. Usporedbom podataka dobivenih iz foto-emisijskih spektara i $I(z)$ spektroskopije na uzorcima djelomično interkaliranih cezijem i europijem (vidi sl. 5.17 i 5.18), pokazano je da je razlika u položajima Diracovih točaka dvaju različito dopiranih područja na uzorku (interkaliranog i ne-interkaliranog) jednaka razlici izlaznih radova ta dva područja, $\Delta E_D = \Delta \Phi$. Drugim riječima, energetski razmak između Diracove točke i vakuumske nivoa je uvijek približno konstantan kao što je skicirano na sl. 5.20. Ovime se objašnjava preferencija ionske adsorpcije na ne-interkalirana područja grafena kao što se može vidjeti npr. na sl. 5.19 u slučaju adsorpcije cezija kod koje se atomi cezija nalaze gotovo isključivo samo na ne-interkaliranim područjima.

Naime, u pojednostavljenom modelu ionske adsorpcije u kojem dominantni dio vezivne energije adsorbata dolazi od delokalizacije elektrona u grafenu, iz sl. 5.20 vidljivo je da će energetski dobitak kod adsorpcije biti najveći u područjima najvećeg izlaznog rada, a to su upravo ne-interkalirana područja grafena.

Poglavlje 6 - Interkalacija drugim elementima

U svrhu poopćivanja našeg istraživanja, prezentiramo rezultate interkalacije Gr/Ir(111) s litijem, europijem i kisikom. Na sl. 6.1 je pokazano nekoliko ARPES spektara za različite količine litija interkaliranog između grafena i iridija. Uočen je kontinuirani pomak Diracova stošca na veće vezivne energije te je za svaku razinu dopiranja vidljiv smeo jedan stožac. To znači da ne postoji fazna separacija na adsorbiranu i interkaliranu fazu kao što je bio slučaj kod interkalacija cezija (usp. sa sl. 5.7). Izostanak fazne separacije objašnjava se malenom dimenzijom Li atoma koji prilikom interkalacije ne moraju znatno odvojiti grafen od iridija i platiti veliku energiju delaminacije grafena. Zbog toga je interkalacija litija moguća već i kod niskih koncentracija, odnosno ne dolazi do stvaranja adsorbirane faze na površini grafena. Iz istih razloga je moguća potpuna desorpcija interkaliranog litija. Ovih rezultati još jednom ističu važnost van der Waals međudjelovanja između grafena i iridija, što je dodatno potvrđeno teorijskim DFT izračunima.

Dodatno je istražena elektronska struktura u blizini K točke u slučaju maksimalne koncentraciju interkaliranog litija koja je ekvivalentna (1×1) strukturi u odnosu na Ir(111). Odgovarajući ARPES spektar je prikazan na sl. 6.2 gdje se jasno se vidi n -dopirani Diracov stožac s Diracovom točkom na ~ 1.6 eV ispod Fermijevog nivoa. Dodatno, uočava se iridijevo površinsko stanje koje je pomaknuto na ~ 0.4 eV ispod Fermijevog nivoa. Iz toga zaključujemo da elektroni atomi litija osim Diracovih stanja također mogu efektivno dopirati i površinsko stanje substrata. Pomak površinskog stanja se događa tek nakon što se dostigne razina dopiranja grafena od ~ 1.2 eV nakon čega slijedi paralelni pomak Diracovog stošca i iridijevog površinskog stanja na veće vezivne energije. Takav pomak omogućava detaljniji uvid u međudjelovanje stanja Diracovog stošca i površinskog stanja iridija; Sl. 6.2 otkriva njihovu hibridizaciju (vidi bijele strelice na sl. 6.2) što podupire saznanja da do hibridizacije dolazi i u slučaju ne-interkaliranog grafena na Ir(111) [50, 51].

Nadalje, istražena je interkalacija Gr/Ir(111) europijem. Motivacija za istraživanjem

Eu interkalacije nalazi se u velikom magnetskom momentu od $7 \mu_B$ po Eu atomu i potencijalnom utjecaju koji on može imati na elektronsku strukturu grafena. Slično kao u slučaju cezija, depozicija europija na epitaksijalni grafen rezultira različitim strukturama u adsorbiranom ili interkaliranom obliku [86, 109]. Ako je temperatura depozicije 720 K ili više, dolazi do interkalacije europija u (2×2) ili $(\sqrt{3} \times \sqrt{3}) R30^\circ$ strukturi u odnosu na grafen [vidi sl. 6.3(a) i (b)]. Fotoemisijski spektri tih dviju struktura u blizini K točke su prikazani na sl. 6.3(c) i (d). U oba slučaja Diracov stožac je n -dopiran te su položaji Diracovih točaka određeni na $E_{D,(2 \times 2)} = -1.36$ eV and $E_{D,(\sqrt{3} \times \sqrt{3})R30^\circ} = -1.43$ eV. Eventualno spinsko cijepanje Diracovog stošca predviđeno zbog velikog magnetskog momenta Eu atoma nije opaženo. U ARPES spektrima obiju struktura razaznaje se vrpca na nekoliko stotina meV ispd Fermijevog nivoa koja je identificirana kao iridijevo površinsko stanje, slično kao i u slučaju interkalacije litijem. Za Eu- $(\sqrt{3} \times \sqrt{3}) R30^\circ$ strukturu, vidljive su dodatne vrpce u elektronskoj strukturi označene crvenom i žutom strelicom na sl. 6.3(d). Njihovo podrijetlo još uvijek nije dobro poznato no obje vrpce pokazuju hibridizaciju sa stanjima Diracovog stošca.

Od p -dopiranih sistema, istražena je interkalacija grafena na Ir(111) kisikom. Elektronska struktura u okolini Γ K točke prije i nakon interkalacije je prikazana na sl. 6.4. U Γ točki se mogu zamijetiti spinsko rascijepljena površinska stanja iridija koja iščezavaju nakon interkalacije kisikom. U K točki, prije interkalacije nalazimo dobro definirani Diracov stožac i iridijevo površinsko stanje na Fermijevom nivou, dok nakon interkalacije dolazi do pomaka stošca iznad Fermijevog nivoa, a iridijevo površinsko stanje iščezava, slično kao i u Γ točki. Interkalacija kisika dakle rezultira uništavanjem površinskih stanja iridija. Ovime je nedvojbeno dokazano da su upravo Diracovi elektroni zatočeni u elektronskim stanjima koja se opažaju na grafenskim kvantnim točkama interkaliranim kisikom [171] što je ujedno i prvi dokaz zatočenja Diracovih elektrona uopće. Kvantitativne informacije o elektronskoj strukturi p dopiranog Diracovog stošca su dobivene iz ARPES spektra prikazanog na sl. 6.5(a). Analizom lijeve grane stošca u energetsom prozoru između -0.2 i -1 eV dobivena je vrijednost za brzinu vrpce koja iznosi $v_F = 1.03 \times 10^6$ m/s te je određen položaj Diracove točke na 0.68 eV iznad Fermijevog nivoa što je u odličnom slaganju s STS rezultatima na istome sistemu [171]. Kristalna struktura interkaliranog O sloja je (2×1) u odnosu na iridij, kao što je utvrđeno iz LEED-a [vidi sl. 6.5(b)]. Intenzitet difrakcijskih točaka koje odgovaraju moiré strukturi je uvelike smanjen što je

indikacija reduciranog vezanja grafena na iridij.

Poglavlje 7 - Zaključak

Naša analiza elektronske strukture i grafenske pokrivenosti pokazala je da rast grafena na Ir(111) ima eksponencijalni karakter te da početni stadij rasta sačinjavaju mali grafenski otoci veličine nekoliko nanometara. Za cjeloviti grafenski sloj usredotočili smo se na strukturu nabora i pokazali da njihova kompleksna mreža pokazuje kvazi-heksagonalno uređenje te da je njihova unutarnja struktura složenija od jednostavnog polukružnog oblika. Također smo izvršili prvu karakterizaciju stanja zrcalnog potencijala grafena na Ir(111) koja su Rydbergovog tipa te smo dodatno pokazali da su elektroni koji nastanjuju ta stanja zarobljeni na grafenskim otocima. Iz naših rezultata interkalacije cezijem vidljivo je da interkalaciji prethodi formiranje razrijeđene faze Cs atoma adsorbiranih na grafen tj. dolazi do fazne separacije cezija. Proces interkalacije je reguliran finom međugrom između Coulomb i van der Waals međudjelovanja. Sveukupna dinamika interkalacije određena je grafenskim naborima i iridijevim stepenicama koji predstavljaju mjesta penetracije i difuzijske barijere za Cs atome. Također je otkriveno da je zbog promjene elektronske strukture i izlaznog rada nakon interkalacije cezija energija adsorpcije na ne-interkalirana područja veća u odnosu na interkalirana područja. Nadalje, sistemi interkalirani s Li, Eu i O pokazuju promjene elektronske strukture kako grafena tako i iridija. Kod interkalacije litija ne dolazi do fazne separacije te se ostvaruje značajan kontinuirani pomak Diracovog stošca i iridijevog površinskog stanja na veće vezivne energije. Pomak iridijevih površinskih stanja također je primijećen kod Eu-interkalarnih sustava kod kojih su dodatno opažene vrpce koje potječu od interkaliranog Eu sloja. Prilikom interkalacije kisikom, učinkovito se mogu uništiti površinska stanja iridija što nedvosmisleno dokazuje da je na grafenskim kvantnim točkama moguće zatočiti Diracove elektrone.

Bibliography

- [1] Novoselov, K. S. *et al.* Electric field effect in atomically thin carbon films. *Science* **306**, 666–9 (2004).
- [2] Karu, A. E. & Beer, M. Pyrolytic formation of highly crystalline graphite films. *Journal of Applied Physics* **37**, 2179–2181 (1966).
- [3] Irving, S. M. & Jr., P. L. W. Interaction of evaporated carbon with heated metal substrates. *Carbon* **5**, 399–402 (1967).
- [4] Presland, A. E. B. & Walker Jr., P. L. Growth of single-crystal graphite by pyrolysis of acetylene over metals. *Carbon* **7**, 1–8 (1969).
- [5] Emtsev, K. V. *et al.* Towards wafer-size graphene layers by atmospheric pressure graphitization of silicon carbide. *Nature materials* **8**, 203–7 (2009).
- [6] First, P. N. *et al.* Epitaxial Graphenes on Silicon Carbide. *MRS Bulletin* **35**, 296–305 (2010).
- [7] Bostwick, A. *et al.* Experimental studies of the electronic structure of graphene. *Progress in Surface Science* **84**, 380–413 (2009).
- [8] Sutter, P. W., Flege, J.-I. & Sutter, E. A. Epitaxial graphene on ruthenium. *Nature materials* **7**, 406–11 (2008).
- [9] Sutter, P., Sadowski, J. T. & Sutter, E. Graphene on Pt(111): Growth and substrate interaction. *Physical Review B* **80**, 245411 (2009).
- [10] Coraux, J., N'Diaye, A. T., Busse, C. & Michely, T. Structural coherency of graphene on Ir(111). *Nano letters* **8**, 565–70 (2008).
- [11] Varykhalov, A. *et al.* Electronic and Magnetic Properties of Quasifreestanding Graphene on Ni. *Physical Review Letters* **101**, 157601 (2008).
- [12] Murata, Y. *et al.* Growth structure and work function of bilayer graphene on Pd(111). *Physical Review B* **85**, 205443 (2012).
- [13] Batzill, M. The surface science of graphene: Metal interfaces, CVD synthesis, nanoribbons, chemical modifications, and defects. *Surface Science Reports* **67**, 83–115 (2012).
- [14] Wintterlin, J. & Bocquet, M.-L. Graphene on metal surfaces. *Surface Science* **603**, 1841–1852 (2009).

- [15] Li, X. *et al.* Large-Area Synthesis of High-Quality and Uniform Graphene Films on Copper Foils. *Science* **324**, 1312–1314 (2009).
- [16] Dresselhaus, M. & Dresselhaus, G. Intercalation compounds of graphite. *Advances in Physics* **30**, 139–326 (1981).
- [17] Geim, A. K. & Novoselov, K. S. The rise of graphene. *Nature materials* **6**, 183–91 (2007).
- [18] Geim, A. K. & Kim, P. Carbon wonderland. *Scientific American* **298**, 90–97 (2008).
- [19] Xu, M., Liang, T., Shi, M. & Chen, H. Graphene-like two-dimensional materials. *Chemical reviews* **113**, 3766–98 (2013).
- [20] Geim, A. K. & Grigorieva, I. V. Van der Waals heterostructures. *Nature* **499**, 419–25 (2013).
- [21] Hasan, M. Z. & Kane, C. L. Colloquium: Topological insulators. *Reviews of Modern Physics* **82**, 3045–3067 (2010).
- [22] Liu, Z. K. *et al.* Discovery of a three-dimensional topological Dirac semimetal, Na_3Bi . *Science* **343**, 864–7 (2014).
- [23] Liu, Z. K. *et al.* A stable three-dimensional topological Dirac semimetal Cd_3As_2 . *Nature Materials* **13**, 667–681 (2014).
- [24] Wehling, T. O., Black-Schaffer, A. M. & Balatsky, A. V. Dirac materials. *Advances in Physics* **63**, 1–76 (2014).
- [25] Castro Neto, A. H., Peres, N. M. R., Novoselov, K. S. & Geim, A. K. The electronic properties of graphene. *Reviews of Modern Physics* **81**, 109–162 (2009).
- [26] Katsnelson, M. I. Graphene : carbon in two dimensions. *Materials Today* **10**, 20–27 (2007).
- [27] Geim, A. K. & MacDonald, A. H. Graphene: Exploring Carbon Flatland. *Physics Today* **60**, 35 (2007).
- [28] Echenique, P. M. & Pendry, J. B. The existence and detection of Rydberg states at surfaces. *Journal of Physics C: Solid State Physics* **11**, 2065–2075 (1978).
- [29] Chulkov, E., Silkin, V. & Echenique, P. Image potential states on metal surfaces: binding energies and wave functions. *Surface Science* **437**, 330–352 (1999).
- [30] Fauster, T. & Steinmann, W. Two-photon photoemission spectroscopy of image states. In Halevi, P. (ed.) *Electromagnetic Waves: Recent Developments in Research*, vol. 2: Photonic Probes of Surfaces, 347–411 (Elsevier, Amsterdam, 1995).
- [31] Silkin, V. *et al.* Image potential states in graphene. *Physical Review B* **80**, 121408(R) (2009).
- [32] Sun, D. *et al.* Ultrafast hot-carrier-dominated photocurrent in graphene. *Nature nanotechnology* **7**, 114–8 (2012).

-
- [33] Bonaccorso, F., Sun, Z., Hasan, T. & Ferrari, A. C. Graphene photonics and optoelectronics. *Nature Photonics* **4**, 611–622 (2010).
 - [34] Csányi, G., Littlewood, P. B., Nevidomskyy, A. H., Pickard, C. J. & Simons, B. D. The role of the interlayer state in the electronic structure of superconducting graphite intercalated compounds. *Nature Physics* **1**, 42–45 (2005).
 - [35] Bolotin, K. I., Sikes, K. J., Hone, J., Stormer, H. L. & Kim, P. Temperature-Dependent Transport in Suspended Graphene. *Physical Review Letters* **101**, 096802 (2008).
 - [36] Novoselov, K. S. *et al.* Two-dimensional gas of massless Dirac fermions in graphene. *Nature* **438**, 197–200 (2005).
 - [37] Lee, C., Wei, X., Kysar, J. W. & Hone, J. Measurement of the elastic properties and intrinsic strength of monolayer graphene. *Science* **321**, 385–8 (2008).
 - [38] Bae, S. *et al.* Roll-to-roll production of 30-inch graphene films for transparent electrodes. *Nature nanotechnology* **5**, 574–8 (2010).
 - [39] Kim, K. S. *et al.* Large-scale pattern growth of graphene films for stretchable transparent electrodes. *Nature* **457**, 706–10 (2009).
 - [40] Lee, J.-H. *et al.* Wafer-Scale Growth of Single-Crystal Monolayer Graphene on Reusable Hydrogen-Terminated Germanium. *Science* **344**, 286–289 (2014).
 - [41] N’Diaye, A. T., Coraux, J., Plasa, T. N., Busse, C. & Michely, T. Structure of epitaxial graphene on Ir(111). *New Journal of Physics* **10**, 043033 (2008).
 - [42] Loginova, E., Bartelt, N. C., Feibelman, P. J. & McCarty, K. F. Factors influencing graphene growth on metal surfaces. *New Journal of Physics* **11**, 063046 (2009).
 - [43] Hattab, H. *et al.* Growth temperature dependent graphene alignment on Ir(111). *Applied Physics Letters* **98**, 141903 (2011).
 - [44] Loginova, E., Nie, S., Thürmer, K., Bartelt, N. & McCarty, K. Defects of graphene on Ir(111): Rotational domains and ridges. *Physical Review B* **80**, 085430 (2009).
 - [45] Hattab, H. *et al.* Interplay of wrinkles, strain, and lattice parameter in graphene on iridium. *Nano letters* **12**, 678–82 (2012).
 - [46] Pletikosić, I. *et al.* Dirac Cones and Minigaps for Graphene on Ir(111). *Physical Review Letters* **102**, 056808 (2009).
 - [47] Kralj, M. *et al.* Graphene on Ir(111) characterized by angle-resolved photoemission. *Physical Review B* **84**, 075427 (2011).
 - [48] Rusponi, S. *et al.* Highly Anisotropic Dirac Cones in Epitaxial Graphene Modulated by an Island Superlattice. *Physical Review Letters* **105**, 246803 (2010).
 - [49] Pletikosić, I. *et al.* Photoemission and density functional theory study of Ir(111); energy band gap mapping. *Journal of physics: Condensed matter* **22**, 135006 (2010).

- [50] Starodub, E. *et al.* In-plane orientation effects on the electronic structure, stability, and Raman scattering of monolayer graphene on Ir(111). *Physical Review B* **83**, 125428 (2011).
- [51] Busse, C. *et al.* Graphene on Ir(111): Physisorption with Chemical Modulation. *Physical Review Letters* **107**, 036101 (2011).
- [52] Liu, Z. *et al.* Interlayer binding energy of graphite: A mesoscopic determination from deformation. *Physical Review B* **85**, 205418 (2012).
- [53] Biedermann, L., Bolen, M., Capano, M., Zemlyanov, D. & Reifenberger, R. Insights into few-layer epitaxial graphene growth on 4H-SiC(000-1) substrates from STM studies. *Physical Review B* **79**, 125411 (2009).
- [54] Chae, S. J. *et al.* Synthesis of Large-Area Graphene Layers on Poly-Nickel Substrate by Chemical Vapor Deposition: Wrinkle Formation. *Advanced Materials* **21**, 2328–2333 (2009).
- [55] Obraztsov, A. N., Obraztsova, E. A., Tyurnina, A. V. & Zolotukhin, A. A. Chemical vapor deposition of thin graphite films of nanometer thickness. *Carbon* **45**, 2017–2021 (2007).
- [56] Sun, G. F., Jia, J. F., Xue, Q. K. & Li, L. Atomic-scale imaging and manipulation of ridges on epitaxial graphene on 6H-SiC(0001). *Nanotechnology* **20**, 355701 (2009).
- [57] Prakash, G., Capano, M. A., Bolen, M. L., Zemlyanov, D. & Reifenberger, R. G. AFM study of ridges in few-layer epitaxial graphene grown on the carbon-face of 4H-SiC(000-1). *Carbon* **48**, 2383–2393 (2010).
- [58] N'Diaye, A. T. *et al.* In situ observation of stress relaxation in epitaxial graphene. *New Journal of Physics* **11**, 113056 (2009).
- [59] Calado, V. E., Schneider, G. F., Theulings, A. M. M. G., Dekker, C. & Vandersypen, L. M. K. Formation and control of wrinkles in graphene by the wedging transfer method. *Applied Physics Letters* **101**, 103116 (2012).
- [60] Zhu, W. *et al.* Structure and electronic transport in graphene wrinkles. *Nano letters* **12**, 3431–6 (2012).
- [61] Ahmad, M. *et al.* Nanoscale investigation of charge transport at the grain boundaries and wrinkles in graphene film. *Nanotechnology* **23**, 285705 (2012).
- [62] Xu, K., Cao, P. & Heath, J. R. Scanning tunneling microscopy characterization of the electrical properties of wrinkles in exfoliated graphene monolayers. *Nano letters* **9**, 4446–51 (2009).
- [63] Starodub, E., Bartelt, N. C. & McCarty, K. F. Oxidation of Graphene on Metals. *The Journal of Physical Chemistry C* **114**, 5134–5140 (2010).
- [64] Lanza, M. *et al.* Tuning graphene morphology by substrate towards wrinkle-free devices: Experiment and simulation. *Journal of Applied Physics* **113**, 104301 (2013).
- [65] Kim, K. *et al.* Multiply folded graphene. *Physical Review B* **83**, 245433 (2011).

- [66] Coraux, J. *et al.* Growth of graphene on Ir(111). *New Journal of Physics* **11**, 023006 (2009).
- [67] Lizzit, S. & Baraldi, A. High-resolution fast X-ray photoelectron spectroscopy study of ethylene interaction with Ir(111): From chemisorption to dissociation and graphene formation. *Catalysis Today* **154**, 68–74 (2010).
- [68] Lacovig, P. *et al.* Growth of Dome-Shaped Carbon Nanoislands on Ir(111): The Intermediate between Carbide Clusters and Quasi-Free-Standing Graphene. *Physical Review Letters* **103**, 166101 (2009).
- [69] Grånäs, E. *et al.* Oxygen intercalation under graphene on Ir(111): energetics, kinetics, and the role of graphene edges. *ACS nano* **6**, 9951–63 (2012).
- [70] Subramaniam, D. *et al.* Wave-Function Mapping of Graphene Quantum Dots with Soft Confinement. *Physical Review Letters* **108**, 046801 (2012).
- [71] Hämäläinen, S. K. *et al.* Quantum-Confined Electronic States in Atomically Well-Defined Graphene Nanostructures. *Physical Review Letters* **107**, 236803 (2011).
- [72] Phark, S.-H. *et al.* Direct observation of electron confinement in epitaxial graphene nanoislands. *ACS nano* **5**, 8162–6 (2011).
- [73] Altenburg, S. J. *et al.* Local Gating of an Ir(111) Surface Resonance by Graphene Islands. *Physical Review Letters* **108**, 206805 (2012).
- [74] Riedl, C., Coletti, C., Iwasaki, T., Zakharov, A. A. & Starke, U. Quasi-Free-Standing Epitaxial Graphene on SiC Obtained by Hydrogen Intercalation. *Physical Review Letters* **103**, 246804 (2009).
- [75] Papagno, M. *et al.* Hybridization of graphene and a Ag monolayer supported on Re(0001). *Physical Review B* **88**, 235430 (2013).
- [76] Pacilé, D. *et al.* Artificially lattice-mismatched graphene/metal interface: Graphene/Ni/Ir(111). *Physical Review B* **87**, 035420 (2013).
- [77] Liu, H., Liu, Y. & Zhu, D. Chemical doping of graphene. *Journal of Materials Chemistry* **21**, 3335 (2011).
- [78] McChesney, J. L. *et al.* Extended van Hove Singularity and Superconducting Instability in Doped Graphene. *Physical Review Letters* **104**, 136803 (2010).
- [79] Jung, N. *et al.* Charge transfer chemical doping of few layer graphenes: charge distribution and band gap formation. *Nano letters* **9**, 4133–7 (2009).
- [80] Varykhalov, A., Scholz, M., Kim, T. & Rader, O. Effect of noble-metal contacts on doping and band gap of graphene. *Physical Review B* **82**, 121101(R) (2010).
- [81] Enderlein, C., Kim, Y. S., Bostwick, A., Rotenberg, E. & Horn, K. The formation of an energy gap in graphene on ruthenium by controlling the interface. *New Journal of Physics* **12**, 033014 (2010).
- [82] Yoo, J. J. *et al.* Ultrathin planar graphene supercapacitors. *Nano letters* **11**, 1423–7 (2011).

- [83] Emtsev, K., Zakharov, A., Coletti, C., Forti, S. & Starke, U. Ambipolar doping in quasifree epitaxial graphene on SiC(0001) controlled by Ge intercalation. *Physical Review B* **84**, 125423 (2011).
- [84] Decker, R. *et al.* Atomic-scale magnetism of cobalt-intercalated graphene. *Physical Review B* **87**, 041403 (2013).
- [85] Sicot, M. *et al.* Size-selected epitaxial nanoislands underneath graphene moiré on Rh(111). *ACS nano* **6**, 151–8 (2012).
- [86] Schumacher, S., Förster, D. F., Rösner, M., Wehling, T. O. & Michely, T. Strain in Epitaxial Graphene Visualized by Intercalation. *Physical Review Letters* **110**, 086111 (2013).
- [87] Bianchi, M. *et al.* Electron-phonon coupling in potassium-doped graphene: Angle-resolved photoemission spectroscopy. *Physical Review B* **81**, 041403(R) (2010).
- [88] Pletikosić, I., Kralj, M., Milun, M. & Pervan, P. Finding the bare band: Electron coupling to two phonon modes in potassium-doped graphene on Ir(111). *Physical Review B* **85**, 155447 (2012).
- [89] Tontegode, A. Y. Carbon on transition metal surfaces. *Progress in surface science* **38**, 201–429 (1991).
- [90] Larciprete, R. *et al.* Oxygen Switching of the Epitaxial Graphene-Metal Interaction. *ACS Nano* **6**, 9551–9558 (2012).
- [91] Rut'kov, E., Tontegode, A. & Usufov, M. Evidence for a C₆₀ Monolayer Intercalated between a Graphite Monolayer and Iridium. *Physical Review Letters* **74**, 758–760 (1995).
- [92] Vinogradov, N. A. *et al.* Hole doping of graphene supported on Ir(111) by AlBr₃. *Applied Physics Letters* **102**, 61601 (2013).
- [93] Li, L., Wang, Y., Meng, L., Wu, R.-t. & Gao, H.-J. Hafnium intercalation between epitaxial graphene and Ir(111) substrate. *Applied Physics Letters* **102**, 093106 (2013).
- [94] Vinogradov, N. A. *et al.* Controllable p-doping of graphene on Ir(111) by chlorination with FeCl₃. *Journal of physics: Condensed matter* **24**, 314202 (2012).
- [95] Bunch, J. S. *et al.* Impermeable atomic membranes from graphene sheets. *Nano letters* **8**, 2458–62 (2008).
- [96] Leenaerts, O., Partoens, B. & Peeters, F. M. Graphene: A perfect nanoballoon. *Applied Physics Letters* **93**, 193107 (2008).
- [97] Nagashima, A., Tejima, N. & Oshima, C. Electronic states of the pristine and alkali-metal-intercalated monolayer graphite/Ni(111) systems. *Physical Review B* **50**, 17487 (1994).
- [98] Huang, L. *et al.* Intercalation of metal islands and films at the interface of epitaxially grown graphene and Ru(0001) surfaces. *Applied Physics Letters* **99**, 163107 (2011).

-
- [99] Jin, L., Fu, Q., Yang, Y. & Bao, X. A comparative study of intercalation mechanism at graphene/Ru(0001) interface. *Surface Science* **617**, 81–86 (2013).
- [100] Büttner, M., Choudhury, P., Karl Johnson, J. & Yates, J. T. Vacancy clusters as entry ports for cesium intercalation in graphite. *Carbon* **49**, 3937–3952 (2011).
- [101] Arnoult, W. J. & McLellan, R. B. The solubility of carbon in rhodium, rutenium, iridium and rhenium. *Scripta Metallurgica* **6**, 1013 (1972).
- [102] Hüfner, S. *Photoelectron Spectroscopy: Principles and Applications* (Springer, New York, 1996), 2nd edn.
- [103] Bostwick, A. *et al.* Renormalization of graphene bands by many-body interactions. *Solid State Communications* **143**, 63–71 (2007).
- [104] Hüfner, S. (ed.) *Very High Resolution Photoelectron Spectroscopy* (Springer, Berlin Heidelberg, 2007).
- [105] Panaccione, G. *et al.* Advanced photoelectric effect experiment beamline at Elettra: A surface science laboratory coupled with Synchrotron Radiation. *The Review of scientific instruments* **80**, 043105 (2009).
- [106] Fauster, T. Two-Photon Photoelectron Spectroscopy. In Wandelt, K. (ed.) *Surface and Interface Science*, vol. 1: Concepts and Methods, 253–268 (Wiley-VCH, Weinheim, 2012).
- [107] Ueba, H. & Gumhalter, B. Theory of two-photon photoemission spectroscopy of surfaces. *Progress in Surface Science* **82**, 193–223 (2007).
- [108] Della Pia, A. & Costantini, G. Scanning Tunneling Microscopy. In Bracco, G. & Holst, B. (eds.) *Surface Science Techniques*, 565–597 (Springer, London, 2013).
- [109] Förster, D. F., Wehling, T. O., Schumacher, S., Rosch, A. & Michely, T. Phase coexistence of clusters and islands: europium on graphene. *New Journal of Physics* **14**, 023022 (2012).
- [110] Horcas, I. *et al.* WSXM: a software for scanning probe microscopy and a tool for nanotechnology. *The Review of scientific instruments* **78**, 013705 (2007).
- [111] Chen, C. J. *Introduction to scanning tunneling microscopy* (Oxford University Press, New York, 1993).
- [112] Besenbacher, F. Scanning tunnelling microscopy studies of metal surfaces. *Reports on Progress in Physics* **59**, 1737–1802 (1996).
- [113] Altman, M. S. Trends in low energy electron microscopy. *Journal of physics: Condensed matter* **22**, 084017 (2010).
- [114] Bauer, E. Low energy electron microscopy. *Reports on Progress in Physics* **57**, 895 (1994).
- [115] Man, K. L. & Altman, M. S. Low energy electron microscopy and photoemission electron microscopy investigation of graphene. *Journal of physics: Condensed matter* **24**, 314209 (2012).

- [116] Woodruff, D. P. & Delchar, T. A. *Modern techniques of surface science* (Cambridge University Press, Cambridge, 1989).
- [117] Held, G. Low-energy Electron Diffraction (LEED). In Bubert, H. & Jenett, H. (eds.) *Surface and Thin Film Analysis: Principles, Instrumentation, Applications*, 71–85 (Wiley-VCH, Weinheim, 2002).
- [118] Šrut, I., Mikšić Trontl, V., Pervan, P. & Kralj, M. Temperature dependence of graphene growth on a stepped iridium surface. *Carbon* **56**, 193–200 (2013).
- [119] Casarin, B. *et al.* The Thinnest Carpet on the Smallest Staircase: The Growth of Graphene on Rh(533). *The Journal of Physical Chemistry C* **118**, 6242–6250 (2014).
- [120] Pisarra, M. *et al.* Electronic structure of epitaxial graphene grown on stepped Pt(997). *Physical Review B* **89**, 195438 (2014).
- [121] Hammer, L. *et al.* Hydrogen-Induced Self-Organized Nanostructuring of the Ir(100) Surface. *Physical Review Letters* **91**, 156101 (2003).
- [122] Heinz, K. & Hammer, L. Nanostructure formation on Ir(100). *Progress in Surface Science* **84**, 2–17 (2009).
- [123] Locatelli, A. *et al.* Temperature-driven reversible rippling and bonding of a graphene superlattice. *ACS nano* **7**, 6955–63 (2013).
- [124] Locatelli, A., Zamborlini, G. & MenteÅŸ, T. O. Growth of single and multi-layer graphene on Ir(100). *Carbon* **74**, 237–248 (2014).
- [125] Preobrajenski, A. B., Ng, M. L., Vinogradov, A. S. & Mårtensson, N. Controlling graphene corrugation on lattice-mismatched substrates. *Physical Review B* **78**, 073401 (2008).
- [126] Gao, M. *et al.* Epitaxial growth and structural property of graphene on Pt(111). *Applied Physics Letters* **98**, 033101 (2011).
- [127] Varykhalov, A. *et al.* Ir(111) Surface State with Giant Rashba Splitting Persists under Graphene in Air. *Physical Review Letters* **108**, 066804 (2012).
- [128] Borca, B. *et al.* Potential Energy Landscape for Hot Electrons in Periodically Nanostructured Graphene. *Physical Review Letters* **105**, 036804 (2010).
- [129] Brako, R., Šokčević, D., Lazić, P. & Atodiresei, N. Graphene on the Ir(111) surface: from van der Waals to strong bonding. *New Journal of Physics* **12**, 113016 (2010).
- [130] Seah, M. P. & Dench, W. A. Quantitative electron spectroscopy of surfaces: A standard data base for electron inelastic mean free paths in solids. *Surface and Interface Analysis* **1**, 2–11 (1979).
- [131] Nieuwenhuys, B. E., Hagen, D. I., Rovida, G. & Somorjai, G. A. LEED, AES and thermal desorption studies of chemisorbed hydrogen and hydrocarbons (C₂H₂, C₂H₄, C₆H₆, C₆H₁₂) on the (111) and stepped [6(111)×(100)] iridium crystal surfaces; comparison with platinum. *Surface Science* **59**, 155–176 (1976).

-
- [132] Marinova, T. S. & Kostov, K. L. Adsorption of acetylene and ethylene on a clean Ir(111) surface. *Surface Science* **181**, 573–585 (1987).
- [133] Schuppler, S., Fischer, N., Fauster, T. & Steinmann, W. Bichromatic two-photon photoemission spectroscopy of image potential states on Ag(100). *Applied Physics A Solids and Surfaces* **51**, 322–326 (1990).
- [134] Niesner, D. *et al.* Trapping surface electrons on graphene layers and islands. *Physical Review B* **85**, 081402(R) (2012).
- [135] Fischer, N., Schuppler, S., Fauster, T. & Steinmann, W. Coverage-dependent electronic structure of Na on Cu(111). *Surface Science* **314**, 89–96 (1994).
- [136] Giovannetti, G. *et al.* Doping Graphene with Metal Contacts. *Physical Review Letters* **101**, 026803 (2008).
- [137] Okabe, A., Boots, B., Suhihara, K. & Chiu, S. N. *Spatial Tessellations: Concepts and Applications of Voronoi Diagrams* (Wiley, Chichester, 1992), 2nd edn.
- [138] Hilhorsta, H. J. Statistical properties of planar Voronoi tessellations. *The European Physical Journal B* **64**, 437–441 (2008).
- [139] Reinert, F., Nicolay, G., Schmidt, S., Ehm, D. & Hüfner, S. Direct measurements of the L-gap surface states on the (111) face of noble metals by photoelectron spectroscopy. *Physical Review B* **63**, 115415 (2001).
- [140] Bihlmayer, G., Koroteev, Y., Echenique, P., Chulkov, E. & Blügel, S. The Rashba-effect at metallic surfaces. *Surface Science* **600**, 3888–3891 (2006).
- [141] Petersen, L. & Hedegård, P. A simple tight-binding model of spin–orbit splitting of sp-derived surface states. *Surface Science* **459**, 49–56 (2000).
- [142] LaShell, S., McDougall, B. & Jensen, E. Spin Splitting of an Au(111) Surface State Band Observed with Angle Resolved Photoelectron Spectroscopy. *Physical Review Letters* **77**, 3419–3422 (1996).
- [143] Varykhalov, a. *et al.* Ir(111) Surface State with Giant Rashba Splitting Persists under Graphene in Air. *Physical Review Letters* **108**, 066804 (2012).
- [144] Hengsberger, M., Baumberger, F., Neff, H., Greber, T. & Osterwalder, J. Photoemission momentum mapping and wave function analysis of surface and bulk states on flat Cu(111) and stepped Cu(443) surfaces: A two-photon photoemission study. *Physical Review B* **77**, 085425 (2008).
- [145] Takahashi, K., Imamura, M., Yamamoto, I., Azuma, J. & Kamada, M. Image potential states in monolayer, bilayer, and trilayer epitaxial graphene studied with time- and angle-resolved two-photon photoemission spectroscopy. *Physical Review B* **89**, 155303 (2014).
- [146] Nobis, D., Potenz, M., Niesner, D. & Fauster, T. Image-potential states of graphene on noble-metal surfaces. *Physical Review B* **88**, 195435 (2013).
- [147] Bose, S. *et al.* Image potential states as a quantum probe of graphene interfaces. *New Journal of Physics* **12**, 023028 (2010).

- [148] Craes, F. *et al.* Mapping Image Potential States on Graphene Quantum Dots. *Physical Review Letters* **111**, 056804 (2013).
- [149] Rut'kov, E. V. & Gall', N. R. Intercalation of Graphene Films on Metals with Atoms and Molecules. In Mikhailov, S. (ed.) *Physics and Applications of Graphene - Experiments*, chap. 12, 293–326 (InTech, Rijeka, 2011).
- [150] Hu, Z. P., Wu, N. J. & Ignatiev, A. Cesium adsorption on graphite (0001) surface: The phase diagram. *Physical Review B* **33**, 7683–7687 (1986).
- [151] Chung, W. *et al.* Layer Spacings in Coherently Strained Epitaxial Metal Films. *Physical Review Letters* **90**, 216105 (2003).
- [152] Petrović, M. *et al.* The mechanism of caesium intercalation of graphene. *Nature communications* **4**, 2772 (2013).
- [153] Runte, S. Atomic and Electronic Structure of Graphene and Graphene Intercalation Compounds. X-Ray Standing Wave and Scanning Tunnelling Microscopy Studies. *PhD thesis, University of Cologne* (2014).
- [154] Koepke, J. C. *et al.* Atomic-scale evidence for potential barriers and strong carrier scattering at graphene grain boundaries: a scanning tunneling microscopy study. *ACS nano* **7**, 75–86 (2013).
- [155] Vlaic, S. *et al.* Cobalt intercalation at the graphene/iridium(111) interface: Influence of rotational domains, wrinkles, and atomic steps. *Applied Physics Letters* **104**, 101602 (2014).
- [156] Song, C.-L. *et al.* Charge-Transfer-Induced Cesium Superlattices on Graphene. *Physical Review Letters* **108**, 156803 (2012).
- [157] Repp, J. *et al.* Substrate mediated long-range oscillatory interaction between adatoms: Cu/Cu(111). *Physical Review Letters* **85**, 2981–4 (2000).
- [158] Knorr, N. *et al.* Long-range adsorbate interactions mediated by a two-dimensional electron gas. *Physical Review B* **65**, 115420 (2002).
- [159] Ternes, M. *et al.* Scanning-Tunneling Spectroscopy of Surface-State Electrons Scattered by a Slightly Disordered Two-Dimensional Dilute “Solid”: Ce on Ag(111). *Physical Review Letters* **93**, 146805 (2004).
- [160] Silly, F. *et al.* Creation of an Atomic Superlattice by Immersing Metallic Adatoms in a Two-Dimensional Electron Sea. *Physical Review Letters* **92**, 016101 (2004).
- [161] von Hofe, T., Kröger, J. & Berndt, R. Adsorption geometry of Cu(111)-Cs studied by scanning tunneling microscopy. *Physical Review B* **73**, 245434 (2006).
- [162] Rutter, G. M. *et al.* Scattering and interference in epitaxial graphene. *Science* **317**, 219–22 (2007).
- [163] Mallet, P. *et al.* Role of pseudospin in quasiparticle interferences in epitaxial graphene probed by high-resolution scanning tunneling microscopy. *Physical Review B* **86**, 045444 (2012).

-
- [164] Petersen, L., Hofmann, P., Plummer, E. & Besenbacher, F. Fourier Transform–STM: determining the surface Fermi contour. *Journal of Electron Spectroscopy and Related Phenomena* **109**, 97–115 (2000).
- [165] Bena, C. & Kivelson, S. Quasiparticle scattering and local density of states in graphite. *Physical Review B* **72**, 125432 (2005).
- [166] Bena, C. Effect of a Single Localized Impurity on the Local Density of States in Monolayer and Bilayer Graphene. *Physical Review Letters* **100**, 076601 (2008).
- [167] Ruffieux, P., Groning, O., Schwaller, P., Schlapbach, L. & Groning, P. Hydrogen atoms cause long-range electronic effects on graphite. *Physical Review Letters* **84**, 4910–3 (2000).
- [168] Ruffieux, P. *et al.* Charge-density oscillation on graphite induced by the interference of electron waves. *Physical Review B* **71**, 153403 (2005).
- [169] Ugeda, M. *et al.* Point Defects on Graphene on Metals. *Physical Review Letters* **107**, 116803 (2011).
- [170] Martínez-galera, A. J., Brihuega, I. & Gómez-rodríguez, J. M. Ethylene Irradiation: A new route to grow graphene on low reactivity metals. *Nano letters* **11**, 3576–3580 (2011).
- [171] Jolie, W. *et al.* Confinement of Dirac electrons in graphene quantum dots. *Physical Review B* **89**, 155435 (2014).
- [172] Schedin, F. *et al.* Detection of individual gas molecules adsorbed on graphene. *Nature materials* **6**, 652–5 (2007).
- [173] Wehling, T., Katsnelson, M. & A.I., L. Adsorbates on graphene: Impurity states and electron scattering. *Chemical Physics Letters* **476**, 125–134 (2009).
- [174] Brar, V. W. *et al.* Gate-controlled ionization and screening of cobalt adatoms on a graphene surface. *Nature Physics* **7**, 43–47 (2010).
- [175] Sato, Y., Takai, K. & Enoki, T. Electrically controlled adsorption of oxygen in bilayer graphene devices. *Nano letters* **11**, 3468–75 (2011).
- [176] Huang, L. F. *et al.* Modulation of the thermodynamic, kinetic and magnetic properties of the hydrogen monomer on graphene by charge doping. *The Journal of chemical physics* **135**, 064705 (2011).
- [177] Khomyakov, P. A. *et al.* First-principles study of the interaction and charge transfer between graphene and metals. *Physical Review B* **79**, 195425 (2009).
- [178] Schumacher, S. *et al.* The backside of graphene: manipulating adsorption by intercalation. *Nano letters* **13**, 5013–9 (2013).
- [179] Desjonqueres, M.-C. & Spanjaard, D. *Concepts in Surface Physics* (Springer, New York, 1996), 2nd edn.
- [180] Lazić, P. private communication .

- [181] Johannsen, J. C. *et al.* Electron-phonon coupling in quasi-free-standing graphene. *Journal of physics: Condensed matter* **25**, 094001 (2013).
- [182] Haberer, D. *et al.* Anisotropic Eliashberg function and electron-phonon coupling in doped graphene. *Physical Review B* **88**, 081401 (2013).
- [183] Fedorov, A. V. *et al.* Observation of a universal donor-dependent vibrational mode in graphene. *Nature Communications* **5**, 3257 (2014).
- [184] Zhang, Y. *et al.* Giant phonon-induced conductance in scanning tunnelling spectroscopy of gate-tunable graphene. *Nature Physics* **4**, 627–630 (2008).
- [185] Leicht, P. *et al.* In Situ Fabrication Of Quasi-Free-Standing Epitaxial Graphene. *ACS Nano* **8**, 3735–3742 (2014).
- [186] Saito, R., Dresselhaus, G. & Dresselhaus, M. S. *Physical Properties of Carbon Nanotubes* (Imperial College Press, London, 1998).
- [187] Voloshina, E. N. *et al.* Electronic structure and imaging contrast of graphene moiré on metals. *Scientific reports* **3**, 1072 (2013).

Curriculum vitae

Personal information

Name and surname	Marin Petrović
Date and place of birth	May 27, 1985, Varaždin, Croatia
e-mail	mpetrovic@ifs.hr

Education

Dates	February 2011 - October 2014
Institution	Faculty of Science, University of Zagreb
Title awarded	(PhD student)

Dates	September 2004 - December 2009
Institution	Faculty of Science, University of Zagreb
Title awarded	dipl. ing. (Bologna equivalent: Master of Science in Physics) Thesis title: Electronic properties of intercalated graphene

Dates	September 2000 - June 2004
Institution	First high school Varaždin

Work experience

Dates	February 2010 - present
Institution	Institute of Physics, Zagreb
Position held	Research assistant

Research interests	graphene, surface physics, 2D materials, nanostructures
--------------------	---------------------------------------------------------

List of publications

1. Jolie, W., Craes, F., Petrović, M., Atodiresei, N., Caciuc, V., Blügel, S., Kralj, M., Michely, T. and Busse, C. Confinement of Dirac electrons in graphene quantum dots. *Physical Review B* **89**, 155435 (2014).
2. Petrović, M., Šrut Rakić, I., Runte, S., Busse, C., Sadowski, J. T., Lazić, P., Pletikosić, I., Pan, Z.-H., Milun, M., Pervan, P., Atodiresei, N., Brako, R., Šokčević, R., Valla, T., Michely, T. and Kralj, M. The mechanism of caesium intercalation of graphene. *Nature Communications* **4**, 2772 (2013).
3. Schumacher, S., Wehling, T. O., Lazić, P., Runte, S., Förster, D. F., Busse, C., Petrović, M., Kralj, M., Blügel, S., Atodiresei, N., Caciuc, V. and Michely, T. The Backside of Graphene: Manipulating Adsorption by Intercalation. *Nano Letters* **13**, 5013 (2013).
4. Niesner, D., Fauster, Th., Dadap, J. I., Zaki, N., Knox, K. R., Yeh, P.-C., Bhandari,

- R., Osgood, R. M., Petrović, M. and Kralj, M. Trapping Surface Electrons on Graphene Layers and Islands. *Physical Review B* **85**, 081402(R) (2012).
5. Dadap, J. I., Kralj, M., Petrović, M., Knox, K., Bhandari, R., Yeh, P., Zaki, N. and Osgood, R. M. Observation of Image States in Graphene on Ir(111) by Two-Photon Photoemission. *CLEO:2011 - Laser Applications to Photonic Applications*, paper QTuK6 (2011).
 6. Kralj, M., Pletikosić, I., Petrović, M., Pervan, P., Milun, M., N'Diaye, A. T., Busse, C., Michely, T., Fuji, J. and Vobornik, I. Graphene on Ir(111) characterized by angle-resolved photoemission. *Physical Review B* **84**, 075427 (2011).

Participation in workshops and conferences

1. European Workshop on Epitaxial Graphene and 2D materials (EWEG/2D), Primošten, Croatia, June 2014. *Wrinkles of graphene on Ir(111) - internal structure and long-range ordering*, poster.
2. 21st International scientific meeting on vacuum science and techniques, Samobor, Croatia, May 2014. *Characterizing wrinkles of graphene on Ir(111)*, poster.
3. International Academic Workshop in Dynamics of Molecules on Surfaces, Osaka, Japan, August 2013. *Experimental and theoretical study on the intercalation of graphene on Ir(111)*, talk.
4. 20th International scientific meeting on vacuum science and techniques, Jeruzalem, Slovenia, May 2013. *Understanding intercalation of epitaxial graphene*, invited talk.
5. European Workshop on Epitaxial Graphene (EWEG), Aussois, France, January 2013. *Cesium on graphene on Ir(111): adsorption, intercalation and desorption*, talk.
6. Lithography and nanocharacterization in action, workshop at Institute of Physics, Zagreb, Croatia, June 2012. *Microscopic View at Large-Scale Graphene Monocrystal*, talk.
7. 76th Annual meeting of the DPG and combined DPG spring meeting, Berlin, Germany, March 2012. *Intercalation of Cs through wrinkles of epitaxial graphene*, poster.
8. 7th Scientific meeting of Croatian Physical Society, Primošten, Hrvatska, October 2011. *Epitaxial graphene on Ir(111) - Growth and structure characterization*, talk.
9. Novel materials for electronics: From production to devices, workshop at Institute of Physics, Zagreb, Hrvatska, June 2011. *Low Energy Electron Microscopy: Principles and applications*, talk.
10. 75th Annual meeting of the DPG and combined DPG spring meeting, Dresden, Germany, March 2011. *Graphene flakes growth study by ARPES*, talk.

Seminars

MURI seminar at Columbia University, New York, SAD, November 2012. *Cesium on graphene on Ir(111): A detailed study of a graphene hybrid system.*

Awards

Annual Young scientist award in the field of physics, awarded by The society of university teachers, scholars and other scientists - Zagreb, March 2014.